BODIPY as building blocks for Near InfraRed-Active Organic Compounds

Dissertation

Zur Erlangung des akademischen Grades

Doktor der Naturwissenschaften

(Dr. rer. nat.)

eingereicht an der Fakultät für

Mathematik und Naturwissenschaften

der Bergischen Universität Wuppertal

von

Benedetta Maria Squeo

aus Foggia

Wuppertal, 8 November 2018

.

The PhD thesis can be quoted as follows:

urn:nbn:de:hbz:468-20181204-140514-6
[http://nbn-resolving.de/urn/resolver.pl?urn=urn%3Anbn%3Ade%3Ahbz%3A468-20181204-140514-6]

This work was carried out during the period from March 2014 to March 2017 in the Research Laboratory of Advent Technologies SA, Patra, Greece, under the supervision of Prof. Dr. Ullrich Scherf and Dr. Christos L. Chochos.

This project has received funding from the European Community's Seventh Framework Programme (FP7/2007-2013) under the Grant Agreements n° 607585 project OSNIRO.

1. Supervisor: Prof. Dr. Ullrich Scherf, Bergische Universität Wuppertal.

2. Reviewer: Dr. Christos L. Chochos,
- Advent Technologies SA
- Institute of Biology, Medicinal Chemistry & Biotechnology, National Hellenic Research Foundation

Abstract

BODIPY (4,4-difluoro-4-bora-3a,4a-diaza-s-indacene) dyes are promising building blocks for the synthesis of NIR organic materials. Compared to other dye classes, these systems offer unique attractions such as excellent thermal/photochemical stability, intense absorption/emission profiles, negligible triplet-state formation, and small Stokes shifts. Their optoelectronic and semiconductor properties can be finely tuned via facile synthetic modifications on the dipyrromethene core.

In this PhD thesis new organic NIR materials (both π-conjugated polymers and small molecules) based on α,β-unsubstituted meso-positioning thienyl BODIPY have been developed, and their optoelectronic properties and their performances when applied in organic light emitting diodes and organic solar cells have been characterized and evaluated.

In more details, on the one hand donor-acceptor quarterthiophene-BODIPY polymers have been synthesized and the dependence of their optoelectronic, electrochemical and charge transporting properties of the resulting α,β-unsubstituted meso-positioning thienyl BODIPY quaterthiophene-based polymers from the alkyl side chain position have been studied. Tail-to-tail (TT) positioning of the alkyl side chains at the two central thiophenes of the quaterthiophene segment results in lower E_g^{opt}, higher energy levels and increased hole mobility as compared to head-to-head (HH) positioning. However, even though the synthesized polymers exhibit high electron affinity, higher even than that of the fullerene $PC_{71}BM$, they present only p-type behavior in field effect transistors (FETs) independent of the alkyl side chain positioning. Furthermore, one of the synthesized copolymers containing a vinylene bond in the middle of the quarterthiophene segment exhibits a panchromatic absorption spectrum ranging from 300 nm to 1100 nm and an optical band gap around 1 eV, suitable for near infrared (NIR) organic photovoltaic applications as electron donor. Preliminary power conversion efficiency (PCE) in bulk heterojunction (BHJ) solar cells of 1.1% in polymer:[6,6]-phenyl-C_{71}-butyric acid methyl ester ($PC_{71}BM$) [1:3 weight ratio] has been achieved, demonstrating very interesting and promising photovoltaic characteristics, such as good fill factor (FF) and open circuit voltage (V_{oc}).

On the other hand, BODIPY unit have been symmetrically conjugate with oligothienyls in a “metal-free” A-D-A (acceptor-donor-acceptor) oligomer emitting in the near-infrared (NIR) thanks to the delocalisation of the BODIPY low-lying lowest unoccupied molecular orbital (LUMO) over the oligothienyl moieties, as confirmed by density functional theory (DFT). A PL efficiency of 20% in the solid

state (vs. 30% in dilute solutions) has been retained by incorporating such a dye in a wider gap polyfluorene matrix and demonstrate organic light-emitting diodes (OLEDs) emitting at 720 nm. We achieved external quantum efficiencies (EQEs) up to 1.1%, the highest value recorded so far by a “metal-free” NIR-OLED not intentionally benefitting from triplet-triplet annihilation. These results demonstrate for the first time the promise of A-D-A type dyes for NIR OLEDs applications thereby paving the way for further optimization.

Table of Contents

Chapter 1

1. Introduction

Organic π-conjugated materials have attracted a tremendous academic and industrial interest in the last decades[1–4]. Thanks to their optoelectronic properties, nowadays these compounds are used as active material in several applications such as organic field effect transistors (OFETs)[5–9], organic light emitting devices (OLEDs)a[10–13], organic photovoltaics (OPVs)[14–20], bio-imaging[21,22], organic solid lasers[23], and many others[24].

1.1 Near Infrared materials

The infrared (IR) radiation is electromagnetic radiation with wavelength longer than those of visible light, but shorter than microwave. The bound between visible light and infrared radiation is not clearly defined. Generally we can consider the infrared radiation the one ranging between 700 nm and 10 μm, and more specifically near infrared (NIR) region the one between 700 nm and 2500 nm.

1.1.1. Classes of NIR materials

The characteristic features of the NIR materials are that they absorb, emit and generally interact with NIR light under external stimulation like electromagnetic field, photoexcitation and chemical reaction and they can be divided in two classes the inorganic and the organic materials.

Among the inorganic compounds, semiconductor nanocrystals (NCs) of II-IV, III-V and IV-VI group, like HgSe, HgTe, InAs, and PbX (X = S, Se, Te) NCs, are emerging as new promising class thanks to the easy production

process by colloidal synthetic methods in aqueous or organic solution and size-depending energy gap[25–27].

Metal-oxide films, like WO_3, MoO_3, TiO_2, Ta_2O_5, and Nb_2O_5, are another class of inorganic NIR materials showing interesting properties like electrochromic behavior and, in reduced form, strong absorption in the NIR region[28].

As regards the organic materials, typical NIR absorbing/emitting compounds are π-conjugated chromophores, like polyenes and polymethines[29,30], charge-transfer chromophores, like cyanines[31,32] and azo dyes[33,34], metal complexes like porphyrines[35,36] and donor-acceptor chromophores[37–39]. The energy gap and consequently the optoelectronic properties of these compounds can be controlled through several factors, like bond length alternation and donor-acceptor charge transfer which will be discussed in the next section (1.2).

1.1.2. Application of NIR materials

The fluorescence, absorption, photoconductive, photosensitizing, photochromic and other properties of the NIR organic materials can find application in different military and civilian fields: military applications include target acquisition, surveillance, night vision, homing, and tracking, while civilian application include energy harvesting, bio-imagining, telecommunication[40,41]. NIR absorbing materials found application in different technological sectors: for example, they are used as pigmets in laser printers, but also as filter in plasma TV and photosensitizer in photodynamic therapy for treatment of cancer[37,42].

In the last decades researchers focused on the synthesis of new material and or new design of solar cells in order to boost the power conversion efficiency (PCE)[43,44]. One way it is to use NIR sensitizer since more than 50% of solar radiation falls in the NIR spectral region[45–47]: the use of ternary ink (NIR

sensitizer, donor polymer and fullerene) has demonstrated to improve of more than 30% the performance compared to the same device without sensitizer[48].

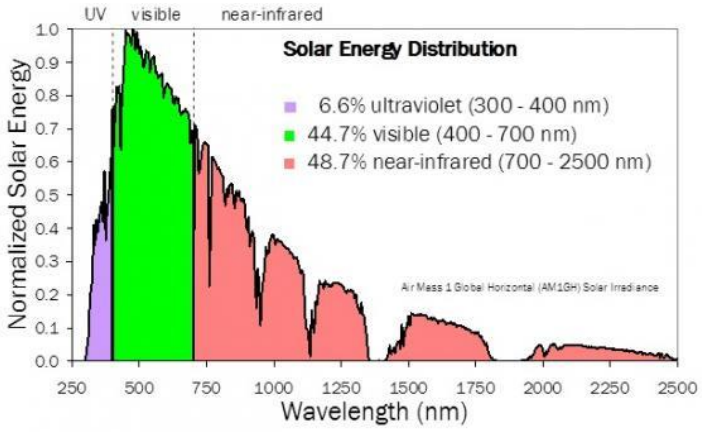

Figure 1. Solar energy distribution (Image courtesy of Heat Island Group, Lawrence Berkeley National Laboratory)

NIR organic emitters are less available, but are receiving more attention for their potential application in optical communication, NIR emissive organic materials may find applications in night-vision target identification, information security display, and sensors[49].

As regards the bio imagining, NIR dyes show interesting feature like minimal interfering absorption and fluorescence from biological samples, inexpensive laser diode excitation, reduced scattering and enhanced tissue penetration depth[50,51]. Boppart et al.[52] presented, for example, a new contrast-enhancing agent for tomography and more recently Li et al. presented a new imagining probe, emitting in the NIR region, for analysis *in vivo*.

1.2 Molecular design and energy gap engineering

The optical and electronic properties of organic materials depend on the energy gap, which is the difference between the highest occupied molecular orbital (HOMO) and the lowest unoccupied molecular orbital (LUMO). Lowering the energy gap results in a red shift of absorption and emission spectra, therefore the engineering of HOMO-LUMO level is a key for low energy gap materials and several design factors, as intrinsic energy gap, conjugation length and donor-acceptor charge transfer should be considered.

1.2.1 Intrinsic energy bandgap

In polyene, like polyacetylene, electrons can be delocalized, if there are no defects, all along the chain, while in polyarylene there is a competition between the delocalization of electrons along the chain and confinement in the rings; the resonance energy, is a measure of this delocalization and of monomer stability. Moreover in polyarylene system there are two ground states, corresponding at two limiting mesomeric forms obtained by the flip of the double bonds, which are not energetically equivalent. While the aromatic form is energetically more stable, the quinoid form has a higher energy but a lower energy gap[53].

The intrinsic bandgap of an isolated conjugated polymer chain can be described by a combination of different energy contribution related to the bond length alternation (BLA), the resonance energy stabilization (RE), the torsional angle θ and the mesomeric or inductive effect of substituent (E_R)[54].

$$E_g = E_{\Delta r} + RE + E_\theta + E_R$$

If we consider polyacetylene, we can describe it as infinite chain of CH, with a completely filled valence band and it should behave as a conductive metal, but between the valence band and the conduction band there is a forbidden zone (the energy gap) originated by the alternation of short (double) bond

and long (single) bond and described by the so called Peierls instability[55]. The value of the energy gap so, can be correlated to the degree of BLA, Δr, defined as length difference between a double and a single bond: the larger the Δr, the higher it will be the energy gap. In polyaromatic compound Δr is defined as maximum difference between the length of a C-C bond inclined relative to the chain axis and a C-C bond parallel to the chain axis. Bredes[56,57] studied the relationship between Δr and energy gap in polythiophene and from theoretical calculation they found how Δr tends to be more positive when the quinoid contributions to RE increase (Figure 2).

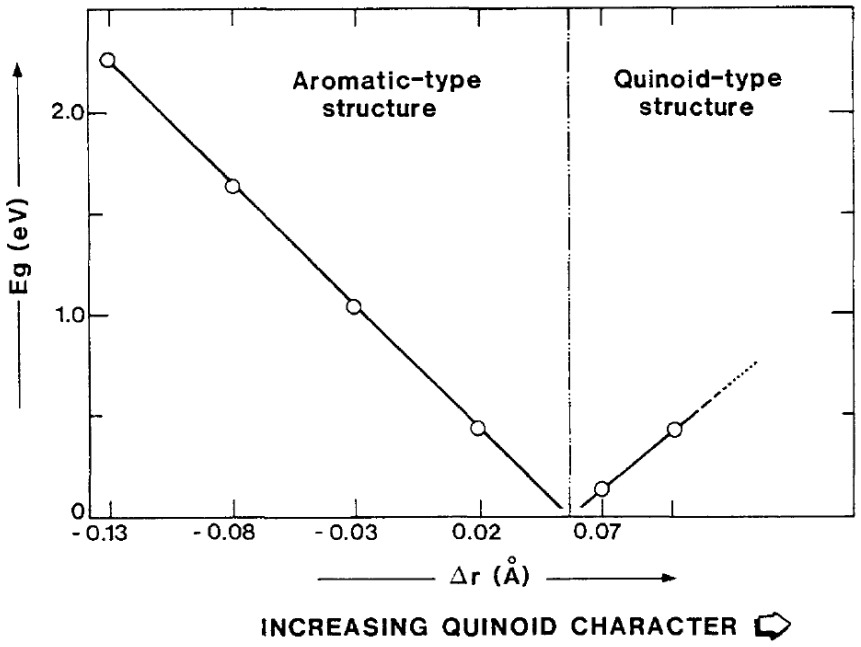

Figure 2. Evolution of the bandgap E_g (eV) as a function of aromatic and quinoid character. (Reproduced by permission of Elsevier Science from J. L. Bredas, Synth. Meth. 17,115 (1987). Copyright © 1987, Elsevier Science.)

This concept results in the synthesis of polyisothianaphtene by Kobayashi et al.[58]. Polyisothianaphtene is a polythiophene derivate where all thiophenes are fused with a benzene ring through β-β' thiophene bond: the benzene rings stabilize the quionoid contributions and the energy gap decreases from 2.2 eV in polythiophene to 1.0 eV in polyisothianaphtene[59].

Furthermore, the presence of heteroatoms in aromatic ring systems can considerably influence the electronic properties. The effect of such a substitution on the relative stability of aromatic ring systems can be evaluated by the resonance energy per electron (REPE). Table 1 shows the decrease of the energy gap upon decreasing the value of REPE. This means that decreasing the aromaticity of the polymer leads to lowering of the band gap it will be[60,61].

Table 1. Resonance Energy (RE) and resonance energy per electron (REPE) values for various heterocyclic and the energies gap (eV) of corresponding polymers.

Compound	RE (β)	REPE (β)	E_g (eV)
Benzene	0.390	0.065	3.4
Pyrrole	0.233	0.039	3.1
Thiophene	0.193	0.032	2.1
Isothianaphtene	0.247	0.025	1.1

Not less important is the linearity of polymer chains for the delocalization of electrons along the π-system. Bredas et al. calculated[62], on theoretical level, the correlation between the energy gap and the torsional angle and found out that increasing the dihedral angle θ from 0° to 90° leads to an increase of the energy gap from a minimum value to a maximum, because of the cosθ dependence of π-orbital overlap. These results were confirmed also by Cui and Kertsets[63] studying polythiophene: the bandgap is maximum, 4.5 eV, with θ = 90°, corresponding to no π-electron interaction between neighboring ring systems, and a further increase, from 90° to 180° results in a decrease of the bandgap; at 180°, in trans-coplanar conformation, the theoretical value of E_g is 1.7 eV.

Substituents play also a fundamental role in the bandgap engineering and their introduction is a direct way to modify the HOMO and LUMO energy levels and to fine tune the energy band gap.

Electron-withdrawing groups, such as nitro, carboxy or cyano and electron-donating groups such as alkyl, alkoxy or alkylsulfanyl have a mesomeric and/or inductive effect which stabilize the energy level and reduce the E_g. The electron-withdrawing substituents down-shift the LUMO and HOMO energy levels versus vacuum (the down-shift of the LUMO is usually more than that of the HOMO), while electron-donating substituents upshift the LUMO and HOMO energy levels (the up-shift of the HOMO is usually more than that of the LUMO)[64]. For example the introduction of an electron-withdrawing group such as a cyano in the vinylene linkage in poly(thienylenevinylene) results in a decrease of LUMO level due to the inductive effect (-I) of cyano group and a general reduction of energy gap (from 1.80 eV to 0.60 eV)[65].

We can say that all of the factors leading to a decrease in π-delocalization across the polymer backbone will result in an increasing in the bandgap and vice versa.

1.2.2 Effect of conjugation length and aggregation

The extension of conjugation length in conjugated systems results in a decrease, to some extent, of the energy gap. The conjugation can be increased in a linear 1-dimensional elongation by linking covalently or fusing π-conjugated units, like, for example, in polythiophene[66], poly(para-phenylene)[67] and rylenediimides oligomers[68].

Theoretical calculations clearly show how adding thiophene units decrease the energy gap and, for the rylenediimides, the increase of the degree of annulation by going from perylenediimide to hexarylenediimide leads to a gradual bathochromic shift of the absorption maximum, with an energy gap going form 2.15 eV to 1.25 eV.

Anyway the energy gap of a conjugated system can be lowered by increasing π-conjugation only until a limit point, since the whole system is governed by the effective conjugation length[69].

Inter-molecular effects and aggregation in solid state also play an important role on influencing the energy gap: strong interaction and formation of H- and J- aggregates influence the optoelectronic characteristic such as absorption and charge mobility[70–72].

1.2.3 Donor-Acceptor Approach

A different approach for tuning the energy levels is the use of alternating donor-like (electron donating) and acceptor-like (electron withdrawing) monomers[73,74]. In these systems, called push-pull, the hybridization of energy levels of donor and acceptor increases the HOMO level so that it becomes higher than the one of donor and decreases the LUMO lower than that of the acceptor (Figure 3): the results is a small HOMO-LUMO gap.

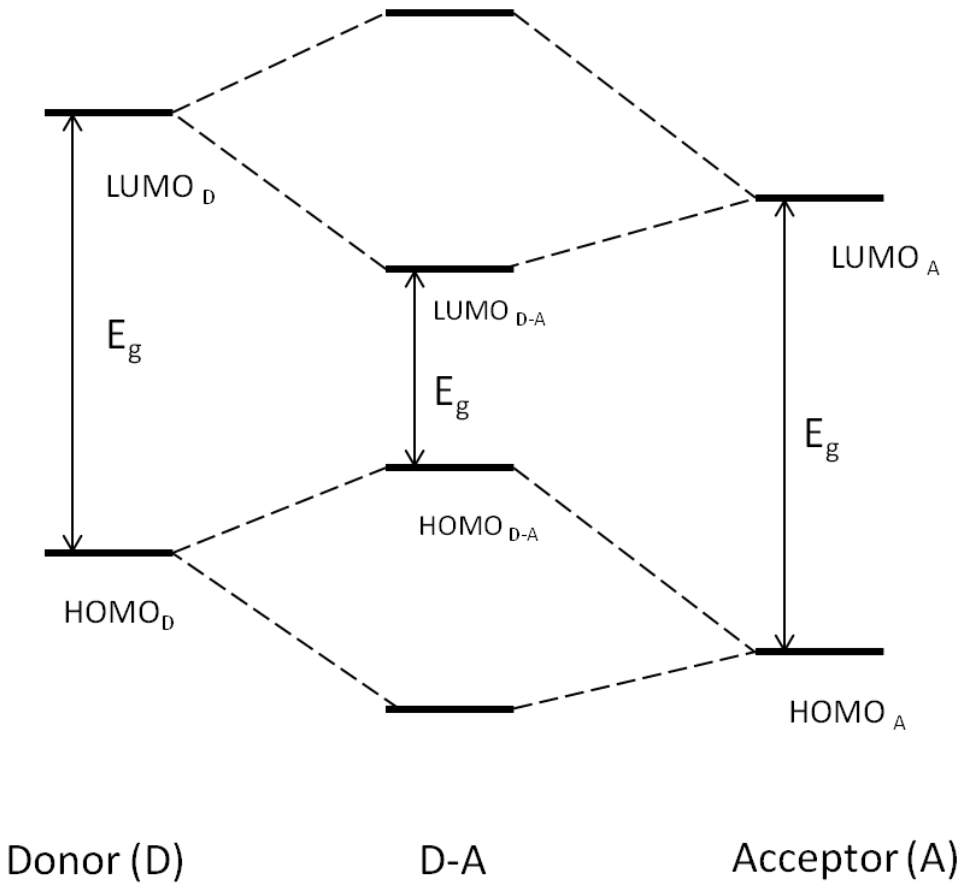

Figure 3. Hybridization of frontier molecular orbitals (HOMO and LUMO) of donor and acceptor units to yield a low bandgap D–A monomer unit.

Depending on the strength of the donor and acceptor monomer, the energy gap can be fine-tuned: in order to get close HOMO LUMO levels, strong acceptor, such as benzothiadiazole and benzobisthiadiazole, and strong donor, such as thienothiophene and benzodithiophene can be used. An important role plays also the spacer linking the donor and acceptor, which can influence the hybridization and as consequence the energy gap[75].

1.3 BODIPY dyes

4,4-Difluoro-4-bora-3a,4a-diaza-s-indacene dyes, more commonly known as BODIPY dyes, have been long since recognized for their excellent optical properties such as high absorption coefficients, high fluorescence quantum

yields, and remarkable photostability[76]. Discovered for the first time in 1968 by Treibs and Kreuz[77], BODIPY dyes are of wide importance and have a broad use as laser dyes in biological sensing, organic electronic, and other possible applications[78–87]. Additionally, straightforward chemical synthesis and structural robustness have enabled fine tuning of optical properties of BODIPY dyes via systematic structural variations[78,83]. The absorption and fluorescence properties depend on the position of substitution (Figure 4), where addition of an electron donating substituent to position 8 does not cause a substantial change of the photophysical behaviour[88], but bulky electron donating groups in positions 2 and 6 cause a large red shift in the absorbance and fluorescence. The effect of an electron withdrawing group is different, with a red shift of the absorbance and fluorescence with addition of the electron withdrawing unit, like a cyano group, to position 8. Addition of a cyano group to positions 2 and 6 causes a smaller change of absorbance and fluorescence wavelength, but it may have a large effect on the fluorescence quantum yield. The presence of bromine atoms in positions 2 and 6 also does not have a substantial effect on the absorbance and fluorescence wavelength[89]. Formation of conjugated systems via positions 2 and 6 also has an effect on the photophysical properties of the BODIPY dyes, showing red-shifted behavior with an increasing degree of conjugation[90,91]. BODIPY compounds blocked by alkyl or aromatic groups show one-electron Nernstian reduction and oxidation waves for the first electron transfer, where the chemical reversibility depends on the character of substitution[92,93]. The stability of anion radicals depends on substitution in position 8, which is subject to nucleophilic attack, while the cation radicals are stabilized by substitution at the 2 and 6 positions, preventing electrophilic attack. Conjugated polymers with on chain BODIPY as well as the corresponding 4-bora-3a,4a,8-triazaindacene core (Aza-BODIPY) can potentially extend the absorption into the deep-red regions of the visible

spectrum and, in some cases, are excellent near-infrared emitters. Aza-BODIPY dyes (Figure 4) contain a nitrogen in the meso (8) position which appears to reduce the HOMO-LUMO energy gap relative to BODIPY dyes bearing similar substituents. The relatively high extinction coefficients of these polymers combined with their photostability make them attractive candidates for various optoelectronic applications

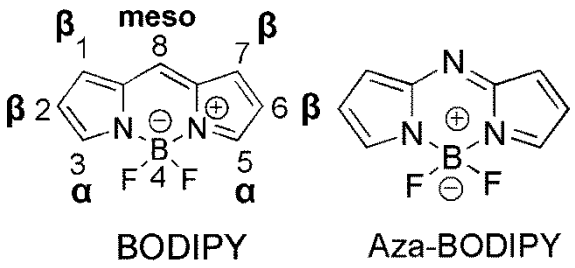

Figure 4. General Chemical Structure of BODIPY and Aza-BODIPY .

As outlined before, in recent years, researchers have showed great interest in low band gap (LBG) organic materials that absorb into the near-infrared (NIR). Even though semiconducting polymers with ultra LBGs have been synthesized before, the design and synthesis of materials with good photoresponse beyond 900 nm and an appreciable PCE in polymer:fullerene solar cells is still a challenge. The key for the design of this polymer is the precise energy level control. The fine tune of energy band gap can be obtained with the donor-acceptor (D-A) approach or the stabilization of aromatic-quinoid structure. D-A approach is the most common tool to synthesize NIR conjugated polymers due to the great amount of functional electron rich and electron deficient building blocks. In order to develop ultra LBG D-A polymers, usually strong electron rich units, like pyrrole, thiophene, ethylenedioxythiophene (EDOT), or bridged bithiophene derivatives and strong electron deficient building blocks, like benzobisthiadiazole, diketopyrrolopyrrole dyes, pyrazinoquinoxaline

derivatives, thiadiazoloquinoxaline derivatives, thienoisoindigo, emeraldicene, or tetraazabenzodifluoranthenediimide are used.

BODIPY small molecules have been recently employed as p-type or donor materials in conjunction with PCBM in bulk heterojunction (BHJ) solar cells thanks to the large extinction coefficients, intense absorption spectra that extend into the red region of the visible spectrum, and decent hole mobility. Also BODIPY-based conjugated polymers have been used in different applications, such as near- IR emitters, light harvesting and OPVs, but only few examples of ultra LBG conjugated polymers (E_g < 1.4-1.5 eV) with BODIPY core have been presented. Actually, Algi and Cihaner designed and synthesized a BODIPY-based polymer for electrochromic applications. In their study, a 1,3,5,7-tetramethyl substituted BODIPY derivative was used as an acceptor unit, featuring a non-planar repeating unit and distorted conjugation between EDOT (strong electron rich) and BODIPY (electron deficient) units due to the steric effect of the methyl groups. To avoid the steric effect of the methyl groups, Vobecka et al.[94] and Samuel et al.[95] have synthesized a BODIPY core with halogens at 3- and 5- positions (α-positions) and effectively synthesized an EDOT-BODIPY-EDOT conjugated polymer both with electro-polymerization and Stille cross coupling polymerization, respectively. However, the resulting copolymers are kinked because the linearity of the polymer was lost. Very recently, Stoddart et al[96]. succeeded to synthesize the first ultra LBG DAD type *α,β*-unsubstituted BODIPY-based copolymer using EDOT as the electron rich (D) unit by electro-polymerization which displays electrochromic behavior.

During the PhD thesis, new LBG conjugated polymers and small molecules based on *α,β*-unsubstituted BODIPY core monomers have been designed and effectively synthesized by conventional cross coupling reaction such as Stille and/or Suzuki coupling.

Chapter 2

2. BODIPY Polymers

2.1 Cross-coupling reactions for the synthesis of BODIPY-based polymers and small molecules

The structure of BODIPY is commonly described as being a boradiazaindacene by analogy with the all-carbon tricyclic ring, but can be also regarded as a cross-conjugated cyanine. The starting point for the synthesis of symmetric (Scheme 1) and asymmetric (Scheme 2) BODIPY unit is the condensation reaction between a highly electrophilic carbonyl compound like an aldehyde and pyrrole, forming a bridge between two pyrrole, followed by oxidation with p-chloranil or dichloro-dicyano-quinone (DDQ) and complexation with boron trifluoride diethyletherate catalyzed by a base (usually a tertiary amine).

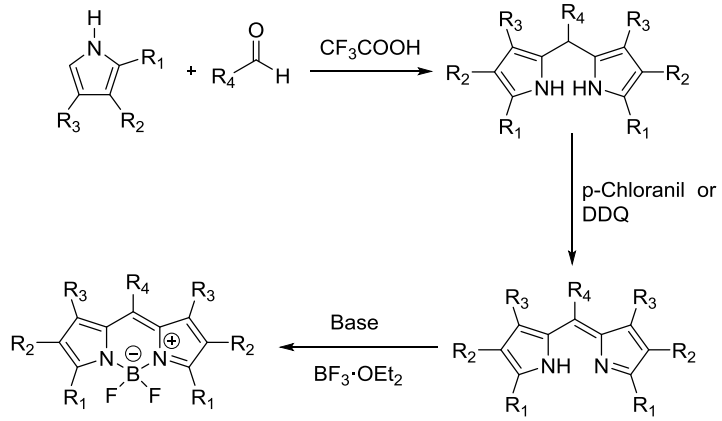

Scheme 1. Synthetic pathway for symmetric BODIPY.

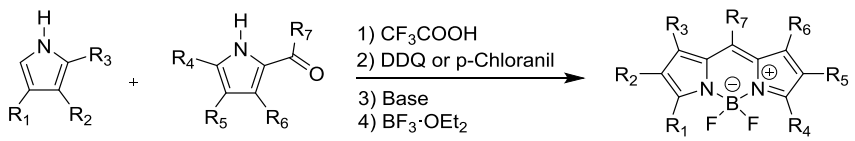

Scheme 2. Synthetic procedure for asymmetric BODIPY.

The BODIPY and aza-BODIPY can be easily modified introducing halogen atom with electrophilic substitution reactions (introduce halogen mainly in 2 and 6 positions) (Scheme 3) or using halogenated dipyrromethene precursors (Scheme 4).

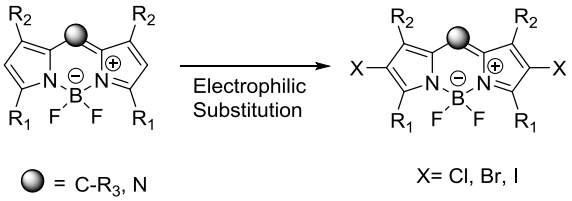

Scheme 3. Halogenation of BODIPY core by electrophilic substitution.

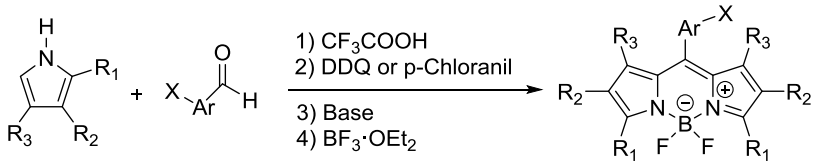

Scheme 4. Halogenation of BODIPY starting from halogenated precursors.

The halogenation of BODIPY in α or β positions open many possibilities not only in the field of small molecule semiconductors[38], but also in the polymers one. The halogenated BODIPYs will be suitable to undergo nickel-catalyzed cross coupling polymerization reaction such as Yamamoto coupling as well as palladium-catalyzed cross coupling reactions, like Sonogashira, Heck, Stille or Suzuki coupling (Scheme 5)[97], facilitating the extension of π-conjugation length and building more complex structures.

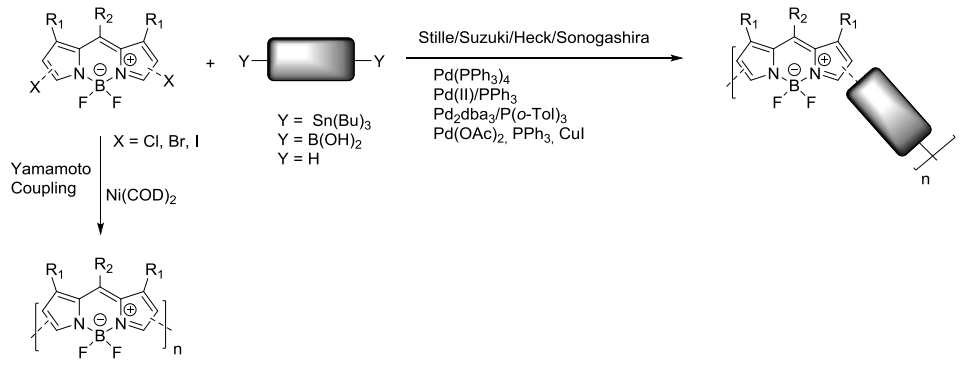

Scheme 5. Nickel and Palladium-catalyzed cross coupling reaction suitable for halogenated BODIPY core.

In this chapter, the synthesis and the optoelectronic characterization of novel ultra LBG polymers consisting of *α,β*-unsubstituted *meso* positioning BODIPY as building block are presented (Figure 5).

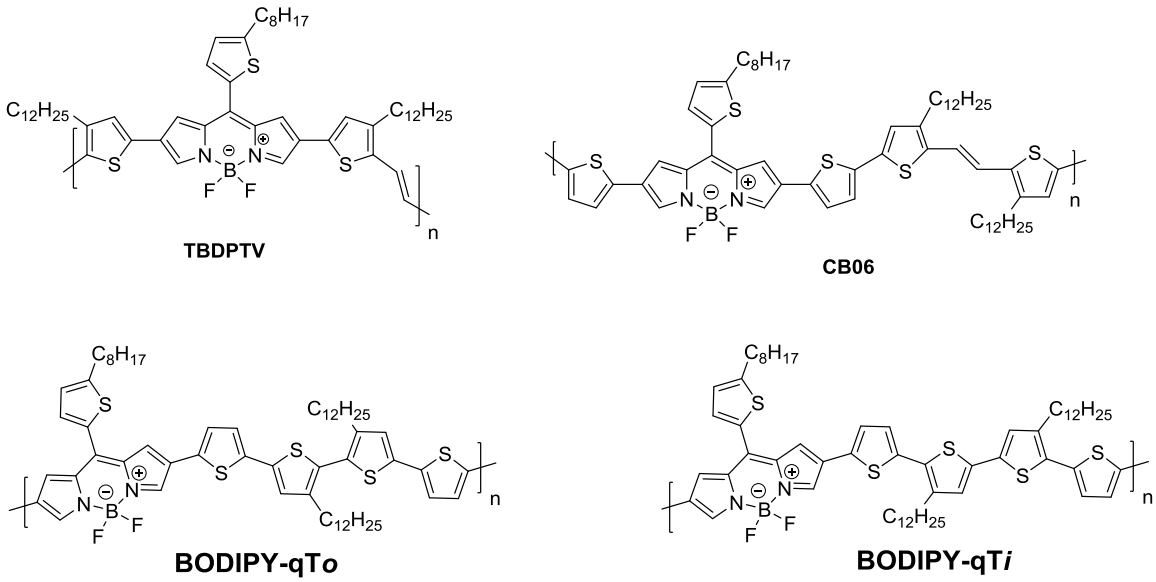

Figure 5. *α,β*-unsubstituted *meso* positioning BODIPY-based polymers.

2.2 Results and discussion

2.2.1. Theoretical calculations

The development of BODIPY-based organic semiconductors and especially those of the *α,β*-unsubstituted forms has so far lagged behind that of other *π*-deficient units, mainly because of stability issues during the synthesis. However, thanks to a recently developed synthetic protocol[37], a stable *α,β*-unsubstituted BODIPY functionalized solely on the *meso* position with a thienyl group has been successfully synthesized (Scheme 8) and integrated into more complex structures. The structural and electronic properties of the recently developed building block along with its structural analogues containing dimethyl substituents at the *α*-positions and tetramethyl substituents at the *α,β*-positions were determined via quantum chemical density functional theory (DFT) calculations utilizing the B3LYP/6-

311G(d,p) as the model basis set and the results are presented in Figure 6. As shown in Figure 6, on the one hand the π-electron density of the highest occupied molecular orbital energy level (E_{HOMO}) of all the three studied BODIPY monomers is found to be delocalized only on the dipyrromethene core (without the participation of the N-B(F2)-N sequence) along with the methyl groups in the case of the α-substituted *meso*-positioning thienyl BODIPY and the α,β-substituted *meso*-positioning thienyl BODIPY. On the other hand, the π-electron density of the lowest unoccupied molecular orbital energy level (E_{LUMO}) is not only distributed throughout the boron-dipyrromethene core but is also found to be extended towards the *meso*-thienyl unit as the methyl substitution decreases. In addition, it is evident that as the number of the methyl substituents decreases both the E_{HOMO} and E_{LUMO} levels are downshifted *vs* vacuum due to the elimination of the σ-inductive effect of the methyl groups, but no significant variation is detected on the calculated E_{HOMO}-E_{LUMO} gap. Furthermore, the subsequent exclusion of the methyl substituents from the α- and β-positions leads to the reduction of the dihedral angle between the boron dipyrromethene core and the *meso*-thienyl unit from 89.8^{o} for the α,β-substituted *meso*-positioning thienyl BODIPY to 50.7^{o} for the α-substituted *meso*-positioning thienyl BODIPY and finally to 47.3^{o} for the α,β-unsubstituted *meso*-positioning thienyl BODIPY. The reduction of the dihedral angle, especially in the α,β-unsubstituted *meso*-positioning thienyl BODIPY, could contribute to the efficient π-π stacking and C-H$\cdots\pi$ interactions when this building block would be integrated into π-conjugated polymer backbones.

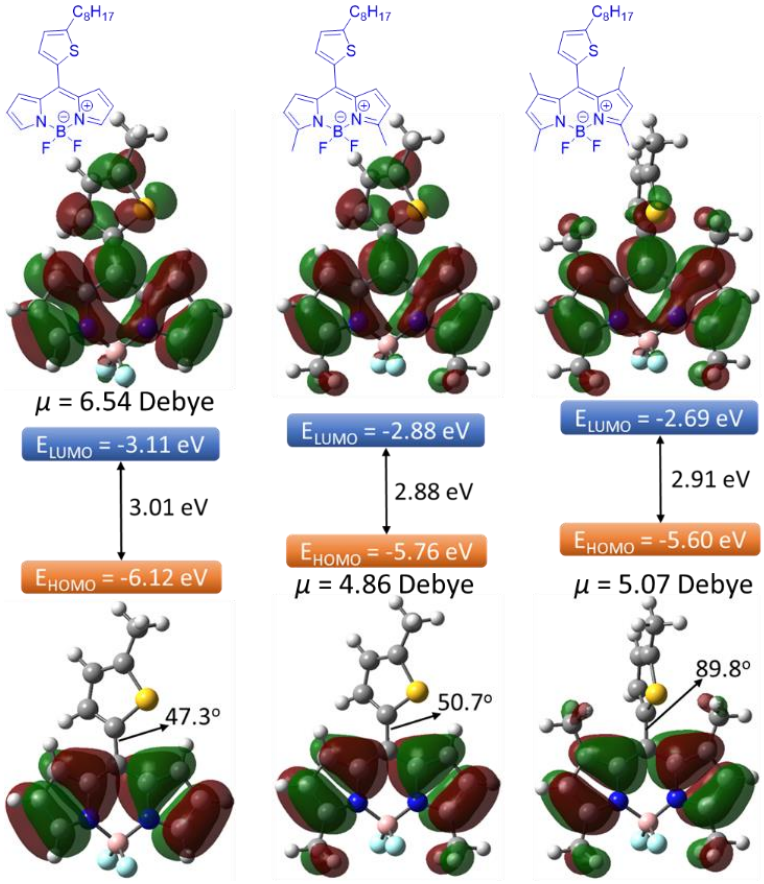

Figure 6. Calculated frontier molecular orbital (E_{HOMO}/E_{LUMO}) levels, molecular dipole moments (μ), dihedral angles between the boron dipyrromethene core with the *meso*-thienyl ring and pictorial representations of the model monomers *α,β*-unsubstituted *meso*-positioning thienyl BODIPY, *α*-substituted *meso*-positioning thienyl BODIPY and the *α,β*-substituted *meso*-positioning thienyl BODIPY (B3LYP/6-311G(d,p) level of theory).

The dipole moment (μ) of the *α,β*-unsubstituted *meso*-positioning thienyl BODIPY (6.54 D) is higher than those of the *α*-substituted BODIPY (4.86 D) and the *α,β*-substituted BODIPY (5.07 D). The μ of the *α,β*-unsubstituted meso-positioning thienyl BODIPY (6.54 D) is higher than that of the *α,β*-substituted BODIPY (5.07 D) due to the absence of the methyl groups that decrease the electron affinity of the BODIPY core through their *σ*-inductive effect. In addition, the symmetric *α,β*-unsubstituted and *α,β*-substituted meso-positioning thienyl BODIPY monomers present higher μ than the asymmetric *α*-substituted BODIPY (4.86 D). Therefore, the higher μ value of the *α,β*-unsubstituted *meso*-positioning thienyl BODIPY is expected to enhance the backbone-ordering and as a consequence the crystallinity of the

corresponding π-conjugated polymer thin films as a result of strong dipolar interactions[52].

2.2.2. Synthesis of *α,β*-unsubstituted *meso* positioning BODIPY precursors

The easiest way to synthesize *α,β*-unsubstituted BODIPY dyes is the combination of aldehydes and pyrrole under neat conditions. The aldehyde can be dissolved in excess pyrrole at room temperature, and the dipyrromethane intermediate (the reduced form of the dipyrromethene) is formed and isolated. The BODIPY core can then be obtained after oxidation and complexation with boron. During the PhD thesis, 5-octylthiophene-2-carbaldehyde has been chosen as the aldehyde, and upon condensation with pyrrole, catalyzed by few drops of trifluoroacetic acid, the resulting 2,2'-((5-octylthiophen-2-yl)methylene)bis(1H-pyrrole) (1) is obtained (Scheme 6).

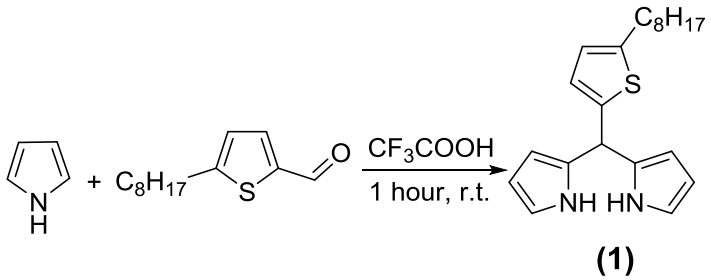

Scheme 6. Synthesis of 2'-((5-octylthiophen-2-yl)methylene)bis(1H-pyrrole).

We decided to choose alkylthiophene-carbaldehyde in order to have the formation of a functional BODIPY building block (3) with a 2D extension for the development of a series of BODIPY based copolymers soluble in common organic solvents. Treatment of monomer 1 with the strong oxidant 2,3-dichloro-5,6-dicyano-1,4-benzoquinone (DDQ), then diisopropylethylamine (Hünig's base) and finally with trifluoroborane dietherate [$BF_3O(Et)_2$] provided the corresponding borondipyrromethene monomer 2 (Scheme 7).

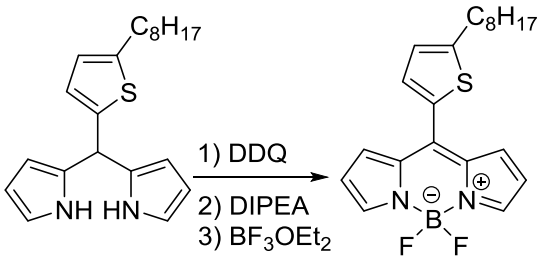

(2)

Scheme 7. Synthesis of 8-octylthiophene BODIPY.

New protocols to introduce bromine in 2- and-6 positions on the unsubstituted BODIPY core has been presented in the literature by Shinokubo et al.[98] and Zhang et al.[99] In our case, the targeted dibromo borondipyrromethene monomer 3 is synthesized upon bromination with N-bromosuccinimide (NBS) using dimethylformamide (DMF):methylene chloride (CH_2Cl_2) 1:1 as the solvent mixture similar to the conditions presented by Stoddart et al.[96] (Scheme 8).

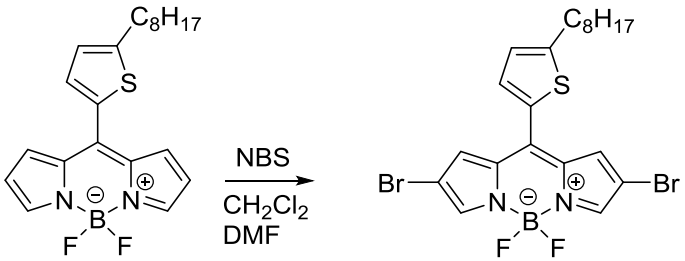

(3)

Scheme 8. Synthesis of 2,6-dibromo-8-octylthiophene BODIPY.

Then, Stille cross coupling reaction between monomer 3 and the commercial avaible 2-(tributylstannyl)thiophene using as catalyst tris(dibenzylideneacetone)dipalladium(0) [$Pd_2(dba)_3$] and tri-o-tolylphosphine [P(*o*-Tol)$_3$] in inert atmosphere and dry toluene provide monomer 4 (Scheme 9). The purified monomer 4 then was brominated, following a classical protocol, with NBS in DMF, in order to provide the functional monomer 5 (Scheme 9).

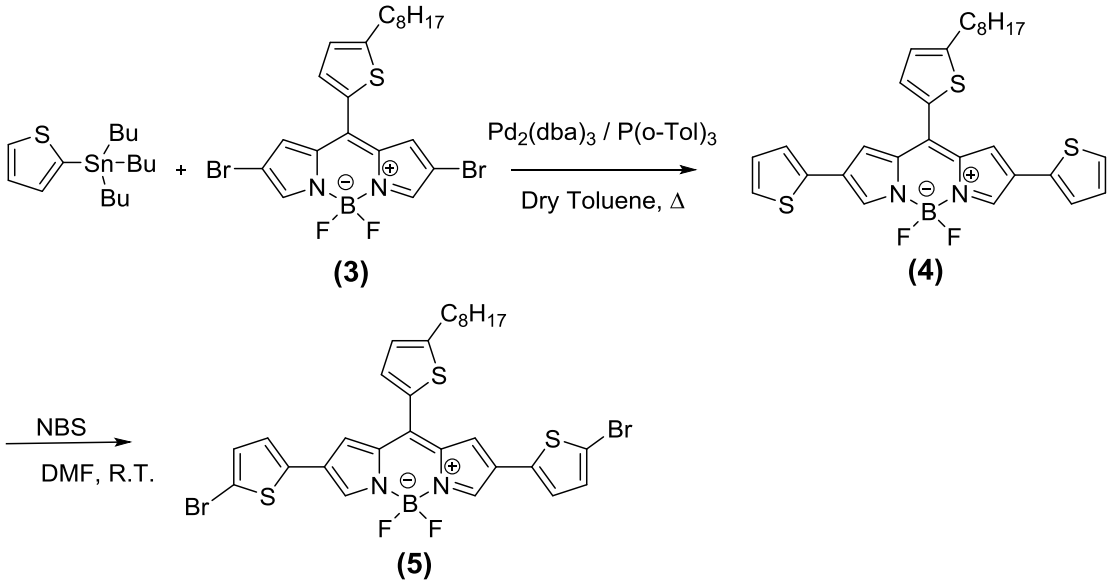

Scheme 9. Synthesis of monomer 5.

2.2.3 Synthesis of polymers

2.2.3.1 Synthesis of TBDPTV

TBDPTV was synthesiszed through Stille cross-coupling polymerization using 1:1 monomer feed ratios (Scheme 10). A solution of the commercially available (E)-1,2-bis(3-dodecyl-5-(trimethylstannyl)thiophen-2-yl)ethene and the dibromo borondipyrromethene monomer 3 were combined in dry deoxygenated toluene in the presence of $Pd_2(dba)_3$ (5 mol%) and $P(o\text{-}Tol)_3$ (40 mol%) and the mixture was heated to ca. 120°C for 48 h to provide the desired crude polymer. Purification was achieved by Soxhlet extraction with methanol (200 mL, 1 d), hexane (200 mL, 1 d) and chloroform (200 mL, 1 d). The chloroform fraction was then concentrated under reduced pressure, precipitated in methanol, filtered and dried in vacuum. Polymer TBDPTV is readily soluble in chloroform, chlorobenzene and o-dichlorobenzene (o-DCB). The typical molecular weight characteristics of TBDPTV were estimated by GPC and are presented in Table 2.

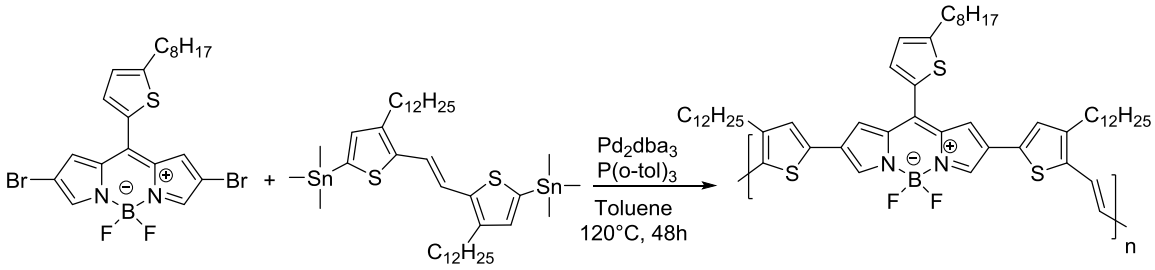

Scheme 10. Synthesis of TBDPTV.

2.2.3.2 Synthesis of BODIPY-qT*o* and BODIPY-qT*i* and CB06

Stille coupling mediated polymerisation ([$Pd_2(dba)_3$] (2 mol %), [P(*o*-tol)$_3$] (4 mol %) in toluene at *ca*. 120 °C for 48 h) was used to combine the BODIPY precursor 5 (Figure 6) with readily available (3,3'-didodecyl-2,2'-bithiophene-5,5'-diyl)bis(trimethylstannane) or (4,4'-didodecyl-2,2'-bithiophene-5,5'-diyl)bis(trimethylstannane) or (*E*)-1,2- bis(3-dodecyl-5-(trimethylstannyl)thiophen-2-yl)ethene to provide the polymers BODIPY-qT*o*, BODIPY-qT*i* and CB06, respectively (Scheme 11).

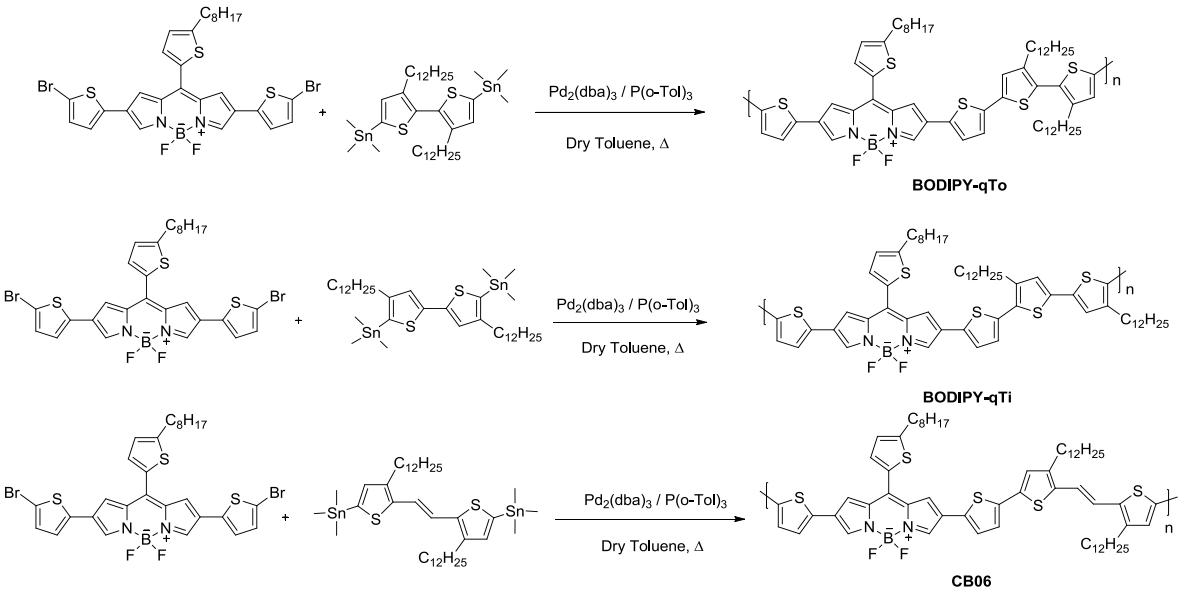

Scheme 11. Synthesis of polymers BODIPY-qT*o*, BODIPY-qT*i* and CB06.

The crude polymers as received from the reaction mixtures were purified by successive Soxhlet extractions and they were collected by precipitation from the chloroform (CF) fraction (BODIPY-qT*o*) and chlorobenzene (CB) fraction (BODIPY-qT*i*, CB06). The resulting polymers are soluble in chloroform, chlorobenzene and *o*-dichlorobenzene (*o*-DCB). The average molecular weights $\overline{M_n}$, $\overline{M_w}$ and the polydispersity (*Đ*) of the polymers were measured by GPC based on monodispersed polystyrene standards at high temperature (150 °C) with 1,2-dichlorobenzene (DCB) as eluent for BODIPY-qT*o* and BODIPY-qT*i*, while the GPC analysis for CB06 was performed at 30°C using chloroform as eluent (Table 2). Both BODIPY-qT*o* and BODIPY-qT*i* show monomodal GPC profiles with no appearance of residual monomers or oligomer chains. BODIPY-qT*o* exhibits $\overline{M_n}$ of 72000 g/mol, with *Đ* of 1.57, which is significantly higher than that of BODIPY-qTi ($\overline{M_n}$ = 22400 g/mol, with *Đ* = 1.74). Since that BODIPY-qT*i* is received from the CB fraction it seems that anchoring the didodecyl side chains on the i-positions prevent the easy solubility of the polymer chains in common organic solvents, which could explain the lower $\overline{M_n}$ of BODIPY-qT*i*.

Table 2. Molecular Characteristics of TBDPTV, BODIPY-qT*o*, BODIPY-qT*i* and CB06.

Polymer	***Mn* (g/mol)**	***Mw* (g/mol)**	***Đ***	***Polymerization Degree***
TBDPTV	13700	70300	5.1	15
BODIPY-qT*o*	72000	113000	1.6	69
BODIPY-qT*i*	22400	40000	1.7	21
CB06	4500	10800	2.4	4

2.2.4 Electrochemical Characterization

The energy levels of TBDPTV have been determined with both cyclic voltammetry (CV) and atmospheric pressure photoelectron spectroscopy (AAPPS) (Figures 7 and 8).

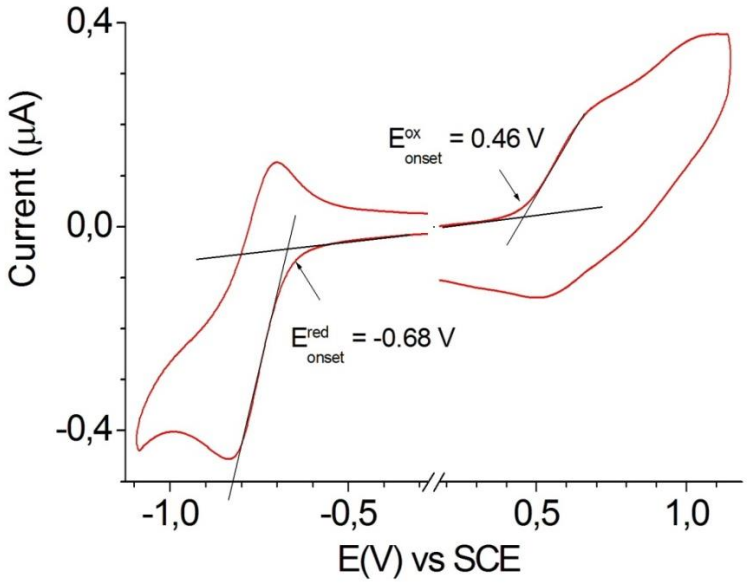

Figure 7. Cyclic voltammogram of TBDPTV in chloroform (containing 0.1 M tetrabutylammonium perchlorate).

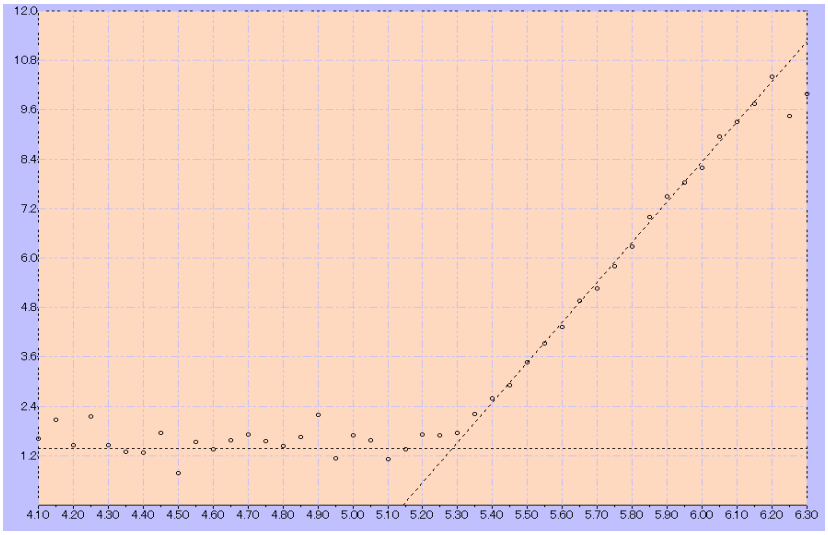

Figure 8. HOMO energy level of TBDPTV estimated by atmospheric pressure photoelectron spectroscopy.

The reduction and oxidation versus saturated calomel electrode (SCE) of TBDPTV are, respectively, at -0.68 V and 0.46 V (Figure 7). The resulting

HOMO (E_{HOMO}) and LUMO (E_{LUMO}) energy levels as calculated from the equations $E_{HOMO} = -(4.7 + E_{onset}^{ox})$ eV and $E_{LUMO} = -(4.7 + E_{onset}^{red})$ eV are -5.16 eV and -4.02 eV vs. vacuum, respectively. The electrochemical bandgap (E_g^{CV}) of 1.14 eV is in excellent agreement with the E_g^{opt} (Table 3 at page 27). The HOMO level as calculated by AAPPS is situated at -5.29 eV, slightly different from the one obtained by cyclic voltammetry.

Also for BODIPY-qT*i* and BODIPY-qT*o*, cyclic voltammetry has been performed (Figure 9). Both BODIPY-qT*i* and BODIPY-qT*o* exhibit reversible oxidation and reduction peaks. It is demonstrated that the oxidation and reduction potentials of the polymers are alkyl side chain positioning dependent.

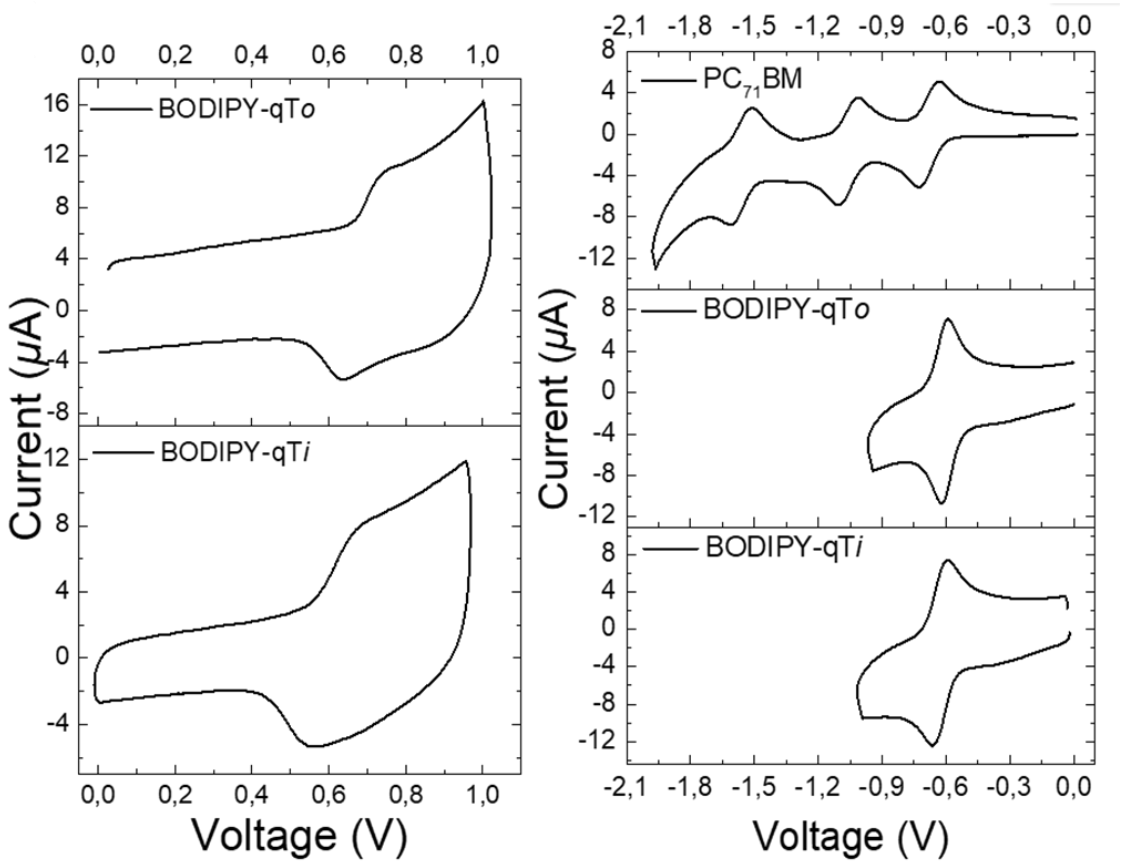

Figure 9. BODIPY-qTi, BODIPY-qTo and PC71BM cyclic voltammetry graphs during oxidation (left) and reduction (right).

BODIPY-qT*i* and BODIPY-qT*o* present oxidation/reduction potentials at 0.62 V/-0.63 V vs saturated calomel electrode (SCE) the former and at 0.69 V/-0.61 V vs SCE the latter. These lead to E_{HOMO}/E_{LUMO} levels at -5.32 eV/-4.07 eV for the BODIPY-qT*i* and at -5.39 eV/-4.09 eV for the BODIPY-qT*o* vs vacuum resulting to very low E_g^{CV} of 1.25 eV for the BODIPY-qT*i* and of 1.30 eV for the BODIPY-qT*o*. The obtained E_g^{CV} of the polymers are increased by 0.05 eV than their corresponding E_g^{opt} (Table 3) in agreement with recently reported results on other polymer systems[100]. It is obvious that when the didodecyl side chains are anchored onto the tail-to-tail (TT) positioning both the E_{HOMO}/E_{LUMO} levels are upshifted as compared to BODIPY-qT*o*. A tentative explanation for the lower lying E_{HOMO}/E_{LUMO} levels of BODIPY-qT*o* can be attributed to the steric constraints that prevent planarity of the quaterthiophene segment when the didodecyl alkyl chains of the two central thiophene units are anchored in the head-to-head (HH) positioning. For comparison the reduction potentials of the well-known organic semiconductor fullerene derivative [6,6]-phenyl-C_{71}-butyric acid methylester ($PC_{71}BM$) with strong electron withdrawing characteristics have also been determined by CV. $PC_{71}BM$ presents three reversible reduction peaks at -0.68 V, -1.06 V and -1.56 V vs SCE that are attributed to E_{LUMO} (-4.02 eV), E_{LUMO+1} (-3.64 eV) and E_{LUMO+2} (-3.14 eV), respectively. These results show that the E_{LUMO} levels of BODIPYqT*i* and BODIPY-qT*o* are lying lower by 0.05 eV (BODIPY-qT*i*) and 0.07 eV (BODIPY-qT*o*) as compared to $PC_{71}BM$. The combined low E_{LUMO} levels and small bandgaps (E_g^{CV} and E_g^{opt}) are indicative of the highly electron-deficient and π-conjugated nature of the *α,β*-unsubstituted *meso*-positioning thienyl BODIPY. These are among the lowest E_{LUMO} levels reported to date for a semiconducting polymer comparable to those of the 2,2′-(bisindenofluorene-12,15-diylidene) dimalononitrile-based quaterthiophenes[101,102] and

approaching those of air-stable n-channel core-cyanated perylene-, anthracene- and naphthalene-based small molecule semiconductors[103–105].

Figure 10 show the predicted E_{HOMO} and E_{LUMO} levels as well as the distribution of the frontier molecular orbitals of the BODIPY-qT*i* and BODIPY-qT*o*.

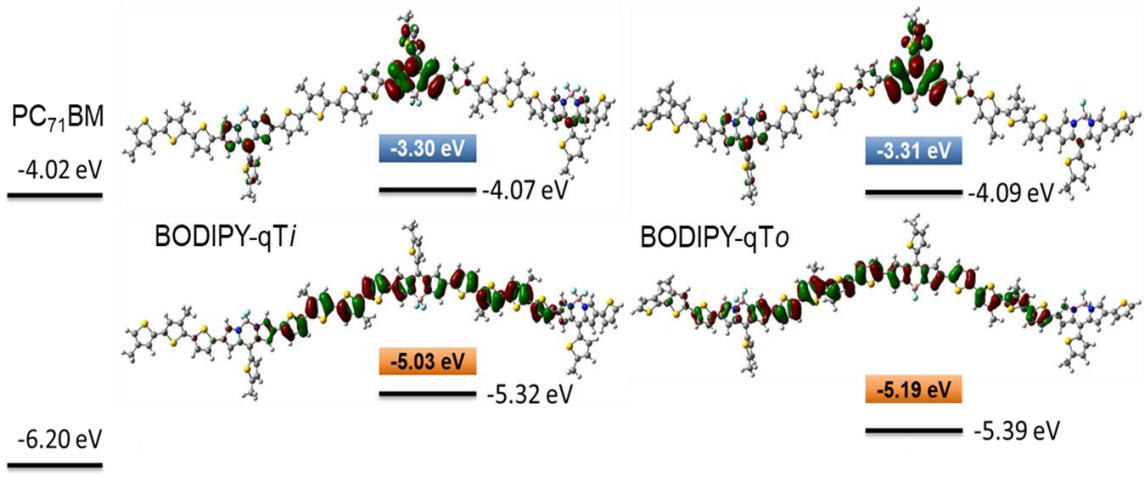

Figure 10. Schematic illustration of the calculated frontier molecular orbital E_{HOMO} (orange band) and E_{LUMO} (blue band) levels variation and pictorial representations of the trimer model compounds BODIPY-qT*i* and BODIPY-qT*o* (B3LYP/6-311G(d,p) level of theory) and with black lines the experimentally determined E_{HOMO}/E_{LUMO} levels of BODIPY-qT*i*, BODIPY-qT*o* and $PC_{71}BM$.

It is possible to observe that in BODIPY-qT*i* and BODIPY-qT*o* the E_{HOMO} levels are fully delocalized along the polymer chain axis in contrast to the significant localization of the E_{LUMO} on the *α,β*-unsubstituted *meso*-positioning thienyl BODIPY along with a good agreement in the variation between the theoretically predicted and the experimentally determined E_{HOMO} and E_{LUMO} levels.

2.2.5 Optical Characterization

The normalized UV–vis absorption spectra of TBDPTV, CB06, BODIPY-qT*o* and BODIPY-qT*i* in chloroform solution and in the solid state were measured and presented in Figures 11-13, whereas the corresponding optical

properties are summarized in Table 3. All the polymers show two major absorption bands, both in solution and in solid state, a feature commonly observed for alternating D-A copolymers. The low-wavelength peak observed can be attributed to a π-π* transition, while the high-wavelength transition with is believed to be related to an intramolecular charge transfer (ICT) between the electron donating and the electron deficient groups of the repeating unit. Focusing on TBDPTV (Figure 11), by passing from solution to the solid state, the absorption spectrum becomes broader covering all the range from 300 nm to 1100 nm and all the absorption bands are redshifted. The peak at 444 nm in solution is situated at 451 nm in the solid state, whereas the peak at 817 nm in solution has been shifted to 848 nm in the solid state, indicating the presence of strong intermolecular π-π interactions. The optical band gap (E_g^{opt}) calculated from the absorption onset in the solid state is estimated at 1.15 eV.

Table 3. Absorption maxima and energy gap of polymers TBDPTV, BODIPY-qT*o*, BODIPY-qT*i* and CB06.

Polymer	**λ_{max}^{sol} (nm)**	**λ_{max}^{film} (nm)**	**E_g^{opt} (eV)**
TBDPTV	444, 817	451, 848	1.15
BODIPY-qT*o*	424, 715	415, 739	0.98
BODIPY-qT*i*	426, 739	446, 782, 877	0.85
CB06	462, 762	484, 794	1.24

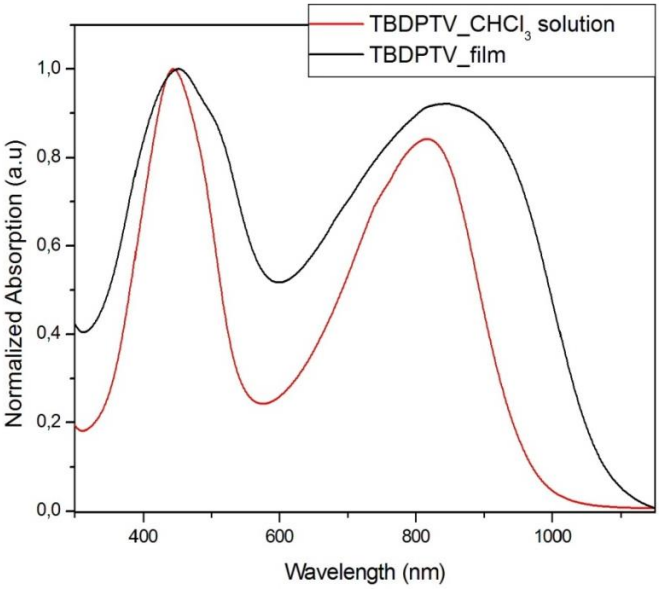

Figure 11. UV-vis Absorption spectra in chloroform solution and as thin film of TBDPTV.

The chemical structure of CB06 is similar as to TBDPTV, but with one more thiophene unit between the BODIPY and the bis(3-dodecyl-thiophen-2-yl)ethene. Compared to TBDPTV, CB06 absorption maxima, both in solution (462 nm and 762 nm) and solid state (484 nm and 794 nm), on the one hand is red shifted at the low wavelength band as a result of the extension of the π-conjugation along the polymer backbone induced by one more thiophene. On the other hand, the high wavelength band is blue shifted in agreement with the finding from a recent work[106] in which it is reported that the stronger the coupling between the D and A moieties or the shorter the conjugation length between two electron withdrawing units within the polymer chain, the higher is the wavelength of the maximum absorption. The estimated E_g^{opt} is 1.25 eV slightly higher than that of TBDPTV.

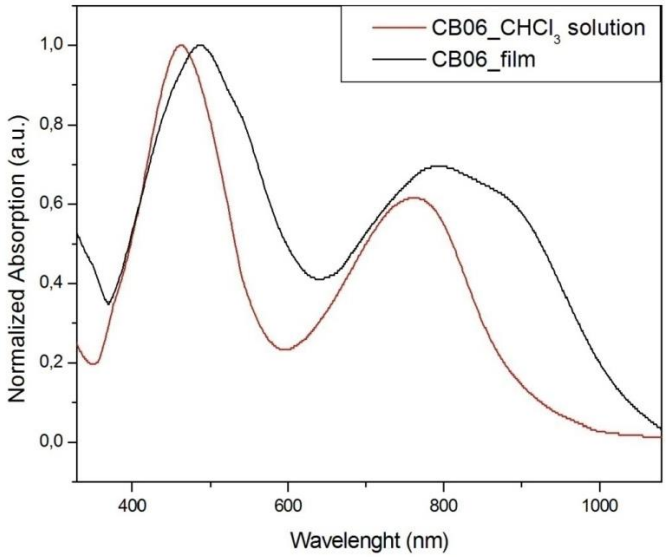

Figure 12. UV-vis spectra of CB06 in chloroform solution and as thin film.

BODIPY-qT*i* and BODIPY-qT*o* show qualitatively similar spectral shape with two well resolved vibronic transitions (Figure 13). The low-wavelength peak observed at 426 nm for BODIPY-qT*i* and at 424 nm for BODIPY-qT*o* can be attributed to the polymers backbone π-π* transition while the high-wavelength transition at 739 nm for BODIPY-qT*i* and at 715 nm for BODIPY-qT*o* is related to an intramolecular D-A charge transfer excitation.

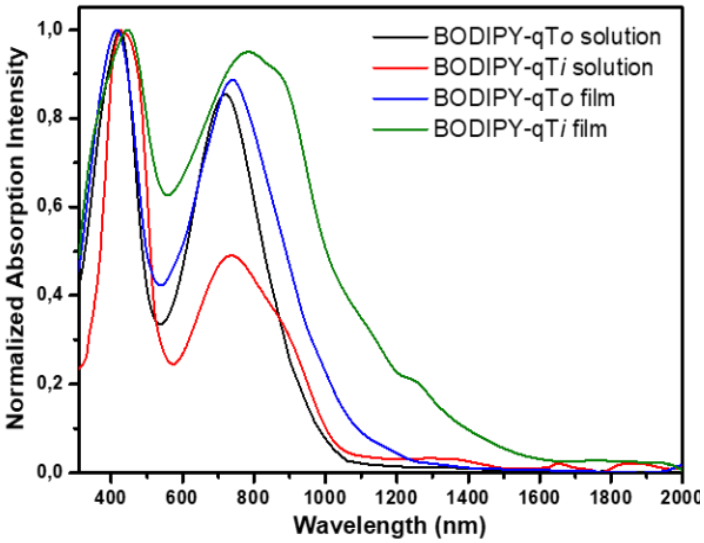

Figure 13. UV-vis spectra of BODIPY-qT*i* and BODIPY-qT*o* polymers in chloroform solution and as films.

Polymer BODIPY-qT*i* presents two additional low absorption bands between 1600 and 1800 nm. This absorption peaks could be attributed to some weak electronic transitions from interchain interactions but more experiments and studies are needed to support this assumption.

Passing from solution to the solid state, both the low- and high- wavelength absorption peaks of BODIPY-qT*i* and BODIPY-qT*o* are red shifted with respect to their solution spectra, except for the low wavelength absorption peak of BODIPY-qT*o* (Table 3). This supports the efficient π-π stacking of the polymer chains of BODIPY-qT*i* passing from solution to the solid state. In general, the same trends observed in solution for the BODIPY-qT*i* and BODIPY-qT*o* regarding the variation of the absorption maxima of both the low and high wavelength peaks were also observed in the solid state studies (446/782 nm for BODIPY-qT*i* and 415/739 nm for BODIPY-qT*o*). However, BODIPY-qT*i* reveals a pronounced absorption peak at longer wavelength (877 nm), a signature of a vibronic feature which denotes enhanced aggregate formation similar to that observed in regioregular poly(3-hexylthiophene) thin films, indicating a more ordered structure.[55] Furthermore, the E_g^{opt} of BODIPY-qT*i* and BODIPY-qT*o* (Table 3) support that these polymers are ultra LBG polymeric semiconductors. The E_g^{opt} of BODIPY-qT*i* (0.85 eV) is lower by 0.13 eV than that of BODIPY-qT*o* (0.98 eV). Therefore, when the didodecyl side chains are anchored onto the HH positions in BODIPY-qT*o* the absorption peak maxima both in solution and in solid state appear at lower wavelengths and the E_g^{opt} is higher as compared to BODIPY-qT*i*, indicating a higher degree of steric hindrance and polymer chain distortion.

To support our assumption quantum chemical DFT calculations were performed to estimate the dihedral angles, predict the molecular energy levels and model the distribution of the frontier molecular orbitals of the BODIPY-qT*i* and BODIPY-qT*o*. The DFT calculations using the B3LYP/6-

311G(d,p) performed on trimer model compounds and the chemical structures of the BODIPY-qT*i* and BODIPY-qT*o* as obtained by the theoretical calculations are presented in Figure 14 and the estimated dihedral angles in Table 4.

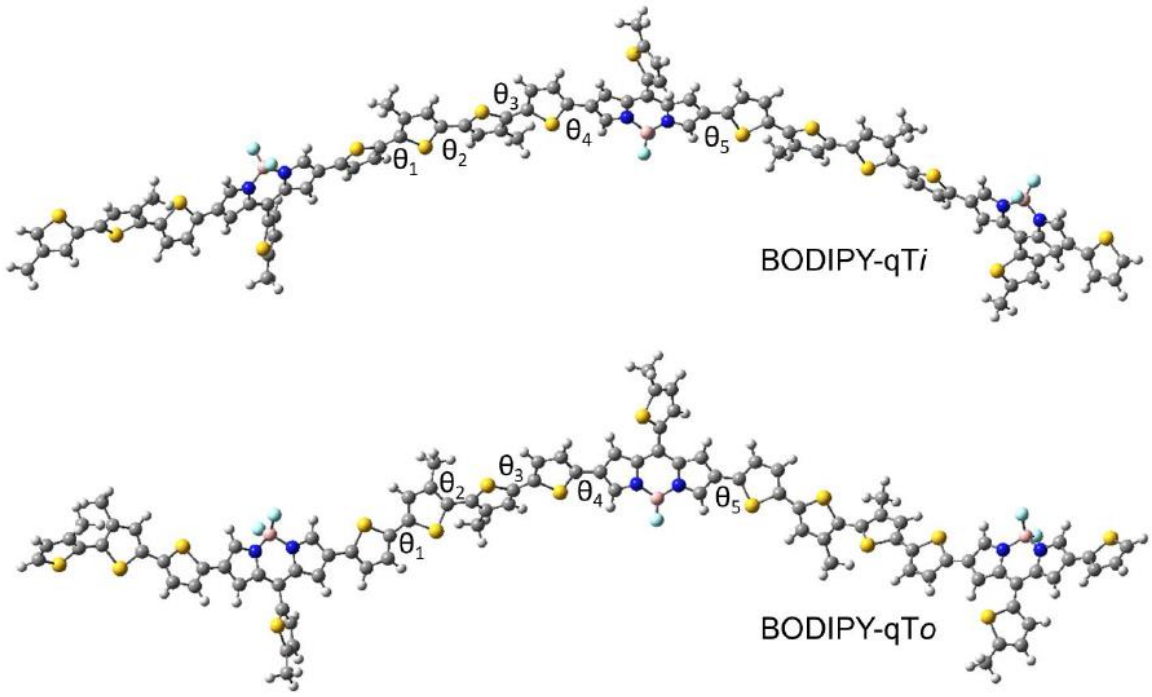

Figure 14. Ground state geometry optimizations of BODIPY-qT*i* and BODIPY-qT*o*. Color scheme: carbon, gray; nitrogen, blue; sulfur, orange; boron, pink; fluorine, cyan. Optimized structures calculated using DFT at the B3LYP/6-311G(d,p) level of theory. θ_1, θ_2, θ_3, θ_4 and θ_5 are the calculated dihedral angles.

Table 4 Calculated dihedral angles (θ_1, θ_2, θ_3, θ_4 and θ_5) of some representative bonds that are shown in Figure 14 for BODIPY-qT*i* and BODIPY-qT*o* polymers.

	θ_1	θ_2	θ_3	θ_4	θ_5
BODIPY-qT*i*	33.2°	20.9°	30.5°	18.1°	16.8°
BODIPY-qT*o*	23.8°	63.4°	21.4°	19.2°	20.1°

The obtained results show that BODIPY-qT*i* and BODIPY-qT*o* present comparable estimated dihedral angles except in the case of θ_2 dihedral angle

where the rotation between the adjacent units in BODIPY-qTo is 63.4° as compared to 20.9° in BODIPY-qT*i*. The lower θ_2 dihedral angle between the adjacent didodecyl thiophene rings of BODIPY-qT*i* results in reduced steric hindrance along the axis when the didodecyl alkyl chains are anchored in the *i*-positions, which is beneficial towards enhanced optoelectronic and charge transporting properties[107,108]. These findings are in agreement with the aforementioned observation on the absorption maxima and E_g^{opt} variation for BODIPY-qTi and BODIPY-qTo.

The research group of Dr. Stratakis from IESL, Heraklion Crete, has performed also the micro-photoluminescence (μPL) measurements. μPL experiment is a photoluminescence experiment with spatial resolution and it allows to study any nanostructures and/or defects and in our case to examine if the studied polymer thin films present any type of aggregation (ordering). The spectra of both polymers are presented in Figure 15 .

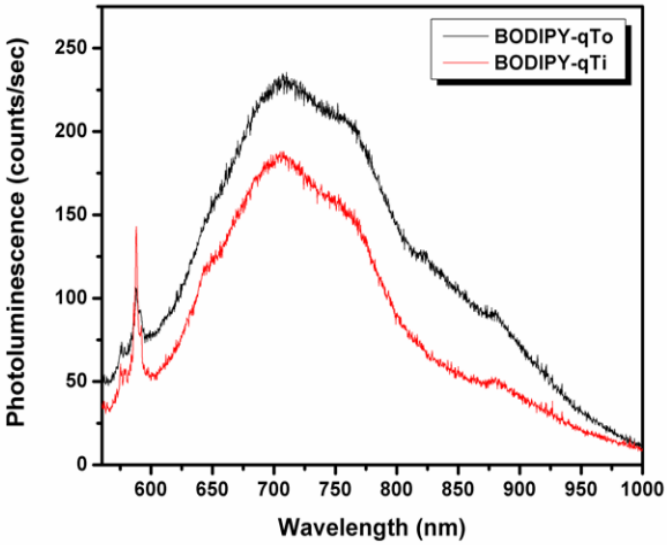

Figure 15. Room temperature μPL spectra following excitation at 543 nm of the BODIPY-qT*o* (black line) and BODIPY-qT*i* (red line) polymers.

While it is possible to observe significant quenching (~20%) for the BODIPY-qT*i* polymer relative to the BODIPY-qT*o* one, no significant μPL peak shift is noticed. This finding is rationalized if one considers the better

π-π stacking of the BODIPY-qT*i* polymer chains due to the reduced steric hindrance as compared to the BODIPY-qT*o*. Notably, the sharp peak at ca. 590 nm (2.1 eV) corresponds to the Raman signature of the symmetric vibration, ν_s(C=C), of the carbon-carbon double bond within the thiophene ring at 1450 cm^{-1}.

The pristine polymers BODIPY-qT*o* and BODIPY-qT*i* were also studied by means of transient absorption spectroscopy (TAS) in order to examine the photo-excitation dynamic processes that occur following 1026 nm laser excitation. It is worth to mention that at least two-photon absorption is used in order to excite these polymers, because the energy of the employed fundamental wavelength, i.e. 1026 nm, is lower than the energy an electron needs to move from the E_{HOMO} to E_{LUMO} of the polymers in question. Figures 16a and 16b present the normalized delta optical density (ΔOD) vs. wavelength, for the two polymers studied (BODIPY-qT*o* and BODIPY-qT*i*) as a function of time, i.e. following photo-excitation at t=0 fs.

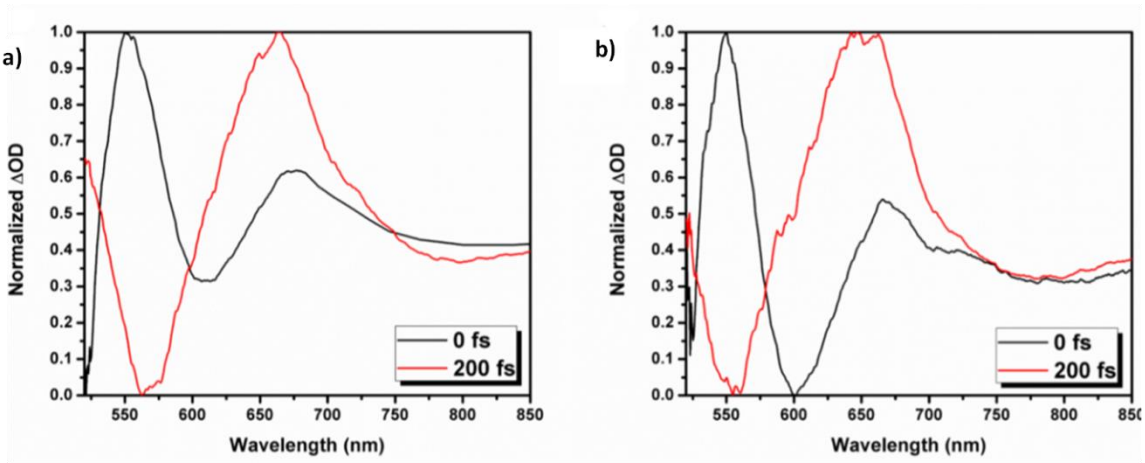

Figure 16. Normalized optical density vs. wavelength plots at various time delays of BODIPY-qTo (a) and BODIPY-qTi (b), following photo-excitation at 1026 nm with a pump fluence of 1.5 mJ cm^{-2}.

For both polymers the transient photo-induced absorption (ΔOD) peak shifts to higher wavelengths, i.e. lower energies, as time progresses. Namely, within 200 fs, the BODIPY-qT*o* polymer peak shifts from 550 to 663 nm,

while the corresponding peak of BODIPY-qT*i* polymer shifts from 550 to 646 nm. This ultrafast red shift in both polymers is attributed to temporal post photo-excitation phenomena such as thermalization of the electrons and holes to the edge of the conduction and valence band, as well as, to the internal vibrational and rotational relaxations within the excited states.

2.2.6 Charge Transporting Properties of BODIPY-qT*o* and BODIPY-qT*i*

The research group of Prof. Thomas Anthopoulos from Imperial College has investigated the charge transport properties of BODIPY-qT*o* and BODIPY-qT*i* polymers in thin-film transistor devices. Initial measurements were performed using a bottom-contact (BC), top-gate device configuration with gold (Au) source-drain electrodes. Polymer films were cast by spin-coating and subsequently annealed at 100 °C before the deposition of the fluorinated ether (Cytop) gate dielectric. Both polymers exhibited *p*-type behaviour but significant differences were observed in their performance. Hence the transfer and output characteristics of BODIPY-qT*i* (Figures 17a,b) exhibited little hysteresis between the forward and reverse sweeps, with a threshold voltage around -15V. The saturated charge carrier mobility was relatively modest, around $5\times10^{-4}\,cm^2V^{-1}s^{-1}$ (Figure 17c).

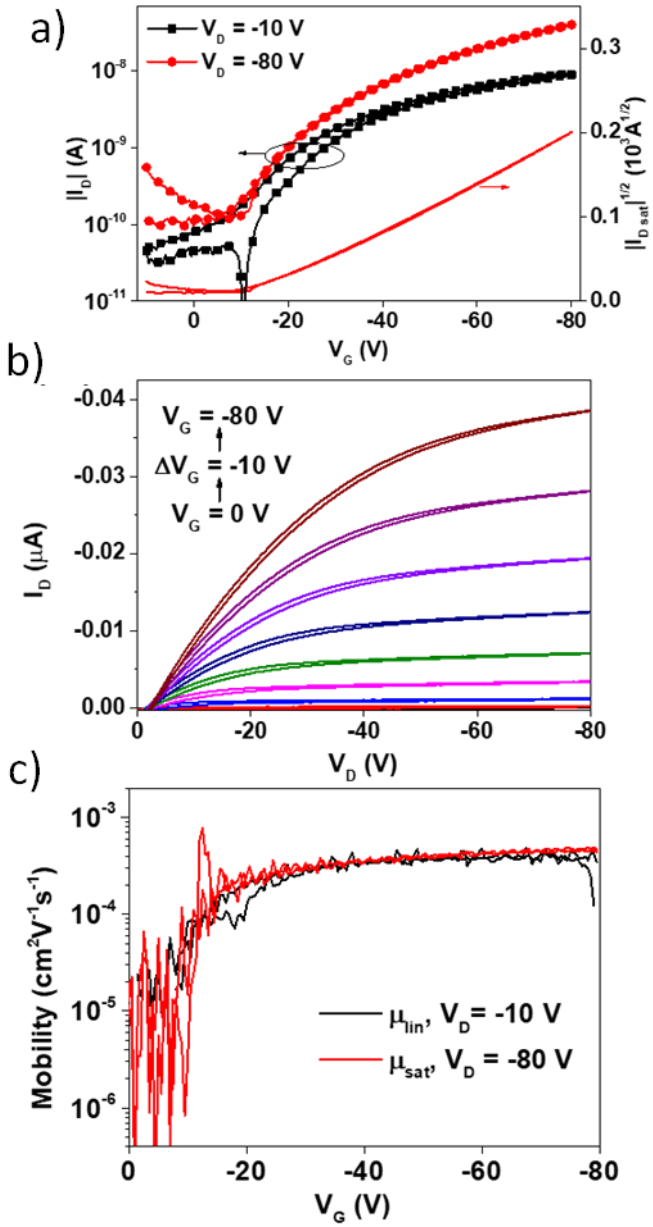

Figure 17. Transfer (a), output (b) characteristics of BC/TG configuration OFET device and mobility calculation based on first derivative of the linear regime transfer curve and first derivative of the square root of the saturation regime transfer curve (c) for the with BODIPY-qT*i*.

In contrast, devices of BODIPY-qT*o* exhibited significant hysteresis between the forward and reverse sweeps, with a much higher threshold voltage of around -50 V (Figure 18). The poor device characteristics made it difficult to extract robust mobility values, although they were approximately one order of magnitude lower than BODIPY-qT*i* .

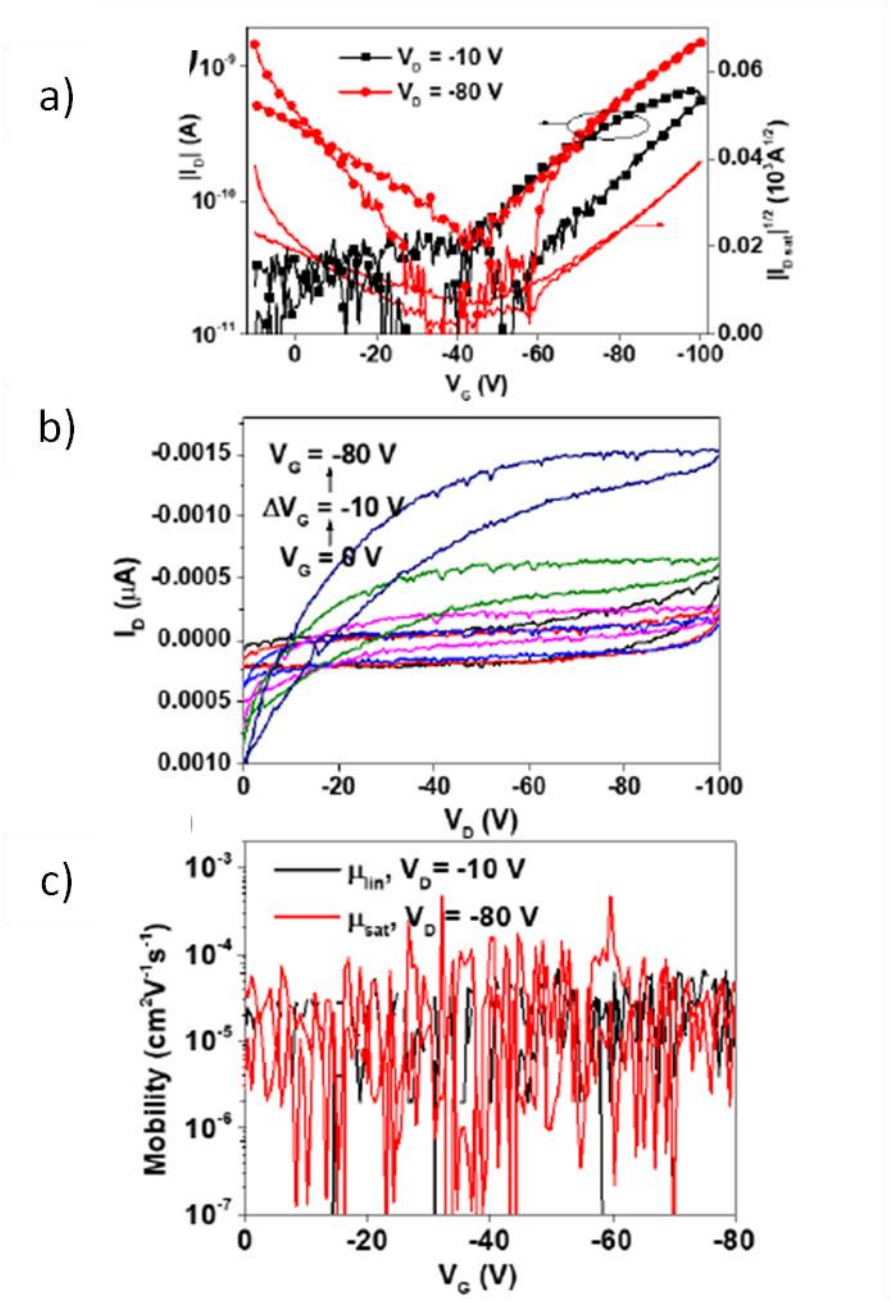

Figure 18. Transfer (a), output (b) characteristics of BC/TG configuration OFET device and mobility calculation based on first derivative of the linear regime transfer curve and first derivative of the square root of the saturation regime transfer curve (c) for the BODIPY-qT*o*.

The reduced performance is likely due to a combination of the HH alkyl chains causing a large torsional twist in the conjugated backbone, inhibiting the close packing of the polymer chains, as well as the resulting increase in the ionisation potential, which increases the injection barrier.

Table 5. Summary of the FET performance of BODIPY-qT*i* and BODIPY-qT*o* polymers.

Polymer	**μ_{sat} average (μ_{sat} max) ($cm^2 V^{-1} s^{-1}$)**	**μ_{lin} average ($cm^2 V^{-1} s^{-1}$)**	**V_{Th} (V)**	**I_{on}/I_{off}**
BODIPY-qT*i*	$4.7\times10^{-4} \pm 3.1\times10^{-5}$ (4.9×10^{-4})	$3.5\times10^{-4} \pm 3.8\times10^{-5}$	-14.4 ± 0.6	10^2-10^3
BODIPY-qT*o*	10^{-5}-10^{-4}	10^{-5}-10^{-4}	< -50 V	10-10^2

Despite the low-lying LUMO of both polymers, no obvious evidence for electron transport was observed in these devices. In order to improve the electron injection, the Au source/drain electrodes were replaced with Al in an otherwise identical device configuration, since the latter has a lower work function that could potentially facilitate electron injection from the metal to the semiconductor due to the reduced barrier. Despite the improvement and the matching electrode/E_{LUMO} interface energetics, no electron accumulation could be observed. Since the nature of the dielectric/semiconductor interface is also known to have a dramatic influence on the electron transport across the channel, top-contact, bottom-gate devices were fabricated using the divinyltetramethyldisiloxane-bis-benzocyclobutene (BCB) as the gate dielectric since the latter is known to provide an excellent interface with various high electron mobility organic semiconductors[112–114]. Control devices using the fullerene derivative [6,6]-phenyl-C_{61}-butyric acid methyl ester ($PC_{61}BM$) as the semiconductor were also prepared in the same device configuration. The latter samples demonstrated the expected transistor performance and in accordance with previously published data. However, we were unable to observe electron transport in either of the polymer devices (Figure 19).

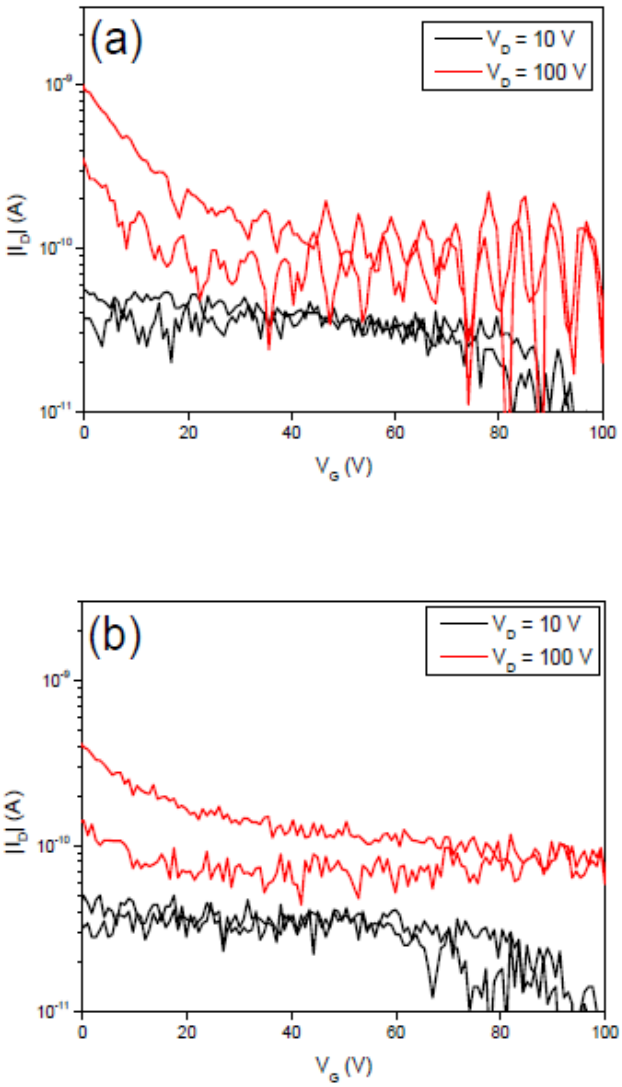

Figure 19. Transfer curves of BG/TC configuration OFET device of (a) BODIPY-qT*i* and (b) BODIPY-qT*o*.

We therefore conclude that despite the low lying E_{LUMO}, neither of the polymers is a good electron transporting material. We believe this may be related to the poor delocalization of the E_{LUMO} along the polymer backbone.

2.2.7 Photovoltaic properties of polymer TBDPTV

Among the synthesized polymers, TBDPTV showed the lowest optical energy gap and upshifted E_{LUMO} level as compared to BODIPY-qT*i* and BODIPY-qT*o* which make it a promising candidate as electron donor

material in bulk heterojunction (BHJ) solar cells. The research groups of Prof. Brabec from FAU University has tested it.

Organic BHJ solar cells were fabricated in inverted device structure consisting of ITO/ZnO/TBDPTV:$PC_{71}BM$/MoOx/Ag, using three different D:A composition ratio (1:2, 1:3 and 1:4). The active layer solution was spin coated under inert atmosphere condition using 97 to 3 vol % of chlorobenzene (CB) and 1,8 diiodooctane (DIO). Figures 20a,b show the J-V curves of the optimized BHJ solar cells under simulated AM 1.5G solar irradiance (100mW cm^{-2}) and in the dark, respectively.

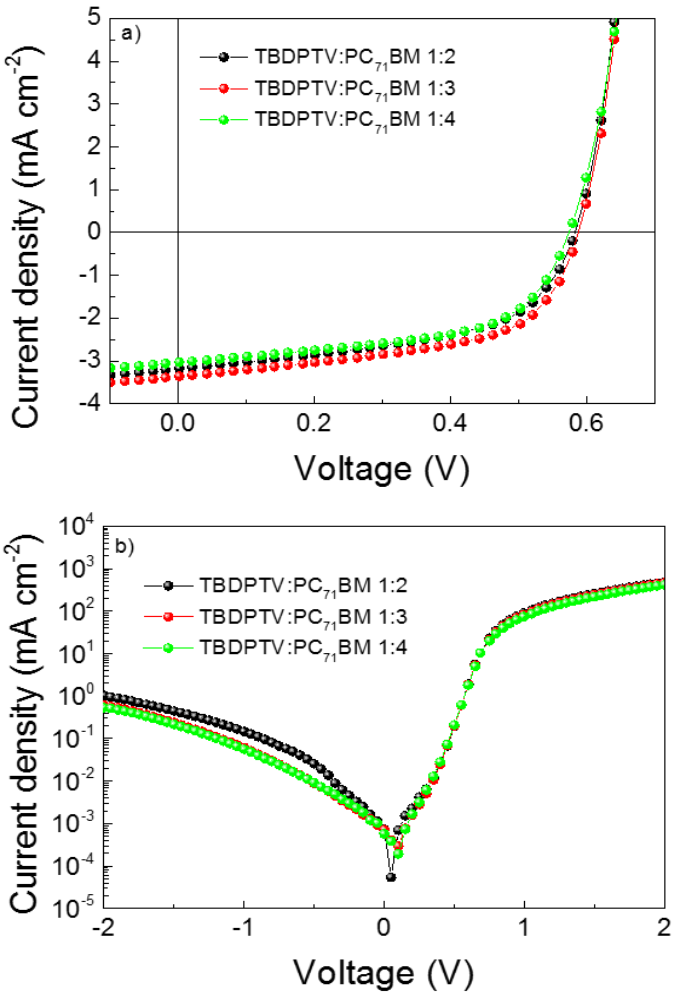

Figure 60. Current density-voltage characteristics under 100 mW cm^{-2} illumination (AM1.5G) (a) in linear graph and (b) in semilogarithmic graph.

The photovoltaic parameters obtained with the three different D:A ratio are summarized in Table 6.

Table 6. Photovoltaic parameters of TBDPTV:$PC_{71}BM$ system in different composition ratio.

TBDPTV:$PC_{71}BM$	V_{oc} (V)	J_{sc}(mAcm^{-2})	FF (%)	η (%)
1:2	0.58 (0.58 ± 0.00)	3.32 (3.27 ± 0.32)	53.45 (51.54 ± 1.82)	1.03 (0.97 ± 0.04)
1:3	0.59 (0.59 ± 0.00)	3.39 (3.16 ± 0.17)	56.18 (55.52 ± 0.58)	1.10 (1.03 ± 0.06)
1:4	0.59 (0.59 ± 0.00)	3.12 (2.86 ± 0.24)	56.51 (56.14 ± 0.37)	1.01 (0.93 ± 0.07)

A PCE of 1.1% was obtained for the 1:3 ratio, with a short circuit current density (J_{sc}) of 3.39 mA cm-^{2}, V_{oc} of 0.59 V and FF of 0.56. Using the same fabrication conditions, solar cells containing 1:2 and 1:4 D:A ratio achieved a maximum efficiency of 1.03 and 1.01, respectively. A strong correlation between the charge carrier mobility and FFs is also obtained for these devices. In fact, as shown in Table 6, solar cells based on 1:3 and 1:4 ratio, display the highest FF of 0.56 and 0.57, respectively. On the other hand, the 1:2 based devices depicted a lower FF of 0.52, consistent with the lower charge carrier mobility obtained.

For all the devices, J_{sc} values are similar and this possibly can be attributed to the not perfect energy alignment with $PC_{71}BM$ for achieving efficient exciton splitting rather than to morphological issues as can be observed by investigations on the surface microstructure carried out through intermitted contact mode atomic force microscopy (AFM, Figure 21). A good intermixing between the donor and the acceptor materials is obtained and the topography and the phase images do not reveal obvious differences

between the three systems studied, supporting the hypothesis that the main limitations on of the system is due a to the low E_{LUMO} offset rather than to morphological issues.

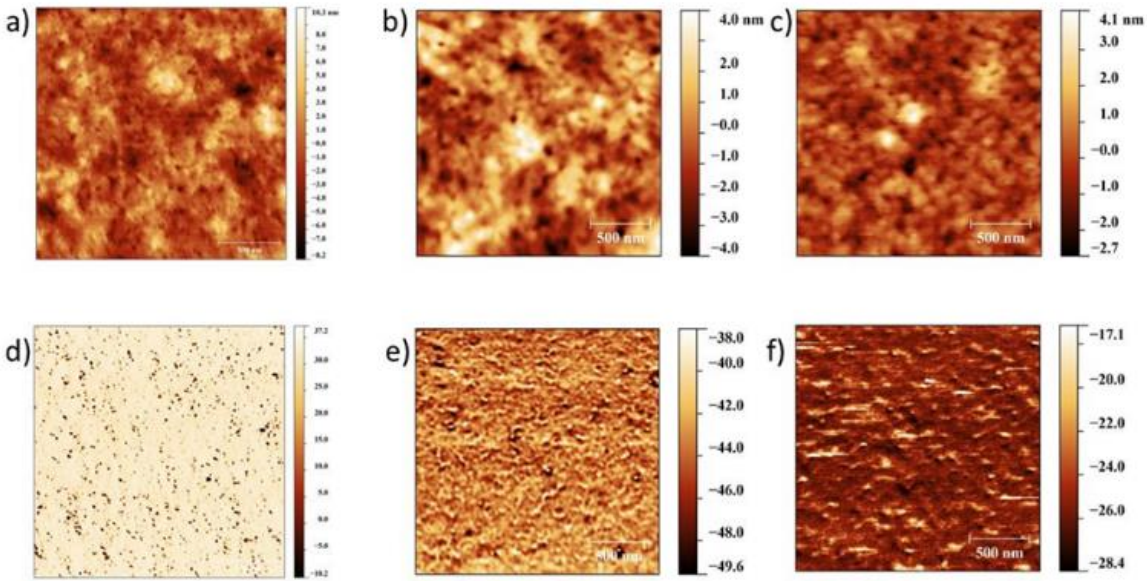

Figure 21. Topography(a,b,c) and phase (d,e,f) images of films TBDPTV:$PC_{71}BM$ 1:2, 1:3 and 1:4 respectively, on top of a layer of ZnO, as measured by intermittent contact mode atomic. Rms=2.29 nm.

External quantum efficiency (EQE) measurements have also been carried out for the best performing solar cell (Figure 22). An EQE signal around 950-1000 nm, even though very weak, is observed, suggesting an existing path towards charge generation from the polymer.

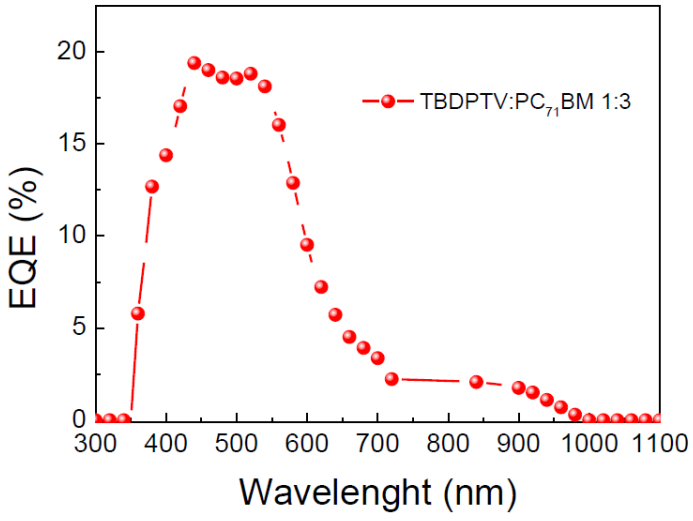

Figure 22. External quantum efficiency (EQE) curve of the TBDPTV:$PC_{71}BM$ (1:3) device.

As reported by Janssen et al.[109], a fast recombination path becomes essential when the E_{LUMO} of the acceptor become too shallow, leading to low J_{sc} values. Noticeably, the rectification behavior of the device slightly improved with increasing the D:A ratio (Figure 22b). The J_{sc} calculated from the EQE is 3.08 mA/cm^{-2}, which is less than 10% smaller compared to the J_{sc} obtained from the solar simulator.

In order to understand the transport properties of TBDPTV based solar cells, the charge carrier mobility μ of the aforementioned devices were determined by employing the technique of photoinduced charge carrier extraction by linearly increasing voltage (photo-CELIV)[110]. Charges are photogenerated by a strongly absorbed laser pulse and extracted after an adjustable delay time. Figure 23 shows the photo-CELIV transients of the TBDPTV:PC71BM system in the three different composition ratios (1:2, 1:3 and 1:4), which were recorded by applying a 2V/20 μs linearly increasing reverse bias pulse and a delay time (td) of 1 μs. From the measured photocurrent transients, the charge carrier mobility (μ) is calculated using the following equation:

$$\mu = \frac{2d^2}{3At_{max}^2\left[1 + 0{,}36\ \frac{\Delta j}{j(0)}\right]}$$

where d is the active layer thickness, A is the voltage rise speed $A = d\mathrm{U}/\mathrm{dt}$, U is the applied voltage, t_{max} is the time corresponding to the maximum of the extraction peak, and j(0) is the displacement current[111].

The photocurrent transients in Figure 23 reveal that t_{max} occurs significantly earlier for the 1:4 weight ratio. As a result, the calculated charge carrier mobility (μ) is higher for the 1:4 ratio $(1.05\pm0.2)\times10^{-5} cm^2V^{-1}s^{-1}$, then for the

1:3 ratio $(9.18\pm0.2)\times10^{-6}$ $cm^2V^{-1}s^{-1}$, and finally for the 1:2 ratio $(7.50\pm0.1)\times10^{-6}$ $cm^2V^{-1}s^{-1}$, respectively.

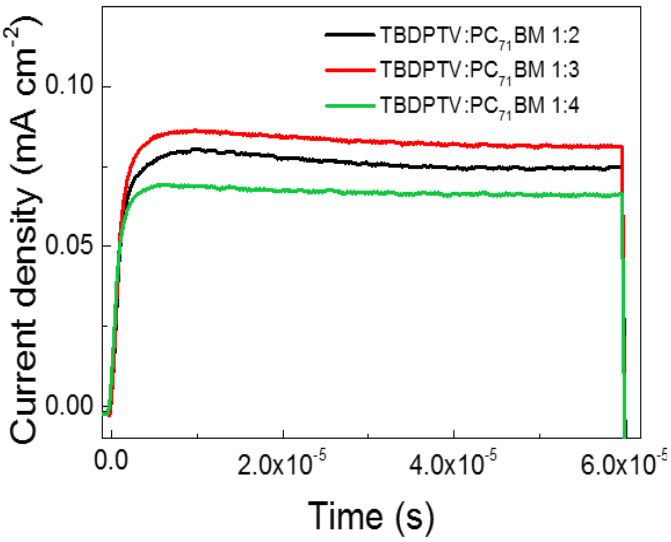

Figure 23. Time-dependent photo-CELIV traces of TBDPTV-based solar cells at a fixed delay time of 1 μs.

Chapter 3

3. BODIPY Small Molecules

3.1. Introduction

Semiconducting organic small molecules have also attracted intense research attention and showed great promise in optoelectronic applications. The advantages of small molecules include well-defined molecular structures, high purity without batch-to batch variations, and the absence of end group contaminants. Moreover, crystalline small molecules exhibit high charge mobility due to their long-range order.

Organic semiconductors emitting in the NIR region are emerging as a promising class of materials with valuable optoelectronic properties. Among the appealing features there are solution processing, low-cost of fabrication, and the possibility of preparation on top of flexible, conformable or even stretchable substrates for organic electronic devices, such as organic (OLEDs) and polymer light-emitting diodes (PLEDs)[115,116]. In general, NIR emitters include organic semiconductors, metal-organic complexes, inorganic nanoparticles and hybrid organic-inorganic perovskite-like compounds[117–120].

Although the quantum yield in this region of the spectrum is significantly lower than for materials emitting in the visible, owing to the so-called "energy-gap law", external quantum efficiencies (EQEs) spanning from ~ 9 % to ~ 24 % and have been achieved in OLEDs incorporating phosphorescent Pt-based porphyrins and carefully-designed derivatives[121–125]. While this is still significantly better than what is achievable with fluorescent NIR materials, the scope and applicability of phosphorescent OLEDs generates significant concerns both because of the use of heavy

metals, and the so-called "efficiency roll-off", limiting the efficiency as the current is increased, and due to a combination of triplet-triplet annihilation, triplet-polaron quenching, and phosphorescent sites saturation (in various ratios also depending on current density).

To achieve near-IR absorbing/emitting abilities, strong donor-acceptor interaction and stabilization of the quinoid resonance structure are required. However, due to the smaller one-dimensional quantum well length, bandgap lowering is more difficult and normally requires very strong donor or acceptor units in the case of small molecules by combining electron donating (D) and electron deficient (A) building blocks with the most common being "D-A-D" dyes[126]. Triphenylamine (TPA), ethylenedioxythiophene (EDOT), pyrrole, thiophene, and bridged bithiophenes derivatives are commonly-used electron-rich units, whereas electron-deficient moieties such as benzobisthiadiazole, thiadiazoloquinoxaline, diketopyrrolopyrrole, thienoisoindigo and cyclopentadithiophenone moieties have been largely employed as acceptor units[127–132]. Interestingly, Yao et al. reported electroluminescence (EL) EQEs > 1% from both D-A-D and A-D-A compounds[133,134]. Such systems benefit from a favorable conformational arrangement of the constituting units, which controls the orbital mixing and leads to the formation of a hybrid localized/charge-transfer (CT) excited state. It was proposed that the localized nature of these states brings about a high radiative rate, whereas the weakly-bound CT nature leads to the formation of a high fraction (> 25 %) of singlet excitons. More generally, however, whereas the properties of dyes of the D-A-D type have been studied extensively, different alternation patterns of the D and A moieties and in particular A-D-A dyes have rarely been explored up to now, mainly because of synthetic difficulties associated to the monofunctionalization of the A building block.

Here, a successful approach to the design and synthesis of a novel A-D-A type NIR dye is described.

3.2 Results and discussion

3.2.1. Synthesis of *α,β*-unsubstituted bromo-BODIPY

As already reported, a facile approach to synthesize *α,β*-unsubstituted BODIPY dyes is the combination of aldehydes and pyrrole under neat conditions. In this work, 5-bromo-thiophene-2-carbaldehyde has been chosen as the aldehyde, and upon condensation with pyrrole, catalyzed by few drops of trifluoroacetic acid, the resulting 2,2'-((5-octylthiophen-2-yl)methylene)bis(1H-pyrrole) (6) is obtained (Scheme 12).

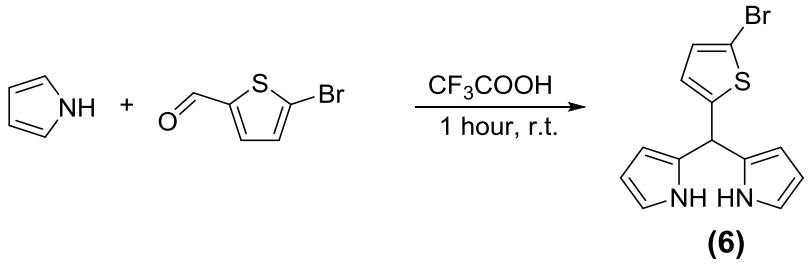

(6)

Scheme 12. Synthesis of 2'-((5-bromothiophen-2-yl)methylene)bis(1H-pyrrole).

Treatment of monomer 6 with the strong oxidant 2,3-dichloro-5,6-dicyano-1,4- benzoquinone (DDQ), then diisopropylethylamine (Hünig's base) and finally with trifluoroborane dietherate [$BF_3O(Et)_2$] provided the corresponding boron dipyrromethene monomer 7 (Scheme 13).

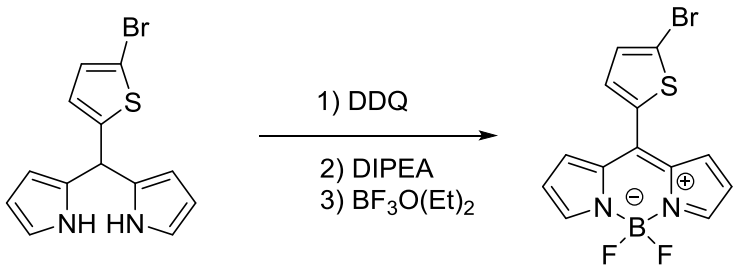

(7)

Scheme 13. Synthesis of 8-bromo BODIPY.

The bromo-thiophene aldehyde derivative has been choosen in order to obtain a functionalized BODIPY that will enable the easy connectivity to the α,ω-oligothiophene cores through their meso-positions. The resulting linear and symmetrical molecular architectures will afford extended π-conjugation throughout the dye as well as optimized molecular energetics. This synthetic methodology can lead to the development of a series of BODIPY based small molecules.

3.2.2. Synthesis of the A-D-A small molecule BODIPY

Small molecule NIRBDTE (NIR-Bodipy dithienyl(ethylene)) was synthesized through Stille cross-coupling using 1:2.5 monomer feed ratios (Scheme 14). A solution of dibromo borondipyrromethene monomer 7 and the commercially available distannyl-1,2-di(2-thienyl)ethylene (DTE), was combined in dry deoxygenated toluene in the presence of tetrakis(triphenylphosphine)palladium and the mixture was heated to reflux overnight. The crude product was purified through silica-gel column chromatography to afford the pure compound and then recrystallized.

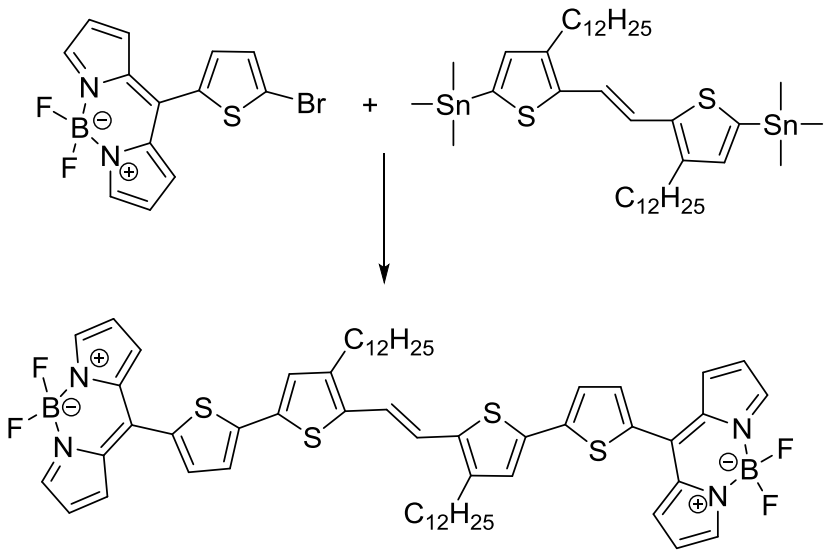

Scheme 14. Synthesis of NIRBDTE.

3.2.3. Electrochemical and Theoretical Characterization

To estimate the energy levels and the electrochemical bandgap (E_g^{CV}) by identifying the oxidation and reduction potentials of the NIRBDTE, cyclic voltammetry (CV) has been performed (Figure 24).

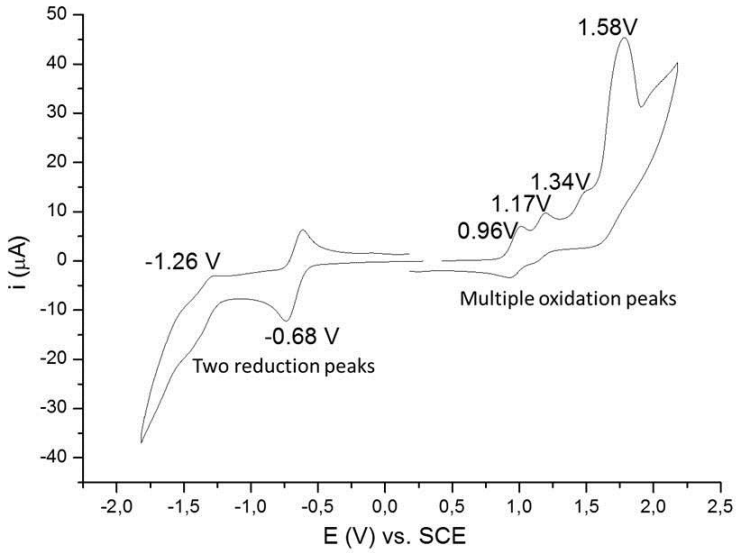

Figure 24. Cyclic voltammetry analyses of NIRBDTE.

NIRBDTE shows two reversible reduction peaks and four reversible oxidation peaks. The reversible oxidation and reduction peaks are calculated by $[(E_{p,c}+E_{p,a})/2]$ where $E_{p,c}$ and $E_{p,a}$ are the cathodic and anodic peak potentials, respectively. The reduction peaks at -0.68 V and -1.26 V versus saturated calomel electrode (SCE) are attributed to E_{LUMO} (-4.02 eV) and E_{LUMO+1} (-3.44 eV), respectively (Figure 24). In addition, the oxidation peaks at 0.96 V, 1.17 V, 1.34 V and 1.58 V versus SCE are attributed to E_{HOMO} (-5.66 eV), E_{HOMO-1} (-5.87 eV), E_{HOMO-2} (-6.04 eV) and E_{HOMO-3} (-6.28 eV), respectively (Figure 24). By comparing the Figure 24 with typical voltammograms of BODIPY[135,136], we can safely assign the reduction peaks at -0.68V and the oxidation peak at 1.58 V to the BODIPY units of the NIRBDTE, hence the reduction peak at -1.26 V and the oxidation peaks at 0.96 V, 1.17 V and 1.34 V can be assigned to the oligothiophene central

segment. To confirm the obtained results, atmospheric pressure photoelectron spectroscopy was performed (Figure 25) and the detected ionization potential (IP) at -5.48 eV was in agreement with the CV one.

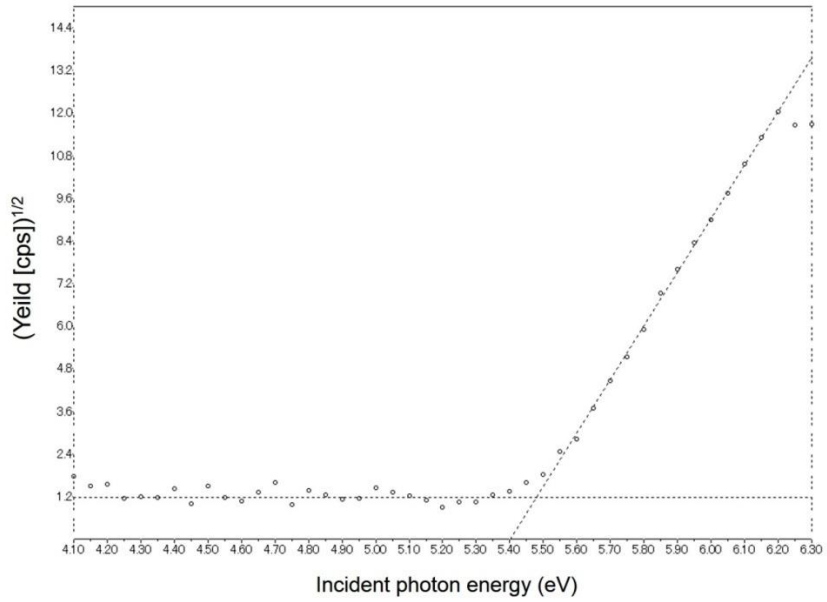

Figure 25. Ionization potential of NIRBDTE estimated by atmospheric pressure photoelectron spectroscopy (AC-2).

We compared these results with DFT calculations in order to investigate the relative positions and spatial distribution of the frontier energy levels (E_{HOMO} and E_{LUMO}) that are eventually responsible for the electronic properties of NIRBDTE. DFT calculations were carried out with the ground state geometry optimized at the B3LYP/6-31 G(d,p).

In Figure 26 the energy levels of NIRBDTE and polymer F8BT, which was used as the host material in the fabrication of OLEDs (Figure 26a), and the band diagram of the energy levels of F8BT and NIRBDTE (Figure 26b) are illustrated schematically. The effective E_{HOMO} and E_{LUMO} of NIRBDTE are those indicated in blue, but we also illustrate in red the local electronic structure of the BODIPY moieties (Figure 26b).

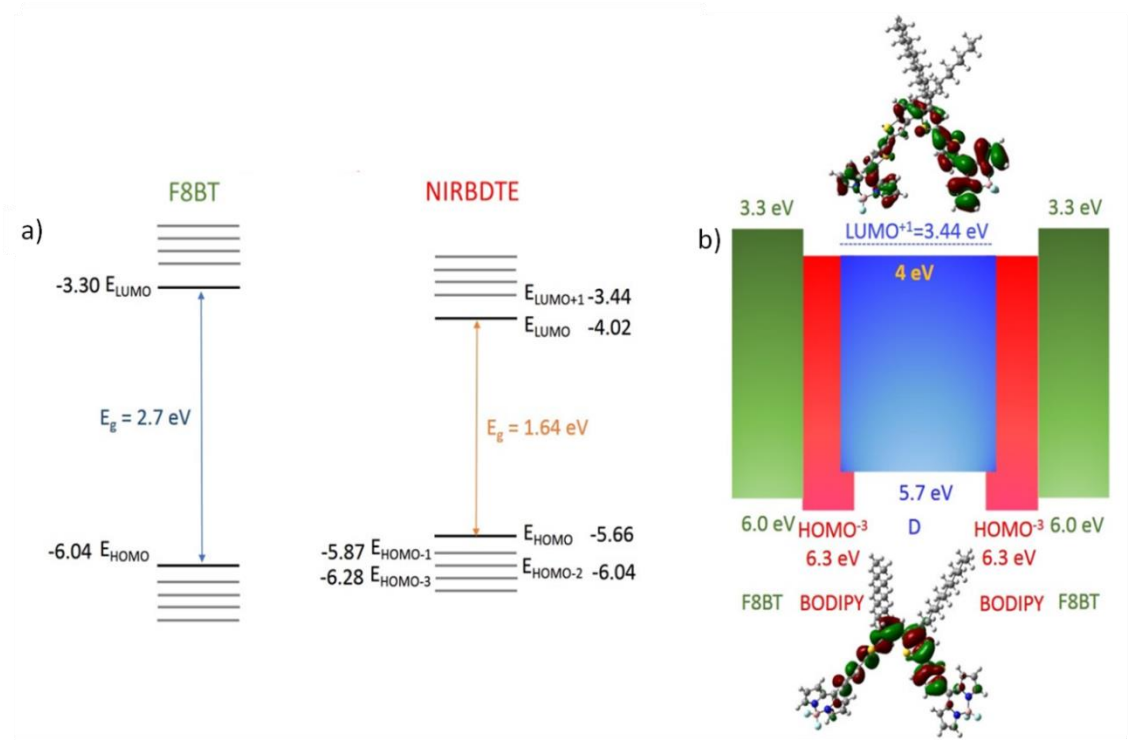

Figure 26. a) Energy levels of F8BT and NIRBDTE and b) the related band diagram of the emitting blend F8BT:NIRBDTE as active layer.

As can be noticed from the distributions of the frontier molecular orbitals in the ground state (Figure 26b) the E_{LUMO} charge density is well distributed along the entire molecule and does not localize at the two BODIPY acceptor units, as it might have been expected in view of the electron-withdrawing nature of the units. On the contrary, charge distribution within the E_{HOMO} is localized on the thiophenes of the central segment. The computed E_{HOMO} and E_{LUMO} levels are found at -5.56 eV and -3.06 eV (where the minus sign indicates that the levels are relative to the vacuum energy), respectively, in excellent agreement with atmospheric pressure photoelectron spectroscopy and cyclic voltammetry .

Consistently with the DFT results discussed above, the E_{LUMO} is set by the BODIPYs, and extends over the full NIRBDTE. This is not the case for the E_{HOMO}, whose dominant feature is instead the negligible charge distribution over the BODIPYs. Whereas the NIRBDTE E_{HOMO} is thus set by that of the

bithienyl at ~ -5.7 eV below vacuum, the relevant local energy levels on the BODIPY moieties remain those of the parent molecule at ~ -6.3 eV.

Furthermore, from the DFT calculations we note that introduction of the didodecyl side chain, which are aligned opposite in order to minimize the steric hindrance, close to the ethylene bond, leads to a "pseudo" 2D conformation of the NIRBDTE, with segments of the latter lying both in-plane and out-of-plane due to cis-geometric isomerism of the ethylene bond. The dihedral angles between the two carbon atoms of the ethylene bond along with the connected carbon and sulphur atoms of the two neighboring thiophene rings are 124.2°and 8.5°, respectively (Figure 27). In both in-plane and out-of-plane directions the inter-ring torsional angles are between 9 and 13° which ensures an efficient π-orbital delocalization along the donor part (Figure 27). On the other hand, inter-ring torsional angles of 43.7° were calculated between the boron-dipyrromethene and the meso-thiophene units. This angle is smaller as compared to those of previously reported meso-aromatic substituted BODIPY small molecules, which is probably due to the lack of α,β-pyrrole substituents and sterically less-encumbered nature of the five-membered thiophene ring[137]. Thus, our structural approach should offer a significant advantage to enhance charge-transport in the solid state when compared to the previously reported BODIPY-based semiconductors[138]. Comparable donor-acceptor dihedral angles were reported between thiophene and naphthalenediimide (NDI)/perylenediimide (PDI) units in several high-performance n-channel semiconductors[139–141].

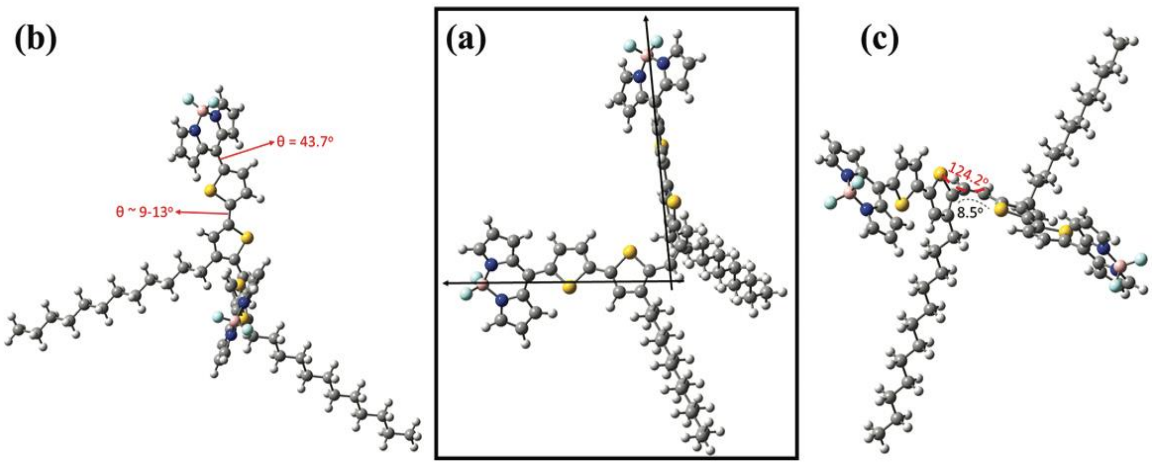

Figure 27. Optimized molecular geometries of NIRBDTE showing inter-ring torsional angles (θ) (DFT, B3LYP/6-31G(d,p).

3.2.4 Optical Characterization

The normalized UV–vis absorption spectra and PL emission spectra are reported in Figure 28.

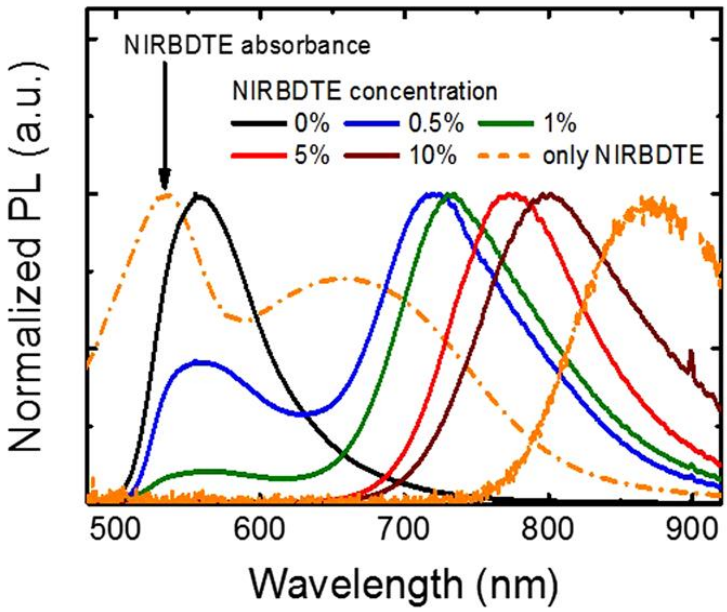

Figure 28. Absorption and PL spectra (excited at 450 nm) of the solid films incorporating different NIRBDTE concentration in the host F8BT and NIRBDTE film absorption spectrum.

In order to study the behaviour of the molecule in host-guest active layer, the photoluminescence spectra of F8BT:NIRBDTE film at different guest

concentration (Figure 28) have been recorded. As can be noticed from the spectra, the emission from F8BT is quenched in the presence of NIRBDTE due to efficient energy transfer, consistently with the good spectral overlap between the F8BT PL (Figure 28) and the absorbance of NIRBDTE. Furthermore, as NIRBDTE concentrations increase, the NIR emission component gains intensity with respect to the F8BT residual band, and progressively red-shifts (from 720 nm to 800 nm).

The PL decay time via time-correlated single-photon counting has been also measured as showed in Figure 29, at 720 nm. For all the blends, the decay is single exponential which confirms the dominant singlet nature of the radiative exciton and varies from 1.2 ns (for just the molecule) to 0.6 ns for the blend with 10% oligomer concentration.

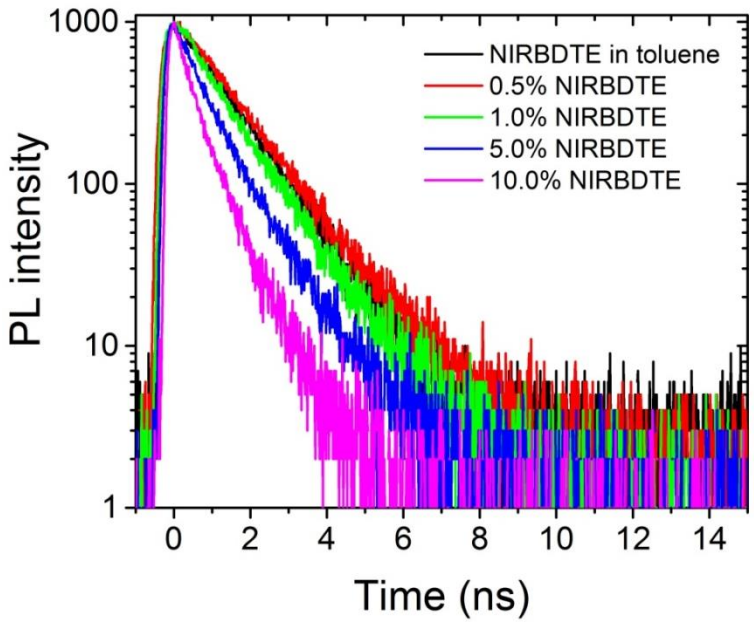

Figure 29. PL decay measured at 720 nm for the F8BT/oligomer blends and oligomer in toluene solution.

3.2.5 Electroluminescent properties of NIRBDTE

The research group of Prof. Cacialli from UCL has studied the emission of NIRBDTE at different concentrations 0.5%, 1%, 5% and 10% wt) in blends with F8BT, in conventional solution-processed PLEDs with

ITO/PEDOT:PSS anodes and Ca/Al cathodes to investigate the influence of the NIR oligomer on the device operation. In Figure 30, it is reported the current density-voltage-radiance (J-V-R) characteristics and the external quantum efficiency.

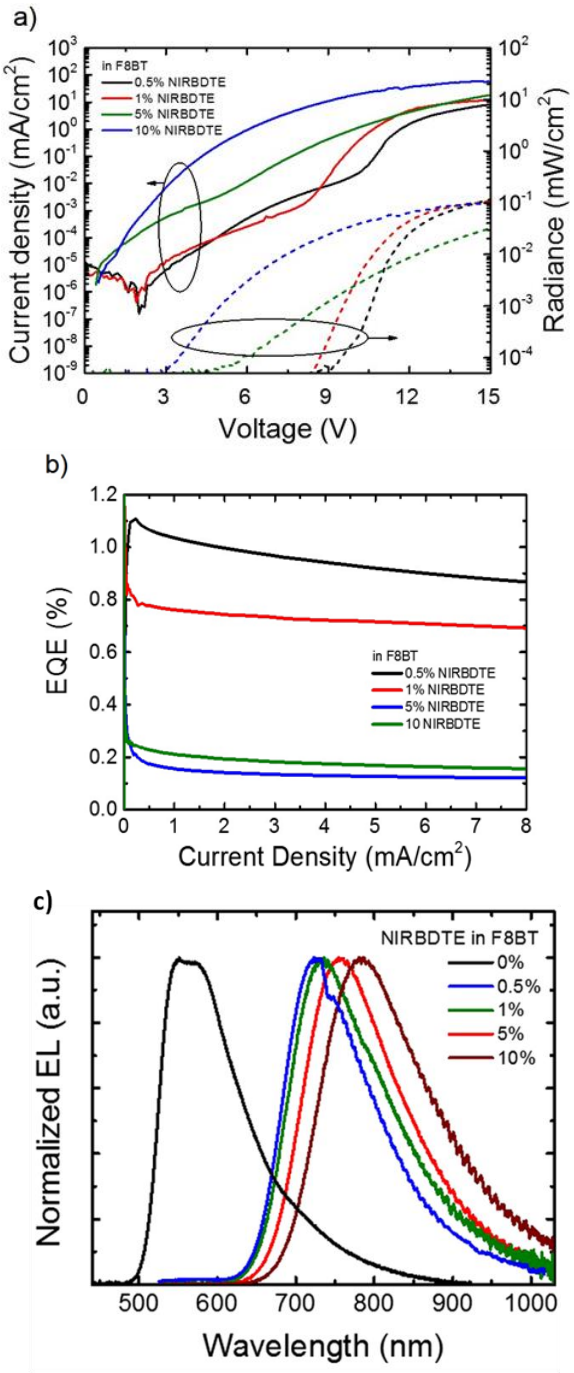

Figure 30. a) J-V-R curves and (b) EQE of PLED incorporating the blend of F8BT with the NIRBDTE at different concentration. (c) EL spectra of PLEDs incorporating these films as emissive layers.

From Figure 30, it is shown that the best EQE was obtained with a blend incorporating 0.5% wt of NIRBDTE. This OLED exhibits a EQE up to 1.1% with a turn-on voltage (V_{ON}) of 9.43 ± 0.05 V and an EL emission (~65% in NIR region) of ~0.11 mW/cm^2 peaked at 720 nm.

The ~1.1% EQE in the solid state was measured at 0.22 mA/cm^2 with a driving voltage of 11 V and represents the state-of-the-art for fluorescent "metal-free" emitting materials, in which only singlets fluorescence can be harvested, such that the maximum achievable internal quantum efficiency is limited to 1/4 of the PL efficiency (Φ_{PL}), consistently with simple spin-statistics arguments.

To put this number in an appropriate context, the theoretical maximum EQE that can be obtained from devices of this kind, has been calculated by taking into account the measured PL efficiency of active layers, i.e. Φ_{PL} = 20 ± 2% (F8BT incorporating 0.5% wt NIRBDTE, measured on spectrosil substrates) and by considering the surface out coupling efficiency ξ[43,44]. The latter can be estimated for example by using the published values of the active layer's refractive index (~1.75 for F8BT above 700 nm, having disregarded the perturbation of NIRBDTE in this case, given the slight concentration), so that we can further calculate ξ to vary from 0.16 to 0.24, respectively, in the case of isotropic or in-plane dipoles. In the ideal case of unit charge injection efficiency (γ) ~1, the "ideal" EQE is expected to vary from ~0.56% to 1.47% (also taking into account the propagation of the error on Φ_{PL} measurements) thereby confirming the excellent quality of the devices, and the limited margins for improvements in terms of device architecture. In fact, further improvements can be envisaged by improving ΦP_L, or by moving to a phosphorescent material.

The PL efficiency decreases by increasing the NIRBDTE content in F8BT from 19% (at 1% wt) to 5% (at 10% wt). This reduction is entirely expected as a result of both the reduction of the energy gap, and because of the aggregation-induced quenching of the oligomer blended with F8BT the radiative exciton. Also, EL spectra also exhibit a red-shift of the NIRBDTE emission with concentration, however and contrary to what is observed in the PL spectra, there is no residual F8BT contribution at 0.5% wt and 1% wt. This effect has been attributed to preferential formation of excited species directly onto the guest chromophores, which are also expected to mediate transport (energy selective in its nature, and occurring preferentially through low-energy sites).

Figure 31 depicts the OLEDs key parameters (EQE, V_{ON} and radiance) as a function of the NIRBDTE loading. As already mentioned, the devices with 0.5% loading feature the maximum EQE (1.1%), and this gradually decreases with increasing loading (on average from ~0.9% for the 0.5% NIRBDTE concentration, to ~0.2% at 1% guest by weight). At the same time however, the 0.5% devices also feature the highest turn-on voltage (-9.45 ± 0.05 V on average). This is significantly higher than for F8BT (~2.5 V) and it can be attributed to charge trapping by the dye in the emissive layer. The progressive decrease of the turn-on voltage with NIRBDTE concentration, taken together with the PL efficiency reduction, and red-shift of the luminescence, strongly supports the interpretation that NIRBDTE molecules are well-dispersed in the host matrix for the 0.5% devices, but increasingly less so as the loading is increased. The radiance from the different devices is compared in Figure 31c, and ranges from ~0.11 mW/cm^2 (at ~52 mA/cm^2 for 10% wt NIRBDTE) to ~0.24 mW/cm^2 (at ~23 mA/cm^2 for 1% wt NIRBDTE). Interestingly we find that the emitted radiance is maximised in the 1% NIRBDTE devices (0.19 mW/cm^2), as a

result of the interplay between efficiency and driving conditions, which allows easier charge injection and transport compared to the more efficient 0.5% devices.

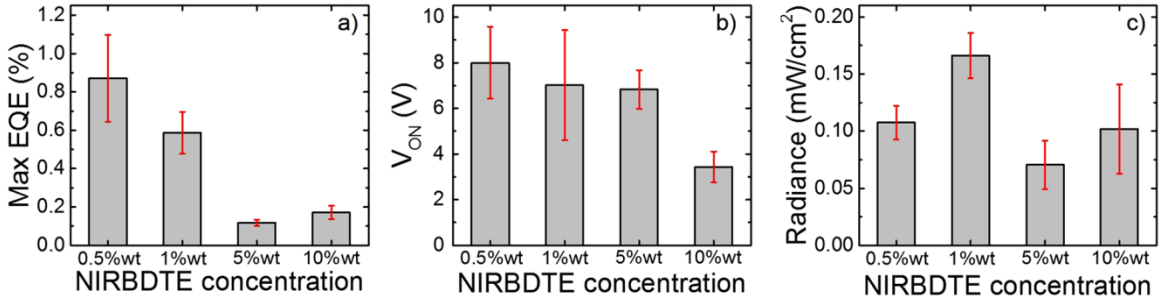

Figure 31. Mean and the related standard deviation (in red) of (a) the maximum external quantum efficiency (EQEs), (b) the turn-on voltage (V_{ON}) and (c) the radiance of PLEDs incorporating different concentration of NIRBDTE (0.5%, 1%, 5% and 10%wt) in blend with F8BT as host material for a set of 8 devices.

Chapter 4

Outlook

BODIPY-based conjugated polymers and small molecules represent an enormous scientific area for molecular and supramolecular design through their facile synthesis and chemical structure modification.

The recent progress in the synthesis of BODIPY based materials by conventional metal catalyzed cross coupling rather than oxidative coupling opens the way to provide polymer backbones with structural integrity and minimization of chemical defects. Moreover, as the access to less substituted and more stable BODIPY cores has been achieved recently, new polymer and small molecule structures can be achieved with improved ordering, increased π-π stacking and superior optoelectronic properties as the result of the possible enhancement of the planarity of the backbone, through the minimization of the steric hindrance.

During this PhD thesis functional *α,β*-unsubstituted BODIPY building blocks suitable for conventional catalyzed cross coupling reaction and polymerization have been synthesized. In order to confirm the proof of concept, the dibromo BODIPY has been successfully polymerized through Stille cross coupling with (E)-1,2- bis(3-dodecyl-5-(trimethylstannyl)thiophen-2-yl)ethene as the comonomer providing a new ultra LBG (E_g^{opt} = 1.15 eV) TBDPTV copolymer. To the best of our knowledge TBDPTV has been the first *α,β*-unsubstituted BODIPY-based NIR copolymer synthesized by conventional catalyzed cross coupling polymerization methods. TBDPTV exhibits a panchromatic absorption spectrum ranging from 300 nm to 1100 nm, and a promising PCE of 1.1% in NIR BHJ OPVs using $PC_{71}BM$ as the electron acceptor with very interesting photovoltaic characteristics, such as good fill factor (FF) and open circuit voltage (V_{oc}).

Then the thesis continued with the synthesis of ultra low bandgap (E_g^{opt} =1 eV) π-conjugated D-A polymers consisting of *α,β*-unsubstituted meso-positioning thienyl BODIPY as the electron deficient unit with readily available (3,3'-didodecyl-2,2'-bithiophene-5,5'-diyl)bis(trimethylstannane) or (4,4'-didodecyl-2,2'-bithiophene-5,5'-diyl)bis(trimethylstannane) or (*E*)-1,2-bis(3-dodecyl-5-(trimethylstannyl)thiophen-2-yl)ethene to provide the polymers BODIPY-qT*o*, BODIPY-qT*i* and CB06, respectively by palladium catalyzed Stille aromatic cross coupling polymerization conditions. With these polymers we have demonstrated that the TT positioning of the alkyl side chains at the two central thiophenes of the quaterthiophene segment results in superior FET performance compared to the HH positioning due to the less steric hindrance of the polymer backbone. Moreover, the lower torsional twist in the conjugated backbone of BODIPY-qT*i* leads to lower E_g^{opt} and upshifted energy levels versus vacuum as compared to BODIPY-qT*o*.

After exploring BODIPY moieties in NIR absorber polymers, next target was the synthesis of NIR emitter small molecule. A red/NIR emitting A-D-A-type dye based on *α,β*-unsubstituted BODIPY moieties as A units embedded in a wider gap F8BT as emissive layer for OLEDs has been synthesized. The emitting devices incorporating the BODIPY NIR emitter at a relatively low concentration of 0.5% wt exhibit maximum EQEs up to 1.1%, with an EL emission peaked at 720 nm (~65% in the “conventional” NIR region, i.e. $\lambda > 700$ nm). In terms of maximum efficiency these results represented the current state of the art for NIR emitters not taking advantage of heavy/toxic metals to induce phosphorescence, as emission efficiency is expected to decrease with decreasing gaps according to the so called energy-gap law.

The recent findings in the BODIPY fields can guide synthetic chemists and materials scientists towards the optimization of next generation BODIPY-

based semiconductors with predetermined optoelectronic properties for specific optoelectronic applications.

Chapter 5

5. Experimental Data

5.1. Instrument

Nuclear Magnetic Resonance (NMR): 1H and 13C NMR spectra were recorded on a Bruker AV-400 (400 MHz for 1H and 100 MHz for 13C), using the residual solvent resonance of $CDCl_3$ as an internal reference.

Gel Permeation Chromatography (GPC): For TBDPTV and CB06: M_n and M_w of the polymer have been determined by GPC on a PSS/Agilent SECurity GPC system, equipped with two PSS SDV analytical linear M columns, ALSG1329A DAD detector, and RID G1362A RI detector. The measurement was performed with chloroform as eluent, with a sample concentration of 0.8 g/L.

For BODIPY-qT*i* and BODIPY-qT*o*: Average molecular weights per number ($\overline{M_n}$) and dispersity ($Đ$) were determined with Gel Permeation Chromatography (GPC) at 150 °C on a high temperature PL-GPC 220 system using a PL-GEL 10 μm guard column, two PL-GEL 10 μm Mixed-B columns and ortho-dichlorobenzene (*o*-DCB) as the eluent. The instrument was calibrated with narrow polystyrene standards with M_p ranging from 4830 g/mol to 3242000 g/mol.

Absorption spectroscopy: UV/vis spectra were measured on a Jasco V-670 spectrophotometer.

Cyclic Voltammetry: Cyclic voltammetry was executed in chloroform with 0.1 M $(n\text{-}Bu)_4NClO_4$ against standard calomel electrode. HOMO and LUMO levels were calculated using the formulae HOMO=-(E_{ox}+4.7) eV and LUMO=-(E_{red}+4.7) eV, respectively. The potensiostat was a PAR VersaSTAT4 and the working electrode used was platinum.

Atmospheric pressure photoelectron spectroscopy: AAPPS has been performed on a Riken Keiki AC-2 spectrometer in thin film at room temperature.

J-V measurements: The J-V characteristics was measured using a source measurement unit from BoTest. Illumination was provided by a solar simulator (Oriel Sol 1A, from Newport) with AM1.5G spectrum at 100 mW/cm^2. EQEs were measured using an integrated system from Enlitech, Taiwan. In order to study the light intensity dependence of current density, we used a series of neutral color density filters. The intensity of light transmitted through the filter was independently measured via a power meter.

Photo-CELIV: In photo-CELIV measurements, the devices were illuminated with a 405 nm laser-diode. Current transients were recorded across an internal 50 Ω resistor of an oscilloscope (Agilent Technologies DSO-X 2024A). We used a fast electrical switch to isolate the cell and prevent charge extraction or sweep out during the laser pulse and the delay time.

Fabrication of Photovoltaic devices: All devices were fabricated using doctor-blading under ambient conditions. Pre structured indium tin oxide (ITO) substrates were cleaned with acetone and isopropyl alcohol in an ultrasonic bath for 10 minutes each. After drying, the substrates were successively coated with 40 nm of zinc oxide (ZnO), 10 nm of $Ba(OH)_2$ and finally a 80-90 nm thick active layer based on TBDPTV:$PC_{71}BM$ (20 g L^{-1}). To complete the fabrication of the devices 10 nm of MoOx and 100 nm of Ag were thermally evaporated through a mask (with a 10.4 mm^2 active area opening) under a vacuum of ~$5 \cdot 10^{-6}$ mbar.

Fabrication of OLED devices: Polymer F8BT (Mw ≈ 255919 g/mol) was purchased from OSSILA.

The film of F8BT/NIRBDTE (~90 nm thick) were deposited onto clean Spectrosil substrates via spin-coating for the UV-Vis spectrum detection.

ITO -coated glasses (Colorado Concept Coatings LLC, ~20 Ω/square) were cleaned in an ultrasonic bath with acetone and isopropyl alcohol (10 min each step) and treated with an oxygen plasma (15 min at 10.2 W)46–48. After drying, the substrates were successively coated with 50 nm of PEDOT:PSS (purchased from Sigma-Aldrich), spin coated on top of the ITO-coated glass substrates in air and thermally treated inside a N_2 glove-box. F8BT and NIRBDTE were dissolved in toluene (10 mg/ml) and pristine F8BT and different concentrations (0.5%, 1%, 5% and 10% wt) of NIRBDTE in blend with F8BT were spin coated as emissive layers on top of the anode to obtain ~90 nm thick films. To complete the fabrication of the devices 30 nm of Ca cathode and 150 nm of Al protective layer were thermally evaporated under a vacuum of $\sim 1 \cdot 10^{-6}$ mbar.

Emission spectroscopy: PL spectra of F8BT, 1, 5 and 10% wt blends and NIRBDTE thin films on spectrosil substrates were measured at room temperature with excitation from a 450 nm laser diode module (average power <1 mW, collimated beam) and collected with an ANDOR-Shamrock 163 spectrometer coupled with an ANDOR-Newton charge-coupled device (CCD) unit. The PL efficiency of the thin films was measured by means of an integrating sphere. The samples were excited with the same low-power 450 nm laser diode module mentioned above. Time-resolved PL measurements were carried out with a time-correlated single photon counting (TCSPC).

Morphology: The AFM images have been acquired with a Bruker Dimension Icon AFM.

Theoretical Calculations: All calculations of the model compounds studied in this work have been performed using the Gaussian 03 software package.The alkyl side chain substituents anchored onto the DPP and the

peripheral thienyl rings have been replaced with methyl groups in the model compounds for our calculations. While the presence of these long alkyl chains enhances the solubility of these polymers and affects the charge carrier mobility and photovoltaic behavior of the polymer,[S5-S7] from a computational point of view their replacement with shorter chains does not affect their optoelectronic properties (HOMO, LUMO and band gap) and thus the optimized structures of the molecules.[S8,S9] The ground-state geometry of each model compound has been determined by a full geometry optimization of its structural parameters using the DFT calculations, upon energy minimization of all possible isomers. In this work, the DFT calculations were performed using the Becke's three-parameter hybrid functional, B3, with non-local correlation of Lee-Yang-Parr, LYP, abbreviated as B3LYP in conjunction with the 6-311G(d,p) split valence polarized basis set. All calculations were performed taking into account that the system is under vacuum conditions. No symmetry constraints were imposed during the optimization process. The geometry optimizations have been performed with a tight threshold that corresponds to root mean square (rms) residual forces smaller than 10^{-5} au for the optimal geometry. The visualization of the molecular orbitals has been performed using GaussView 5.0.

OFET device fabrication procedures: *Hole mobility measurements*: Bottom contact/top gate (BC/TG) devices were fabricated on glass substrates using Au (40 nm) source-drain electrodes and CYTOP dielectric. Au electrodes were treated with pentafluorobenzene thiol (PFBT) SAM to increase the work function. Polymers were dissolved in chloroform at a concentration of 10 mg/mL, and spin cast at 2000 rpm onto the substrate for 60 s. The obtained polymer films were thermally annealed at 100 ^{o}C for 30 min, before spin coating of CYTOP dielectric (900 nm). The devices were completed by evaporation of Al (40 nm) gate through shadow masks. The

channel width and length of the transistors are 1000 µm and 50 µm, respectively. A Keithley 4200 parameter analyzer was used to characterise the transistors under nitrogen. Linear mobility was calculated according to the equation below: $\mu_{lin} = \frac{L}{WC_iV_D}\left(\frac{\partial I_{D\,lin}}{\partial V_G}\right)$

And saturation mobility was extracted from the slope of $I_D^{1/2}$ vs. V_G:

$\mu_{sat} = \frac{2L}{WC_i}\left(\frac{\partial\sqrt{I_{D\,sat}}}{\partial V_G}\right)^2$

Performance parameters were averaged over ~6 devices.

Electron mobility measurements: Bottom gate/top contact devices were fabricated on heavily doped n^+-Si (100) wafers with 400 nm-thick thermally grown SiO_2. The Si/SiO_2 substrates were treated with BCB to improve electron transport. Polymers were dissolved in chloroform at a concentration of 10 mg/mL, and spun cast at 2000 rpm onto the substrate for 60 s. The obtained polymer films were thermally annealed at 100 ^oC for 30 min. Al (40nm) source and drain electrodes were deposited onto the polymer film under vacuum through shadow masks. The channel width and length of the transistors are 1000 µm and 40 µm, respectively.

5.2 Synthesis

5.2.1. 2,2'-((5-octylthiophen-2-yl)methylene)bis(1H-pyrrole) (1)

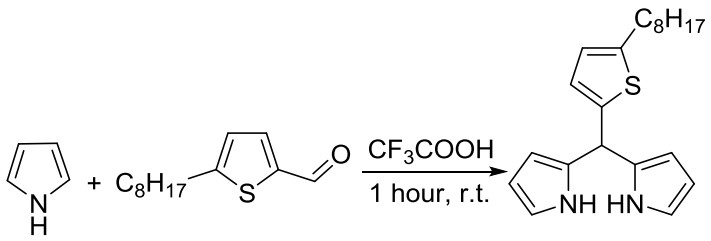

(1)

Procedure

A solution of pyrrole (400 mmol, 28 ml) and 5-octyl-thiophen-2-carbaldehyde (10 mmol, 2,24 gr) was degassed by bubbling with argon for 30 min, then trifluoroacetic acid (CF_3COOH, 0,1 ml) was added. The solution was stirred for 1 hour at room temperature. A TLC control was made and it showed the starting aldehyde, so the solution was stirred at room temperature for another hour. The TLC control made showed the starting aldehyde so some drops of acid were added and the solution was stirred for another hour.
The mixture was diluted with 350 mL of dichloromethane (CH_2Cl_2), then washed with 0.1 NaOH aq., and water and the organic phase was dried with magnesium sulphate ($MgSO_4$).
The solvent was removed under reduced pressure. Attempt to remove the excess of pyrrole by vacuum distillation at room temperature was unsuccessful.
The product was purified by chromatography on silica gel using as eluents at the beginning only hexane and then increasing the polarity to 9:1 hexane/ethyl acetate.
The solvent from the collected fraction was removed under reduced pressure and it was dried overnight in high vacuum at 25°C.
The crude product (2,40 gr, 71% yield) is a yellow-green oil.

^{1}H-NMR (crude): ($CDCl_3$, 400 MHz): δ 8.0 (s, 2H), 6.70 (dd, ^{3}J = 6.70 Hz, 2H), 6.60 (d, 1H), 6.17 (dd, 3J = 6.17 Hz, 2H), 6.04 (s, 2H), 5.66 (s, 1H), 2.73 (t, 2H), 1.63 (m, 2H), 1.29 (m, 10H), 0.89 (t, 3H).

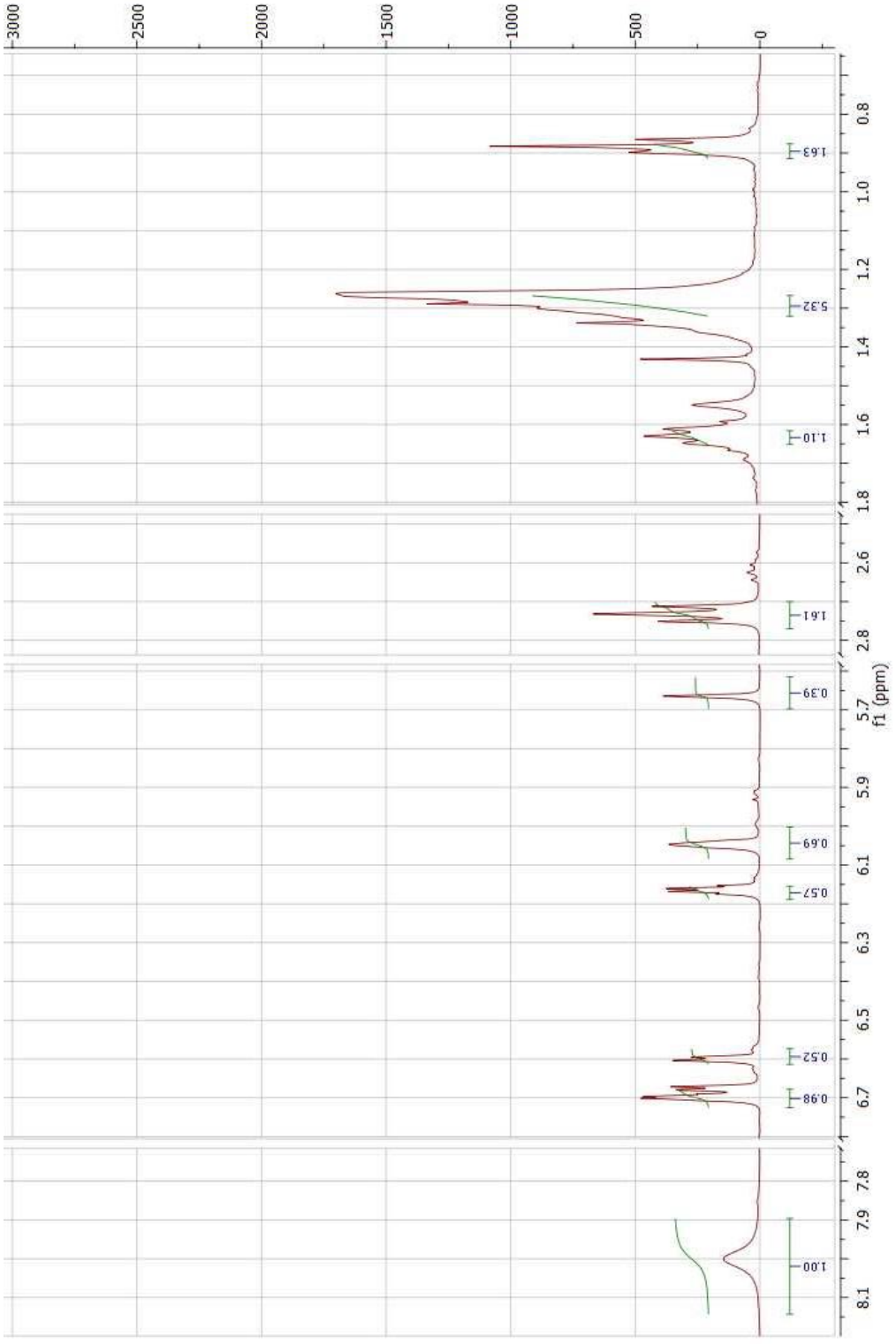

Figure 32. ^{1}H-NMR of 2,2'-((5-octylthiophen-2-yl)methylene)bis(1H-pyrrole).

5.2.2 8-octylthiophene BODIPY (2)

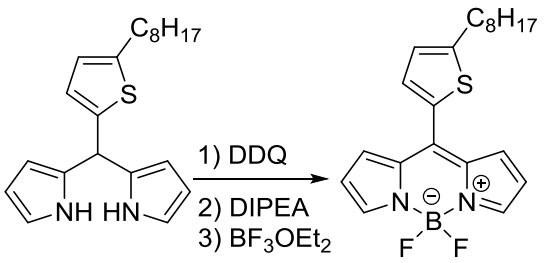

(2)

Procedure

Monomer 1 (2,30 gr, 6.8 mmol) and DDQ (1,57 g, 6,8 mmol) were dissolved in dry toluene (35 ml + 35 ml) and then added in 250 ml three necked round bottom flask predegassed.
The mixture was stirred for 30 min at room temperature. TLC control did not show the starting product monomer 1 anymore. Then 5,6 ml (4,7 mmol) of distilled N,N-diisopropylethylamine DIPEA was added and the mixture was stirred at room temperature for 1hour and 30 min.
Then 5,7 ml (6,8 mmol) of boron trifluoride-diethyl ether ($BF_3O(Et)_2$) was added and the mixture was heated and stirred at 80°C for 2 hours. The mixture showed an orange fluorescence.
After 2 hours the mixture was cooled down to room temperature and the crude was washed with water (3 time) and dried over $MgSO_4$.
The solvent was removed under reduced pressure.
A TLC using as eluents 2:1 dichloromethane/ hexane show a fluorescent orange spot and two light red spot.
Monomer 2 was purified through silica gel chromatography using as eluents dichloromethane/hexane 2:1.
The product (1,43 gr, 40% yield) is a red-orange oil.

^{1}H NMR ($CDCl_3$, 400 MHz): δ 7.9 (s, 2H), 7.44 (d, J = 3.6 Hz, 1H), 7.32 (d, J = 3.6 Hz, 2H), 6.97(d, J = 3.2 Hz, 1H), 6.57 (m, 2H), 2.92 (t, J = 7.6 Hz, 2H), 1.76 (m, 2H), 1.29 (m, 10H), 0.89 (t, J = 6.8 Hz, 3H).

^{13}C NMR ($CDCl_3$, 100MHz): δ 154.21, 143.11, 133.79, 132.13, 131.30, 125.88, 118.19, 31.83, 31.49, 29.26, 28.18, 22.85, 14.19, 0.99.

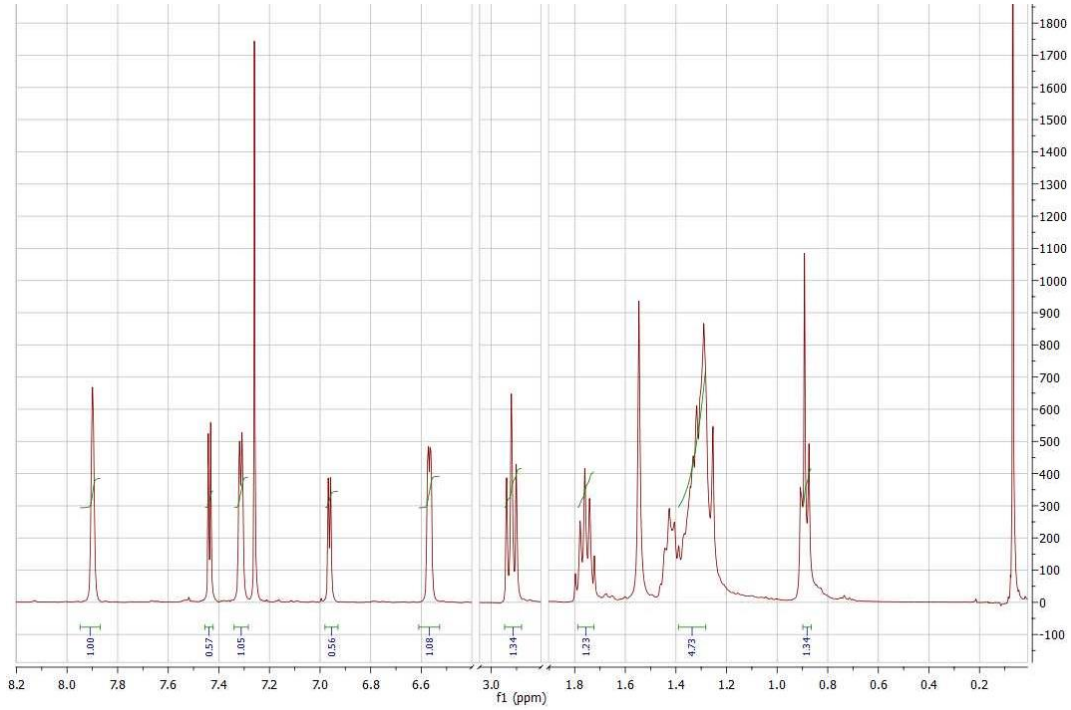

Figure 33. ^{1}H-NMR of 8-octylthiophene BODIPY (2).

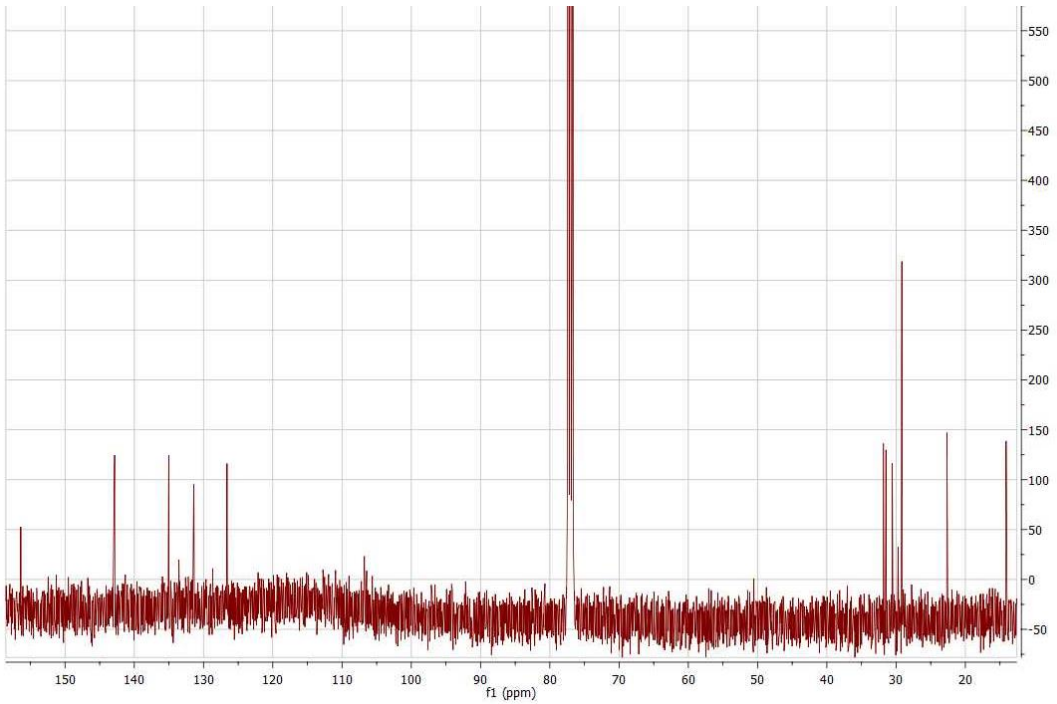

Figure 34. ^{13}C-NMR of 8-octylthiophene BODIPY (2).

5.2.3 2,6-dibromo-8-octylthiophene BODIPY (3)

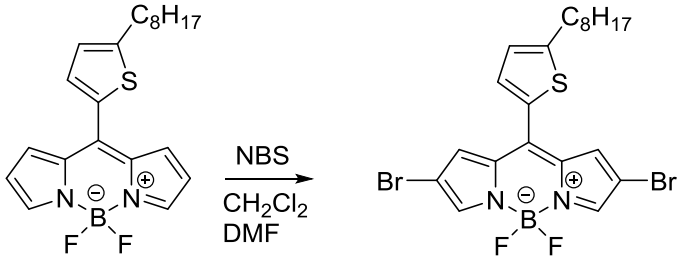

(3)

Procedure

To a solution of monomer 2 (0,200g, 0,52 mmol) in dry methylene chloride (13 ml) and dry dimethylformamide (13 ml) N-bromosuccinimide (NBS) (0,222 g) was added portion wise 3 times every 10 min. The mixture was stirred at room temperature and in the dark for 2 hours.
After TLC control, the crude was diluted in dichloromethane and washed with brine for three times. The organic phase was dried over $MgSO_4$ and the solvent was removed under reduced pressure.
The crude product was purified by silica-gel column chromatography using at the beginning hexane as eluent and then incresing slowly the polarity to 7:3 hexane/dichloromethane.
The product (0,120 g, 50%) is a dark pink solid .

^{1}H NMR ($CDCl_3$, 400 MHz): δ 7.8 (s, 2H), 7.48 (d, 1H), 7.32 (s, 2H), 7.0 (d, 1H), 2.93 (t, 2H), 1.77 (m, 2H), 1.38 (m, 10H), 0.90 (t, 3H).

^{13}C NMR ($CDCl_3$, 100MHz): δ 156.36, 142.84, 135.02, 131.40, 126.61, 31.83, 31.46, 30.55, 29.24, 29.17, 22.65, 14.11.

MALDI m/z, calcd for $C_{21}H_{23}BBr_2F_2N_2S$ (M^+): 543.10; found: 543.14

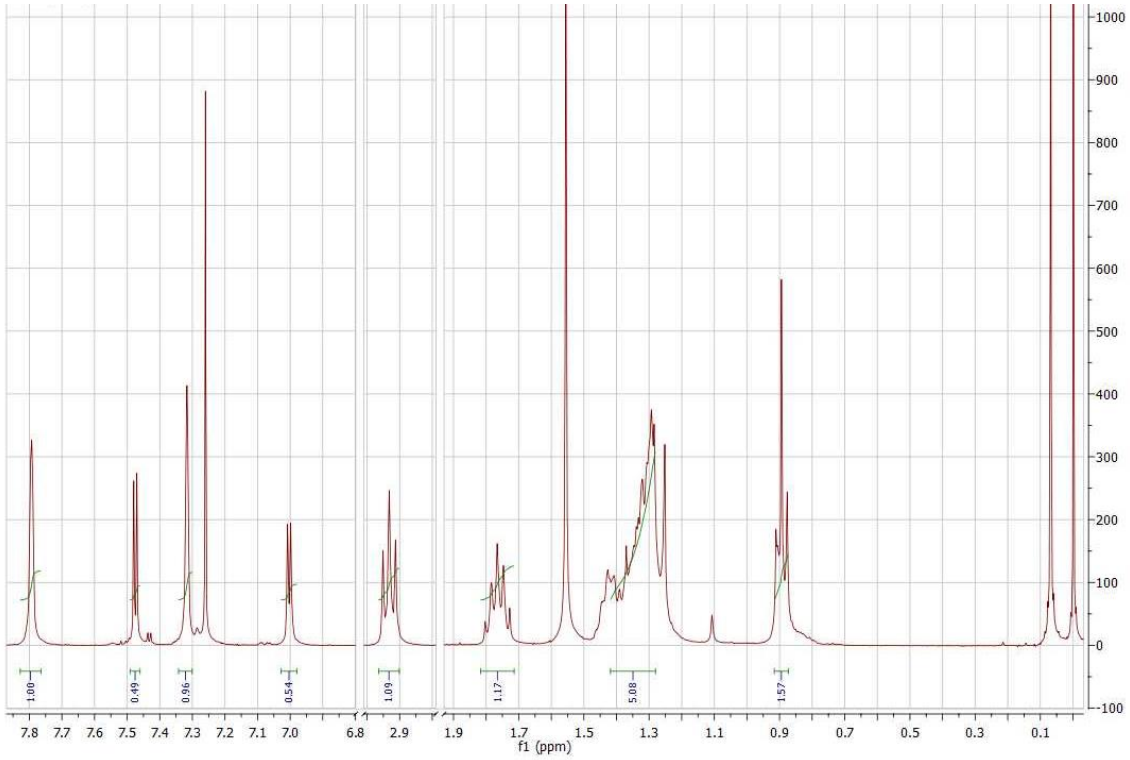

Figure 35. ^{1}H-NMR of 2,6-dibromo-8-octylthiophene BODIPY (3).

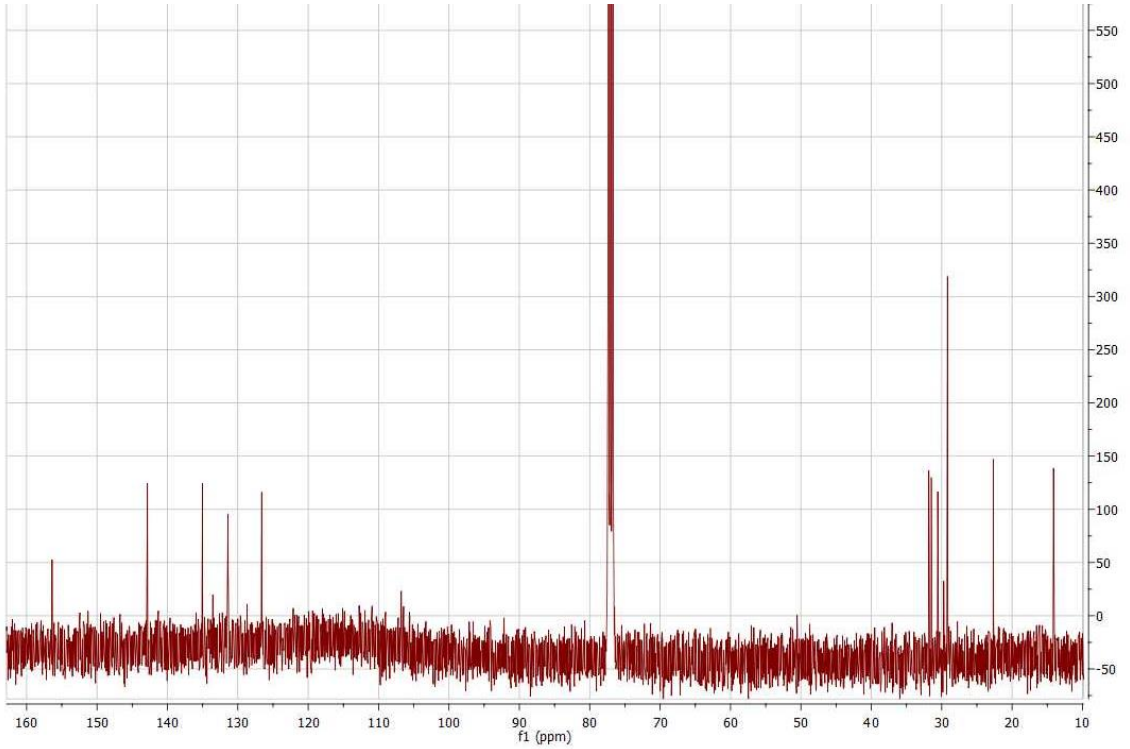

Figure 36. ^{13}C-NMR of 2,6-dibromo-8-octylthiophene BODIPY (3).

5.2.4 5,5-difluoro-10-(5-octylthiophen-2-yl)-2,8-di(thiophen-2-yl)-5H-4λ⁴,5λ⁴-dipyrrolo[1,2-c:2',1'-f][1,3,2]diazaborinine (4)

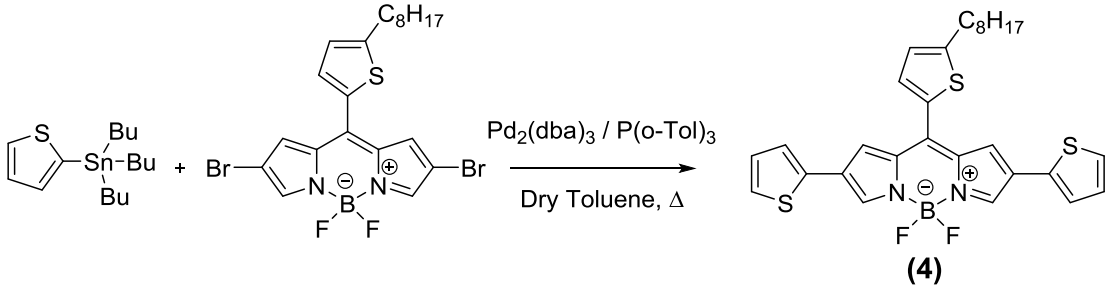

(4)

Procedure

A solution of the commercially available 2-tributylstannylthiophene (2.3 mol) and the 2,8-dibromo-5,5-difluoro-10-(5-octylthiophen-2-yl)-5*H*-4λ⁴,5λ⁴-dipyrrolo[1,2-*c*:2',1'-*f*][1,3,2]diazaborinine (**3**) (0.92 mol) were combined in dry deoxygenated toluene in the presence of tris(dibenzylideneacetone)dipalladium(0) [$Pd_2(dba)_3$] (2 mol%) and tri-*o*-tolylphosphine [P(*o*-Tol)$_3$] (4 mol%) and the mixture was heated to ca. 120 °C for 4 hours. Then, the reaction mixture was filtered through a pad of celite and the toluene solution was evaporated and dried under high vacuum. Purification was achieved by silica gel chromatography using as eluent a hexane/chloroform mixture (1:1). The resulting pure compound is an orange solid with yield 79% (0.40 g).

^{1}H NMR ($CDCl_3$, 300 MHz): δ 8.14 (s, 2H), 7.53 (d, 1H), 7.33 (s, 2H), 7.24 (dd, ^3J = 7.24, 2H), 7.21 (dd, ^3J = 7.21, 2H), 7.05 (dd, ^3J = 7.05, 2H), 7.04 (d, 1H), 2.97 (t, 2H), 1.80 (quintuplet, 2H), 1.46 (m, 12H), 0.90 (t, 3H).

^{13}C NMR ($CDCl_3$, 100 MHz): δ 154.72 (s), 140.74 (s), 139.03 (s), 135.90 (s), 134.57 (s), 134.08 (s), 131.98 (s), 128.02 (m), 127.90 (s), 126.14 (s), 124.69 (s), 124.28 (s), 123.35 (s), 99.51 (s), 31.82 (s), 31.44 (s), 30.48 (s), 29.69 (m), 29.26-29.18 (t), 22.63 (s), 14.08 (s)

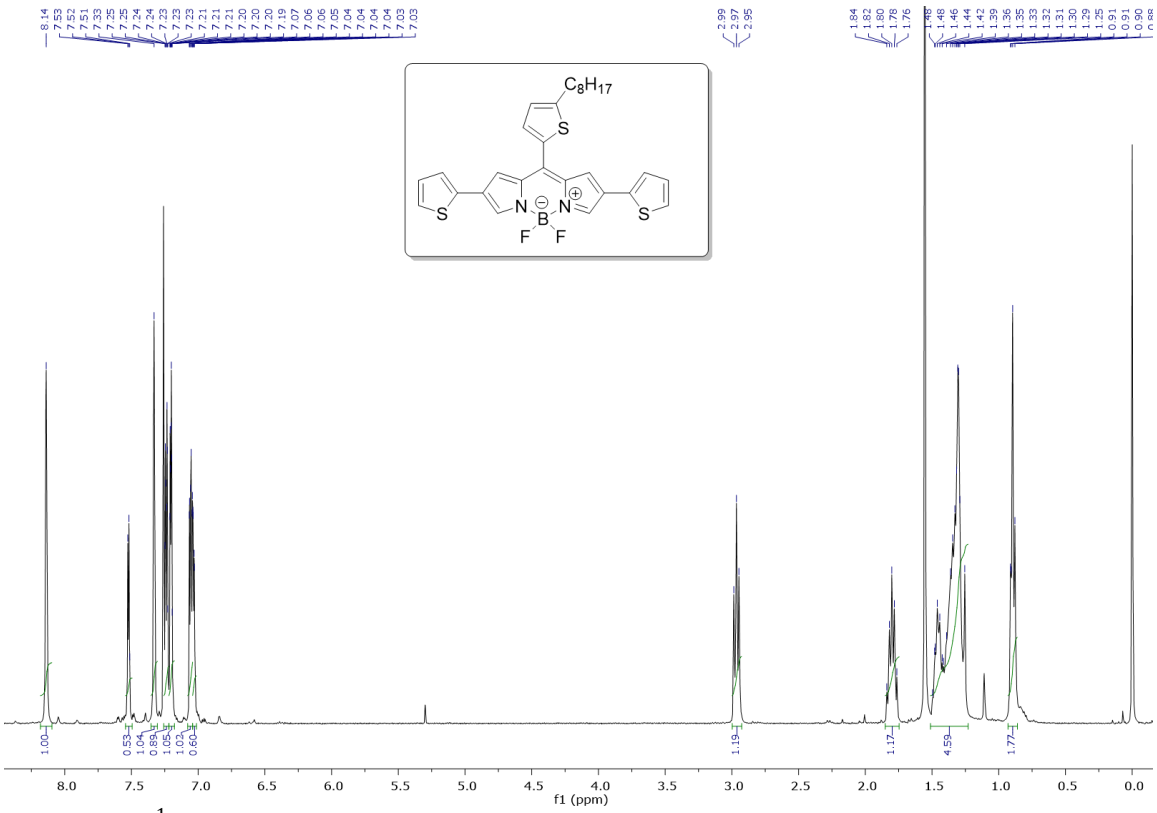

Figure 37. ^{1}H-NMR spectrum of 5,5-difluoro-10-(5-octylthiophen-2-yl)-2,8-di(thiophen-2-yl)-5*H*-4λ^4,5λ^4-dipyrrolo[1,2-*c*:2',1'-*f*][1,3,2]diazaborinine (**4**).

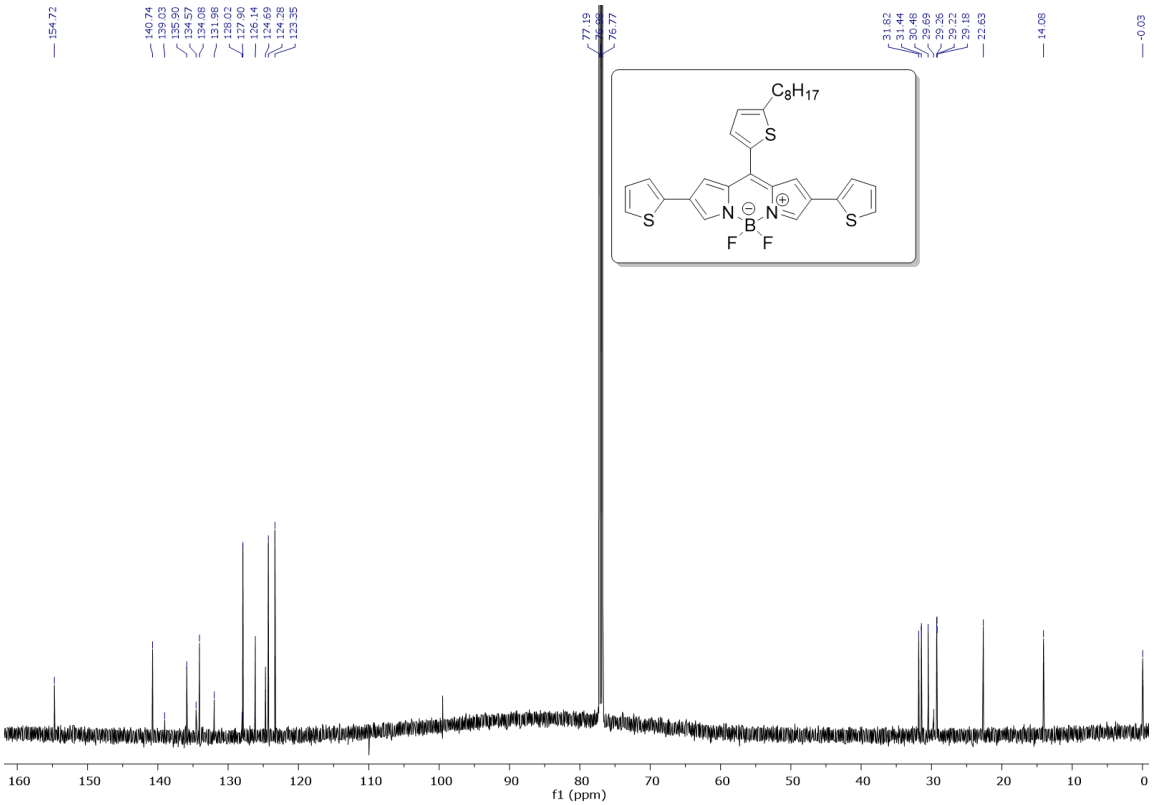

Figure 38. ^{13}C-NMR spectrum of 5,5-difluoro-10-(5-octylthiophen-2-yl)-2,8-di(thiophen-2-yl)-5*H*-4λ^4,5λ^4-dipyrrolo[1,2-*c*:2',1'-*f*][1,3,2]diazaborinine (**4**).

5.2.5 2,8-bis(5-bromothiophen-2-yl)-5,5-difluoro-10-(5-octylthiophen-2-yl)-5H-4λ⁴,5λ⁴-dipyrrolo[1,2-c:2',1'-f][1,3,2]diazaborinine (5)

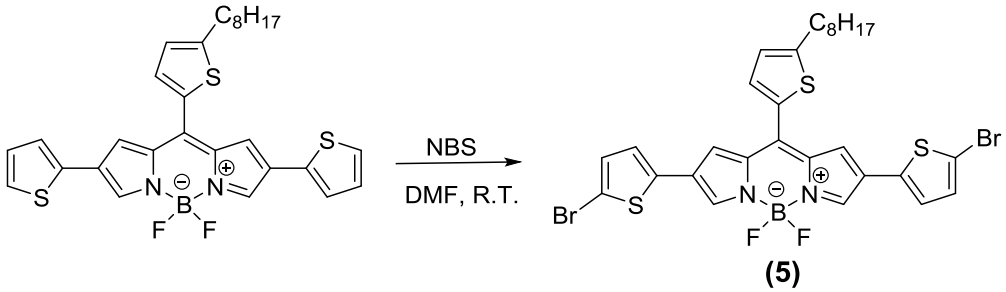

(5)

Procedure

In a predegassed flask, **4** (0.72 mol) was dissolved in freshly dried DMF, then recrystallized NBS (1.44 mol) was added portion wise (three times) in a period of 30 minutes. The mixture was stirred at room temperature for 3 hours. The mixture was diluted in chloroform and washed with water three times. The solvent was removed under reduced pressure and the crude compound was purified through silica gel chromatography using as eluent a hexane/chloroform mixture (7:3). The resulting pure compound is a red-orange solid with yield 68%.

^{1}H NMR ($CDCl_3$, 300 MHz): δ 8.07 (s, 2H), 7.51 (d, 1H), 7.04 (d, 2H), 7.0 (d, 1H), 6.95 (d, 2H), 2.97 (t, 2H), 1.80 (quintuplet, 2H), 1.31 (m, 12H), 0.90 (t, 3H).

^{13}C NMR ($CDCl_3$, 100 MHz): δ 155.28 (s), 140.37 (s), 139.36 (s), 137.47 (s), 134.53-134.36 (d), 131.83 (s), 130.73 (s), 127.21 (s), 126.30 (s), 124.60 (s), 123.53 (s), 110.95 (s), 31.81 (s), 31.42 (s), 30.50 (s), 29.67 (s), 29.25-29.17 (t), 22.63 (s), 14.07 (s)

m/z [FD+(eiFI)]: 704.98 (M^+-1, 12%), 705.97 (M^+, 50%), 706.97 (MH^+, 40%), 707.97 (MH^++1, 100%), 708.97 (MH^++2, 49%), 709.97 (MH^++3, 77%), 710.97 (MH^++4, 22%), 711.97 (MH^++5, 11%)

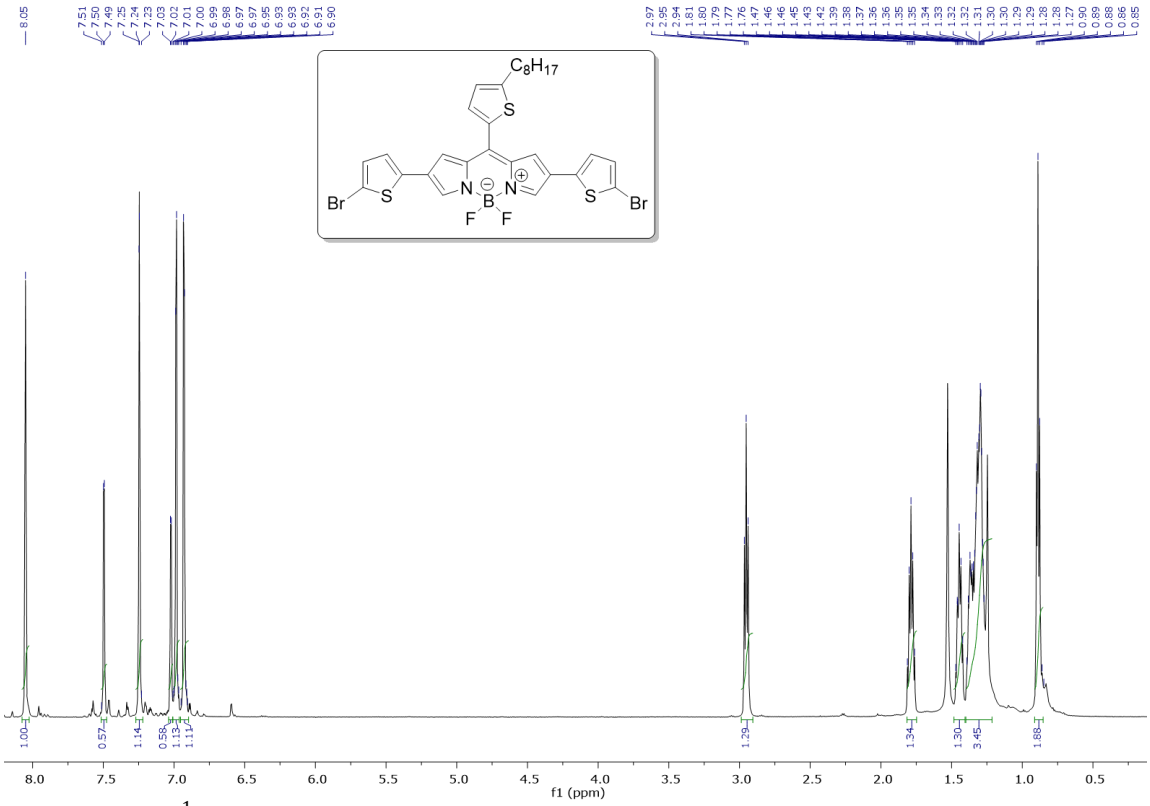

Figure 39. ^{1}H-NMR spectrum of 2,8-bis(5-bromothiophen-2-yl)-5,5-difluoro-10-(5-octylthiophen-2-yl)-5*H*-4λ^4,5λ^4-dipyrrolo[1,2-*c*:2',1'-*f*][1,3,2]diazaborinine (**5**).

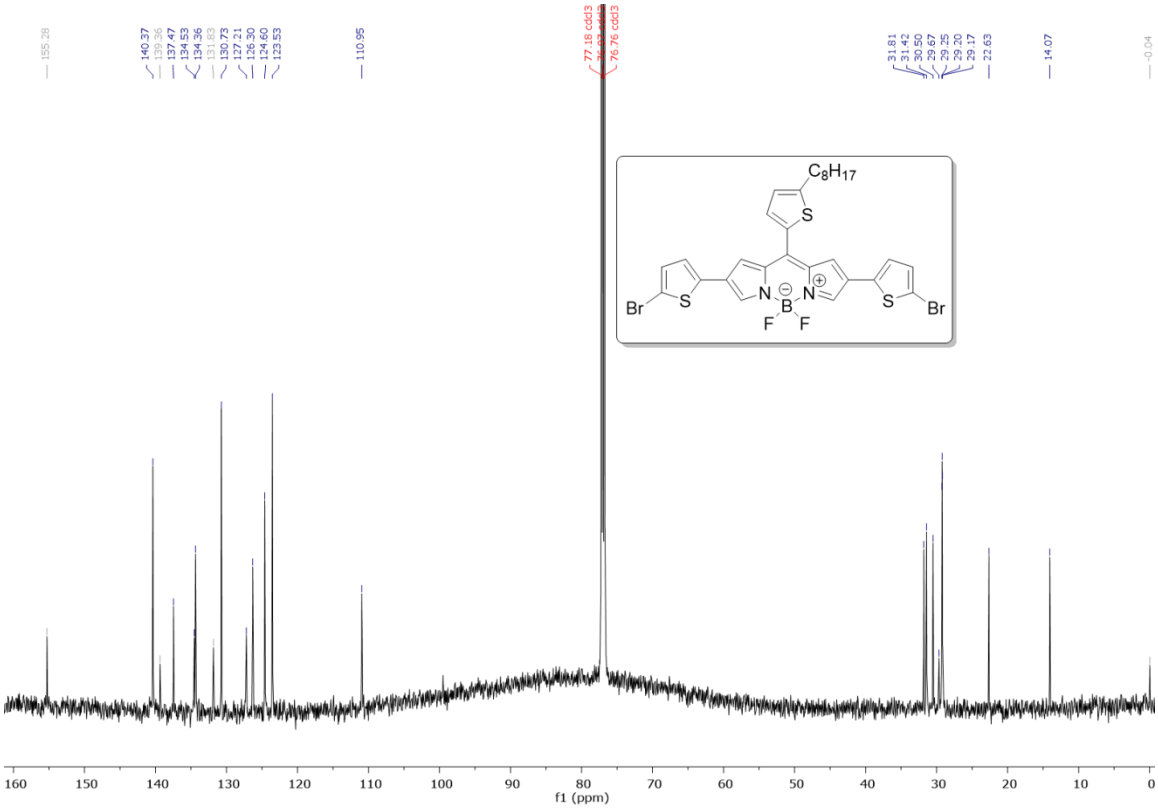

Figure 40. ^{13}C-NMR spectrum of 2,8-bis(5-bromothiophen-2-yl)-5,5-difluoro-10-(5-octylthiophen-2-yl)-5*H*-4λ^4,5λ^4-dipyrrolo[1,2-*c*:2',1'-*f*][1,3,2]diazaborinine (**5**).

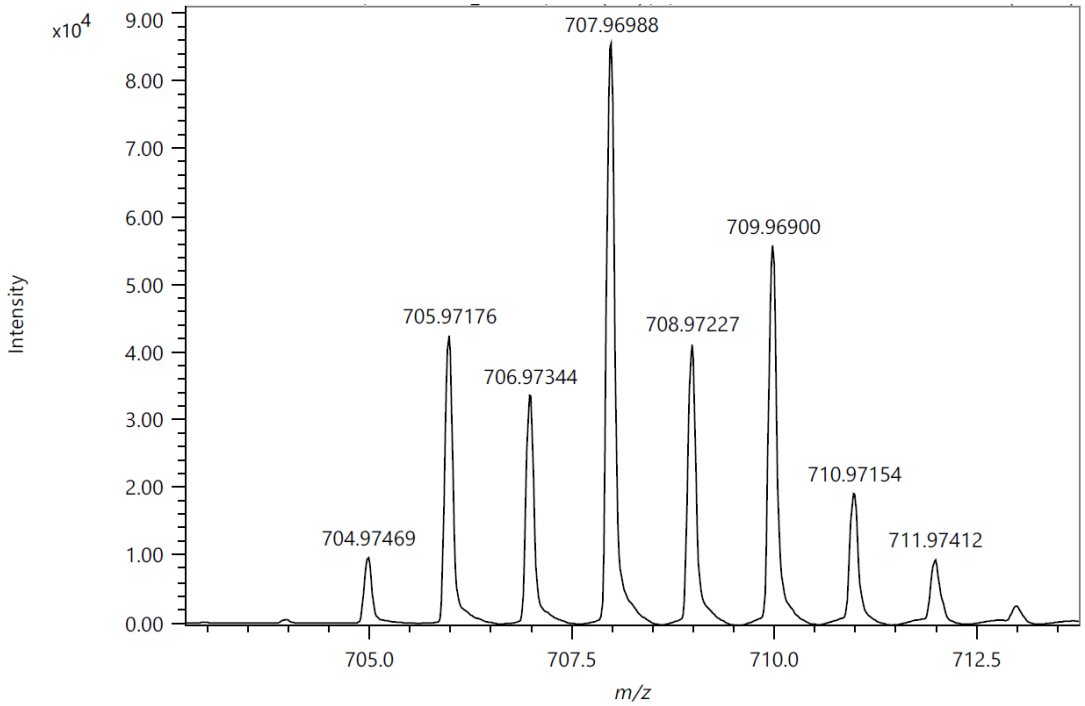

Figure 41. FD+(eiFI) mass spectrum of 2,8-bis(5-bromothiophen-2-yl)-5,5-difluoro-10-(5-octylthiophen-2-yl)-5*H*-4λ^4,5λ^4-dipyrrolo[1,2-*c*:2',1'-*f*][1,3,2]diazaborinine (**5**).

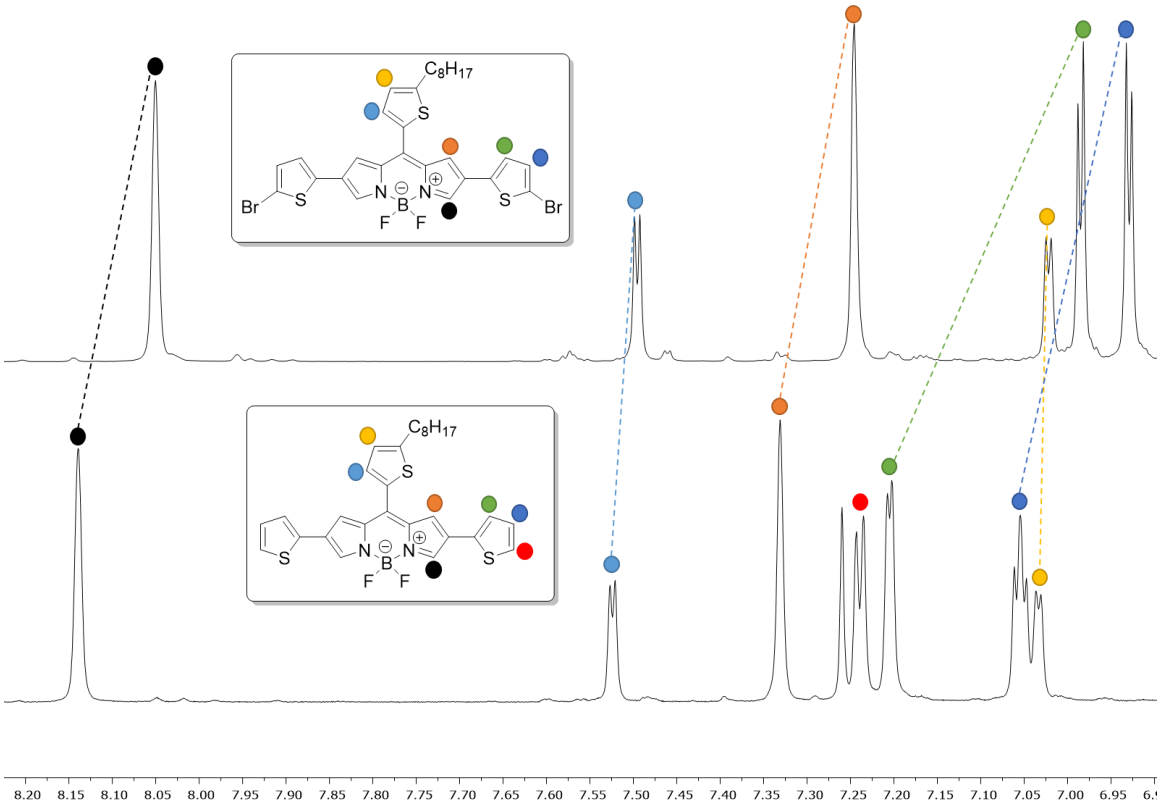

Figure 42. Aromatic region (6.90-8.20 ppm) of the ^{1}H-NMR spectra of monomers **4** and **5** with assignment of the representative protons.

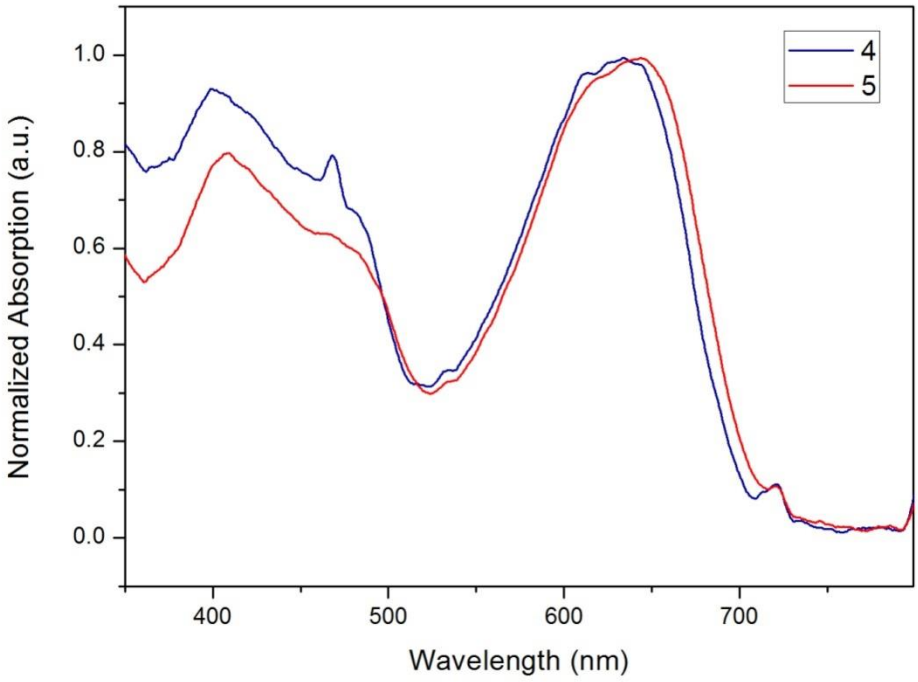

Figure 43. Absorption spectra in chloroform solution of monomers **4** and **5**.

5.2.6 2,2'-((5-bromothiophen-2-yl)methylene)bis(1H-pyrrole)(6)

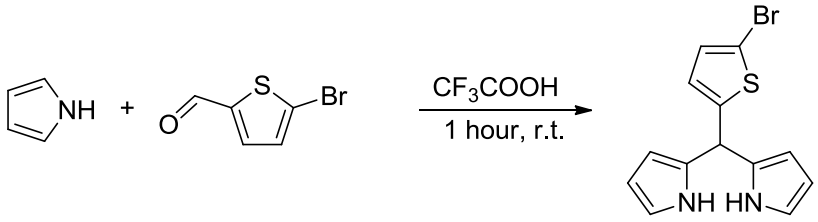

(6)

5-bromothiophene-2-carbaldehyde (2.13 g, 11.16 mmol) was dissolved in excess of pyrrole (31 mL, 446.4 mmol). The resulting mixture was degassed for 30 min by argon and then 0.1 mL of trifluoroacetic acid were added. The reaction was stirred at room temperature for an hour and the crude product was diluted with methylene chloride and washed three times with sodium hydroxide (NaOH) aq. 0.1 N and dried over $MgSO_4$. The solvent was removed under reduced pressure. The product was purified by chromatography on silica gel using hexane/ethyl acetate 9:1 as eluent. The yellow-green solid crude product obtained with a yield of 95% (3.29 g).

^{1}H NMR crude ($CDCl_3$, 400 MHz): δ 5.65 (s, 1H), 6.07 (m, 2H), 6.18 (m, 2H), 6.64(dd, ^{3}J= 6,64Hz, 1H), 6.70 (t, 3J = 6.71Hz, 2H), 8.0 (s, 2H).

Figure 44. ^{1}H-NMR of 2,2'-((5-bromothiophen-2-yl)methylene)bis(1H-pyrrole) crude (**6**).

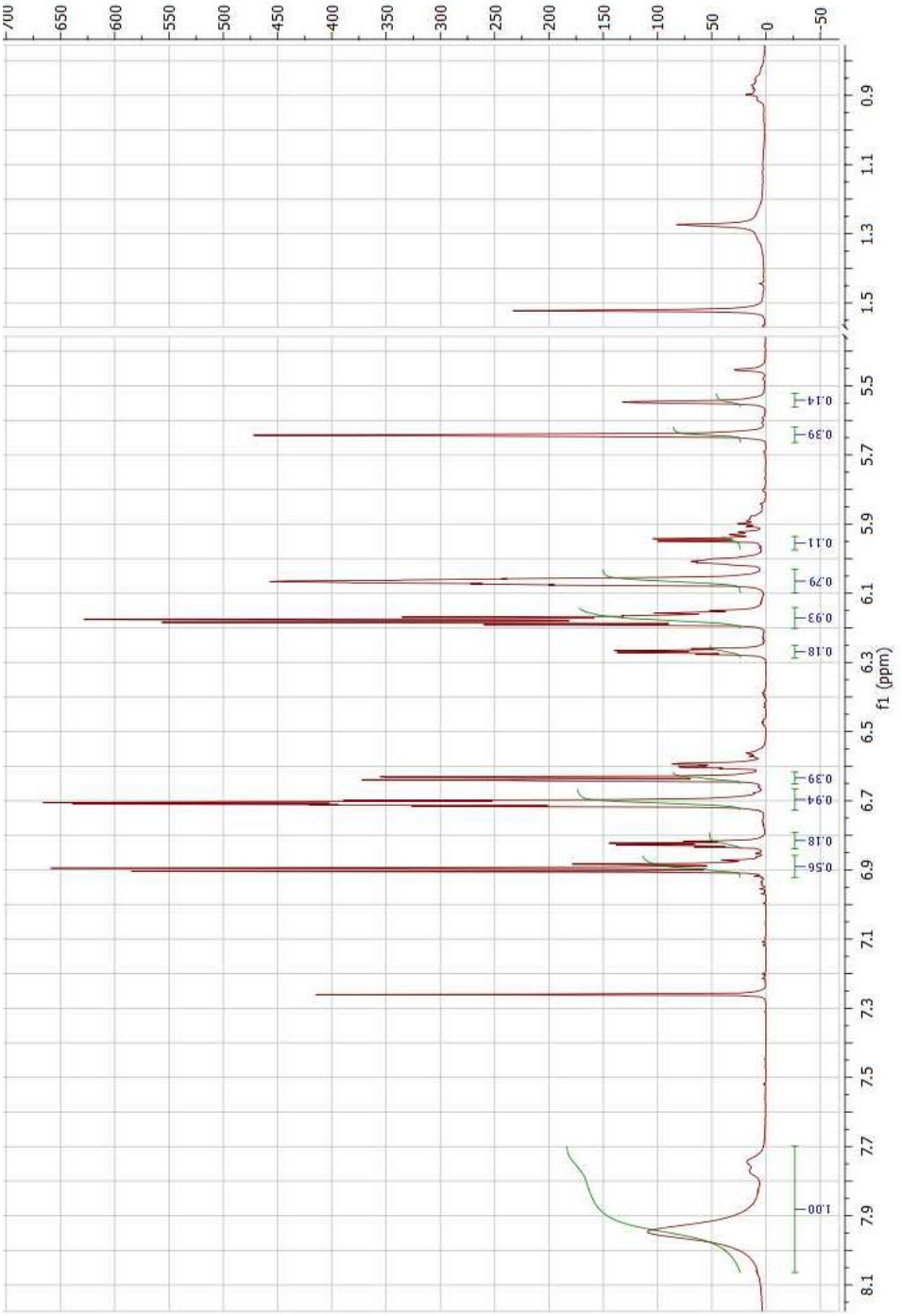

5.2.7 Bromo functionalized-BODIPY monomer (7)

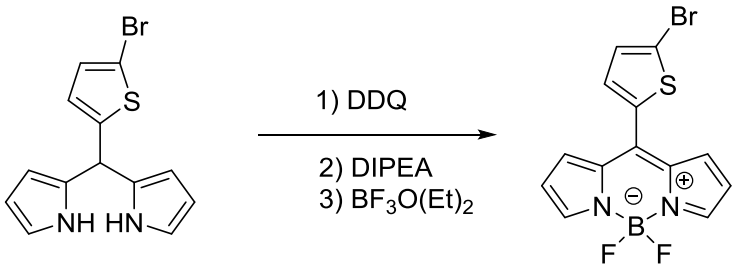

(7)

Monomer **6** (3.29 g, 10.70 mmol) and the DDQ (2.43 g, 10.70 mmol) were dissolved in dry toluene (54 mL + 54 mL) and then added in a predegassed three necked flask. After 30 min the predistilled Hünig's base (DIPEA, 8.8 mL) was added and the mixture was stirred at room temperature for 90 min. Finally, the boron trifluoride diethyl etherate (9 mL) was added and the mixture was stirred at 80°C for 2h and then cooled at room temperature. The crude product was washed with water and dried on $MgSO_4$. The solvent was removed under reduced pressure and the product was purify by silica gel chromatography using a mixture of dichloromethane:hexane 2:1 as eluent. The product was obtained as a pink solid with a yield of 49% (1.87 g).

^{1}H NMR ($CDCl_3$, 400 MHz): δ 6.6(d, 2H), 7.27 (dd, ^{3}J=7.27, 3H), 7.35 (d, 1H), 7.96 (s, 2H).

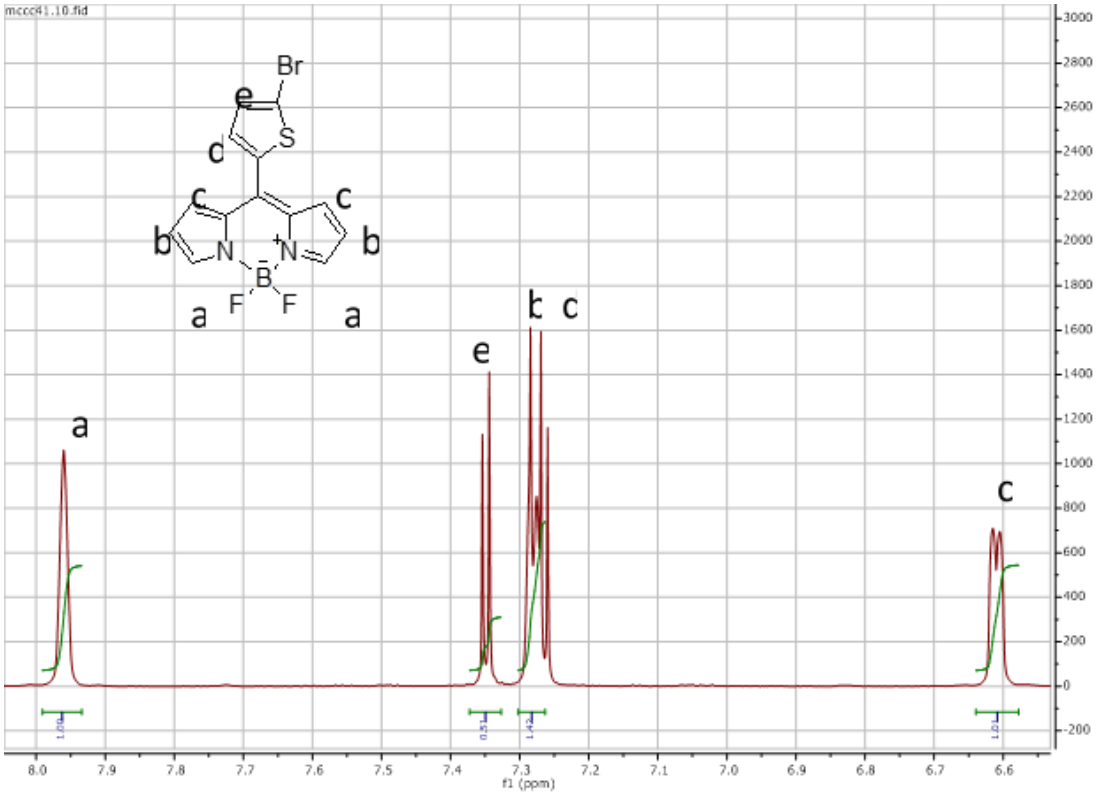

Figure 45. ^{1}H-NMR of Intermediate BODIPY monomer **7**.

5.2.8 Synthesis of NIRBDTE

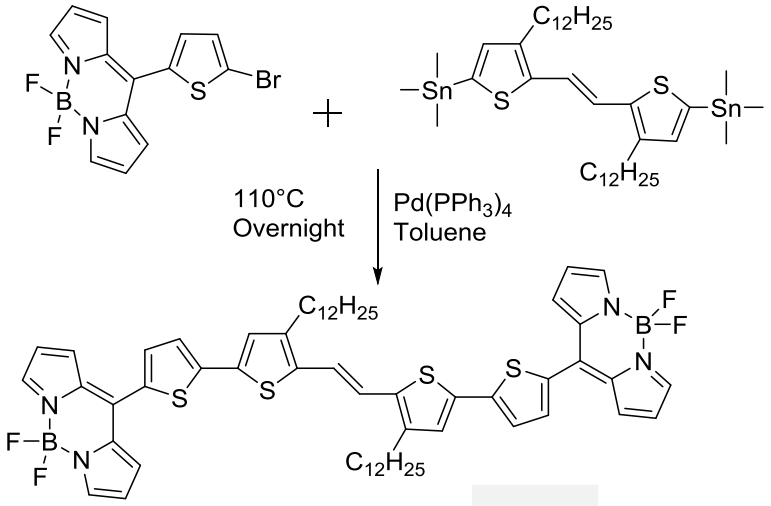

NIRBDTE

To a mixture of BODIPY intermediate monomer 7 (0.22 g, 0.26 mmol), distannyl-1,2-di(2-thienyl)ethylene (DTE) (0.23 g, 2,5 eq) and tetrakis(triphenylphosphine)palladium (5%, 14.9 mg) toluene (5 mL) was added. The mixture was stirred overnight at 110 °C. The crude product was cooled down and toluene was removed under reduced pressure. The crude product was purified by silica-gel column chromatography using a mixture of hexane: dichloromethane 7:3 eluent and then recrystallized from hexane to afford compound NIRBDTE. The product obtained as a purple solid with a yield of 76% (0.21 g).

^{1}H NMR ($CDCl_3$, 400 MHz): δ 1,30(m, 42H), 1,67 (m, 4H), 2.70 (t, 4H), 6,60 (dd, ^{3}J = 6.60Hz, 4H), 7.02 (s, 2H), 7.14 (s, 2H), 7.35 (d, 2H), 7.37 (d, 4H), 7.55 (d, 2H), 7.93 (s, 4H).

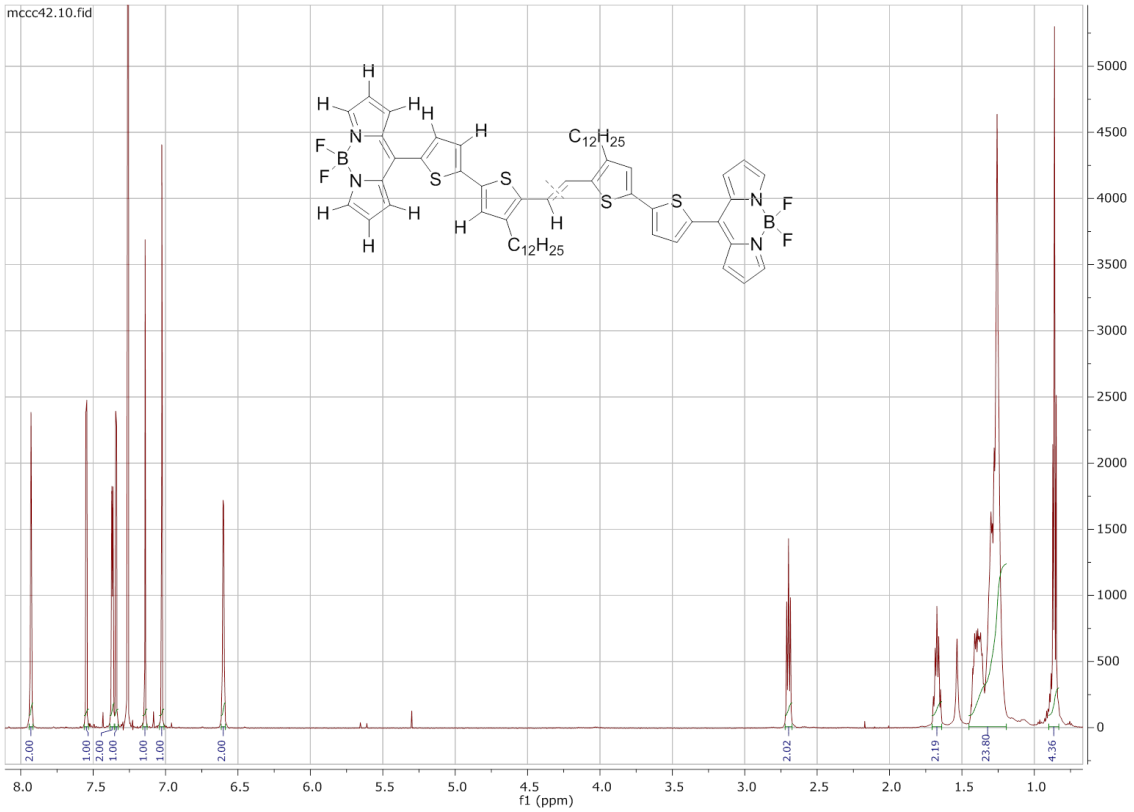

Figure 46. ^{1}H-NMR of NIRBDTE.

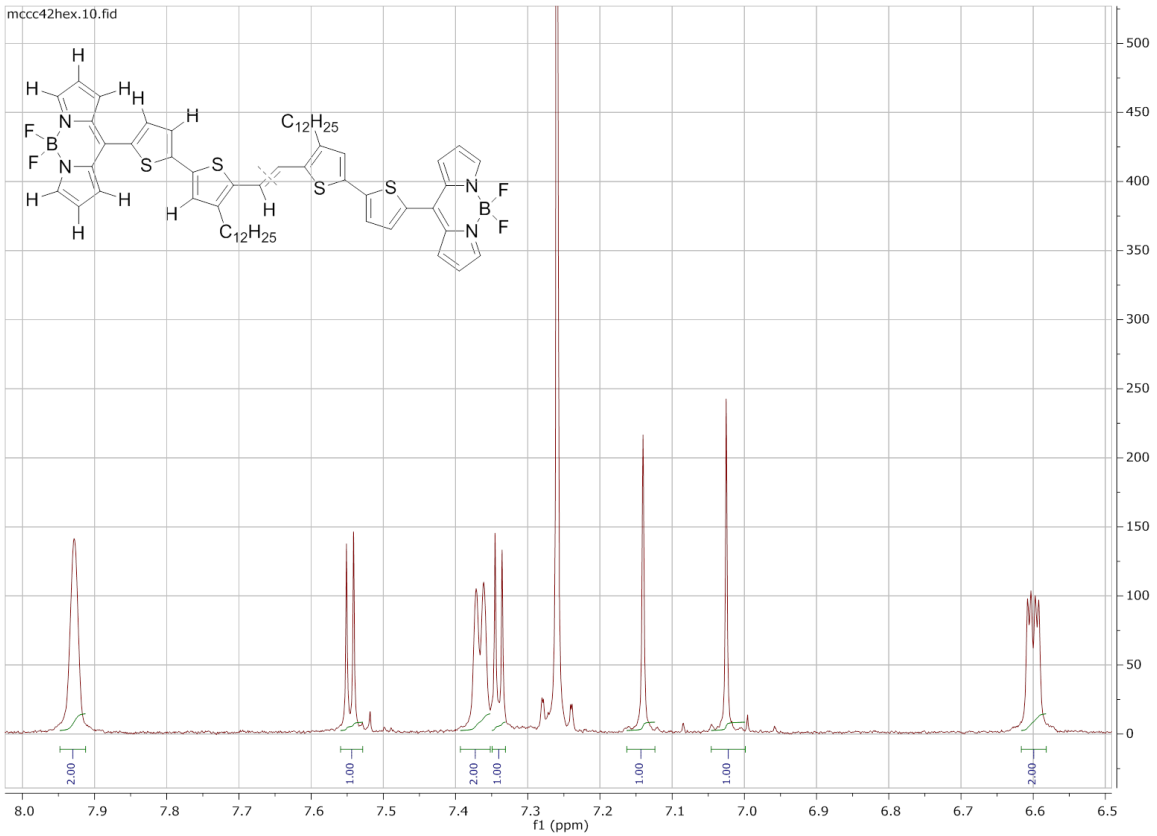

Figure 47. ^{1}H-NMR of NIRBDTE (aromatic region).

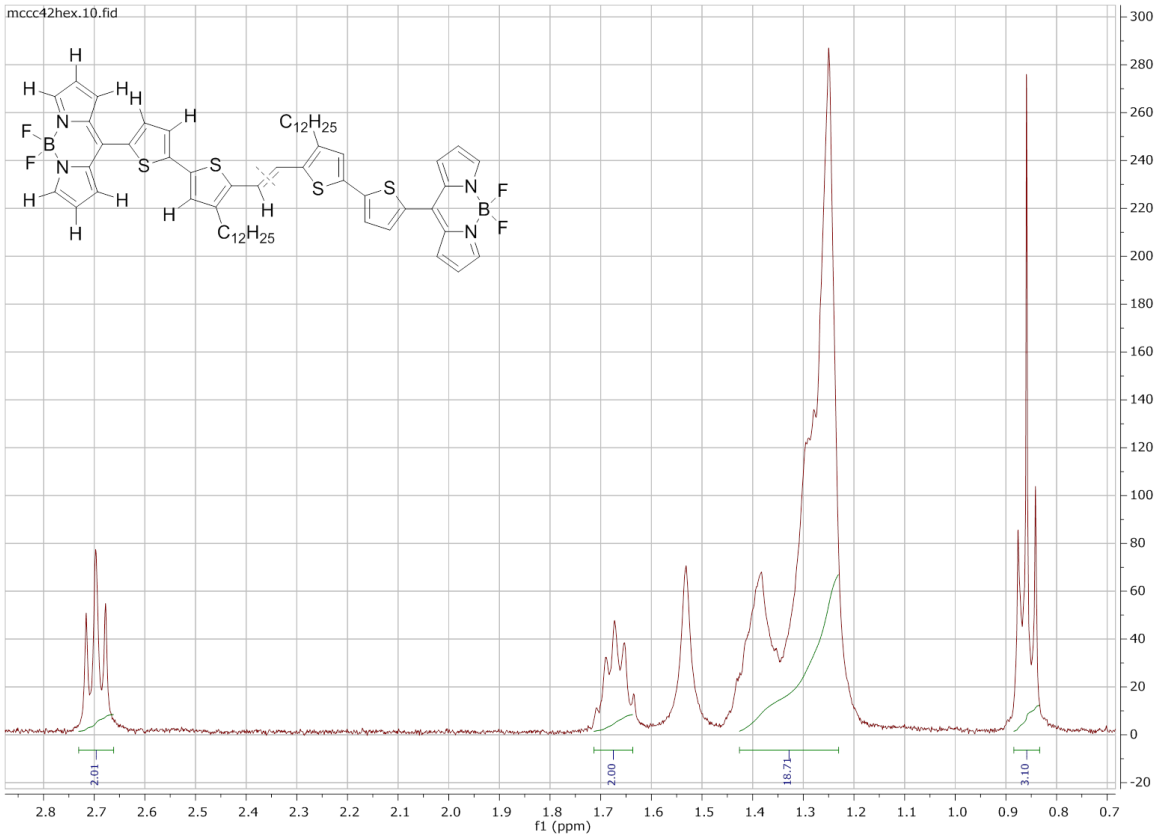

Figure 48. ^{1}H-NMR of NIRBDTE (aliphatic region).

MALDI-TOF Analysis of NIRBDTE

NIRBDTE has been further analyzed by MALDI-TOF (Bruker Reflex TOF in MPI Mainz) and the spectra is presented in Figure 49. As can be seen, one main peak at 1073,24 which corresponds to the molecular weight of NIRBDTE is appeared.

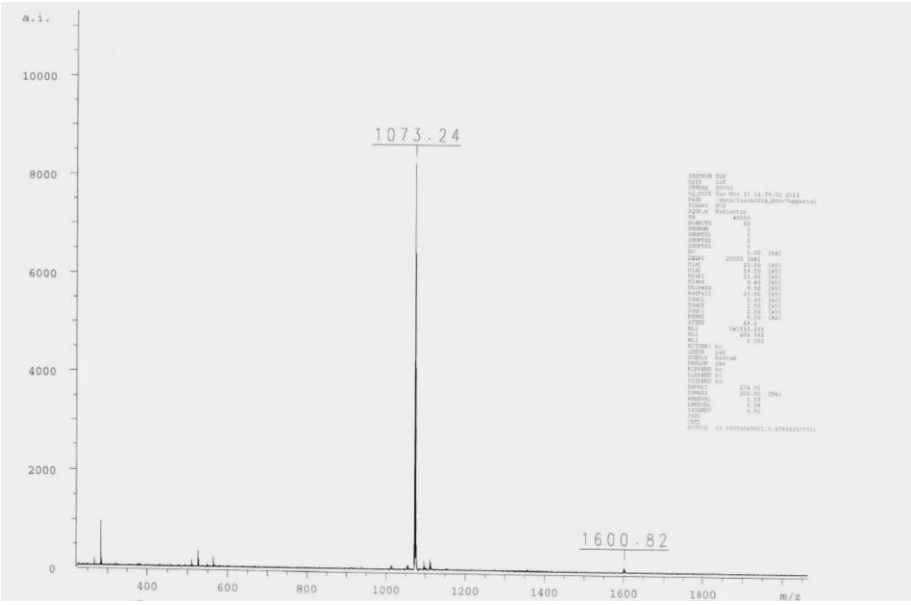

Figure 49. MALDI-TOF spectrum of NIRBDTE.

5.2.9 Polymer TBDPTV

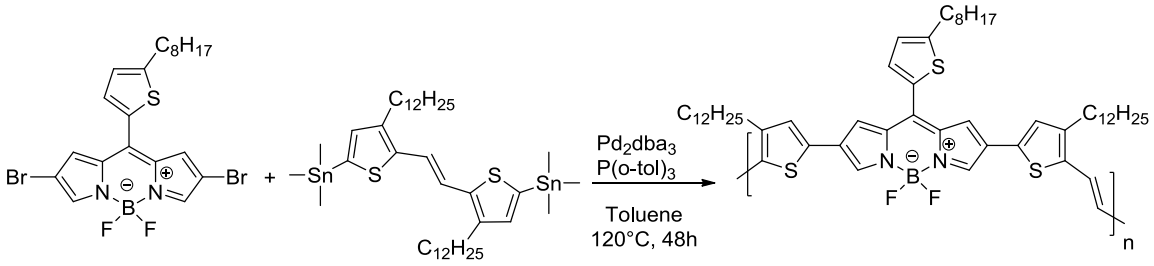

Procedure

Monomer 3 (0.202 mmol, 110 mg) and (E)-1,2-bis(3-dodecyl-5-(trimethylstannyl)thiophen-2-yl)ethene (0.202 mmol, 172.8 mg) were dissolved in dry toluene (8.1 mL). Then, Pd_2dba_3 (0.0101 mmol, 9.3 mg) and $P(o\text{-}tol)_3$ (0.0808 mmol, 24.6 mg) were added and the reaction mixture was stirred at 120°C under argon atmosphere for 48h. Then, the toluene solution was evaporated, the mixture was solubilized in $CHCl_3$. The polymer was purified by precipitation in methanol, filtered and washed on Soxhlet apparatus with methanol, hexane and chloroform. The chloroform fraction was evaporated under reduced pressure and the polymer was precipitated in acetone, filtered and finally dried under high vacuum, providing a greenish solid (52 mg).

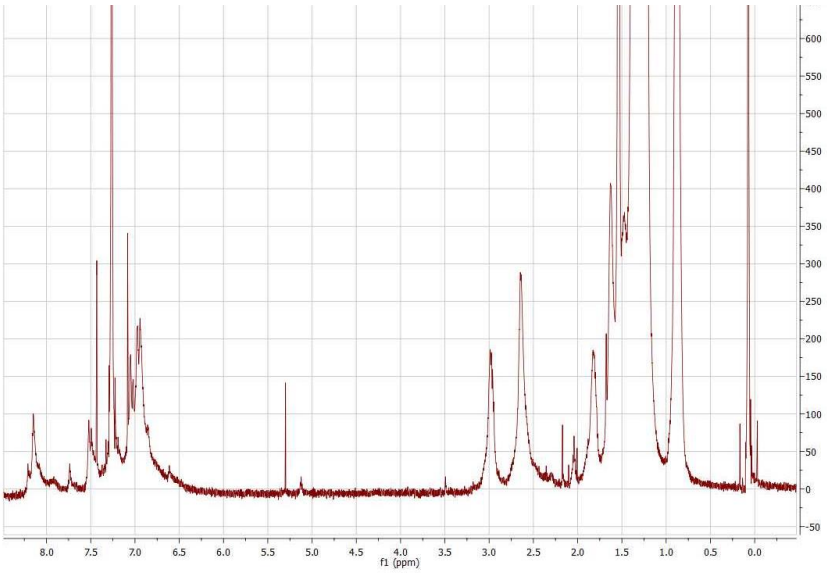

Figure 50. ^{1}H-NMR of TBDPTV

5.2.10 Polymer BODIPY-qTo

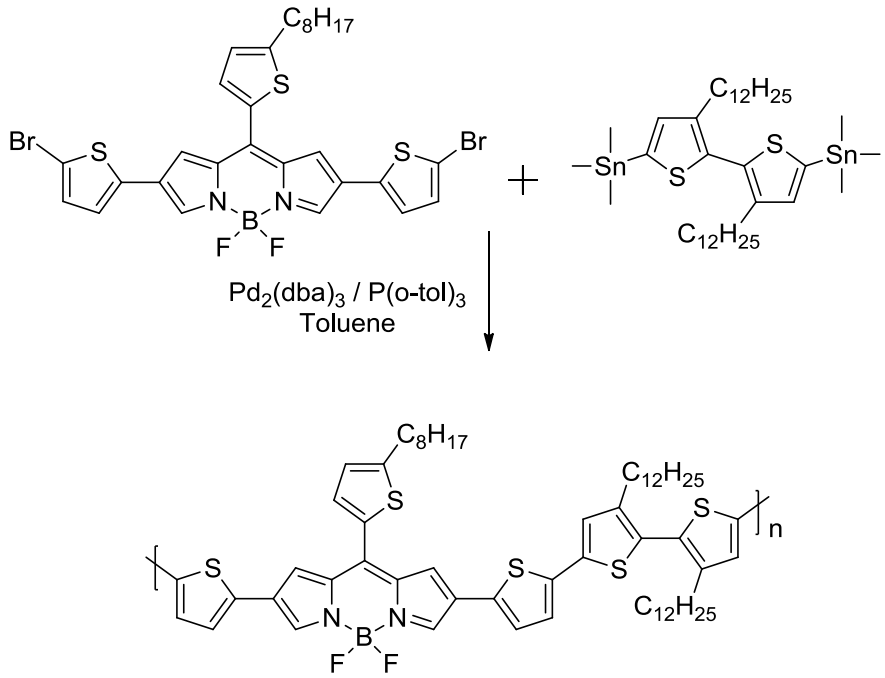

Procedure

A mixture of monomer 5 (110mg, 0,155 mmol), (3,3'-didodecyl-[2,2'-bithiophene]-5,5'-diyl)bis(trimethylstannane) (128 mg, 0,155mmol), $Pd_2(dba)_3$ (4,3 mg,0,0046 mol) , $P(o\text{-}tol)_3$ (2,8 mg, 0,0093 mmol) were added in dried flame two neck round bottom flask. Then dry toluene (12,4 mL) was added through a syringe and the reaction mixture started stirring and heating at 110° C for 48h.

Then 2-bromothiophene (0,15 ml, 1,55mmol) was added to the reaction and let it stir for 4 h, then 2-tributylstannylthiophene (0,49 ml,1,55 mmol) was added. The day after the reaction was cooled down and the compound was precipitated in methanol. Then the precipitate was filtered and purified with Soxhlet extraction using acetone, DCM and chloroform as solvents. The chloroform fraction was evaporated under reduced pressure and the polymer was precipitated in acetone, filtered and finally dried under high vacuum, providing a brownish solid (52 mg).

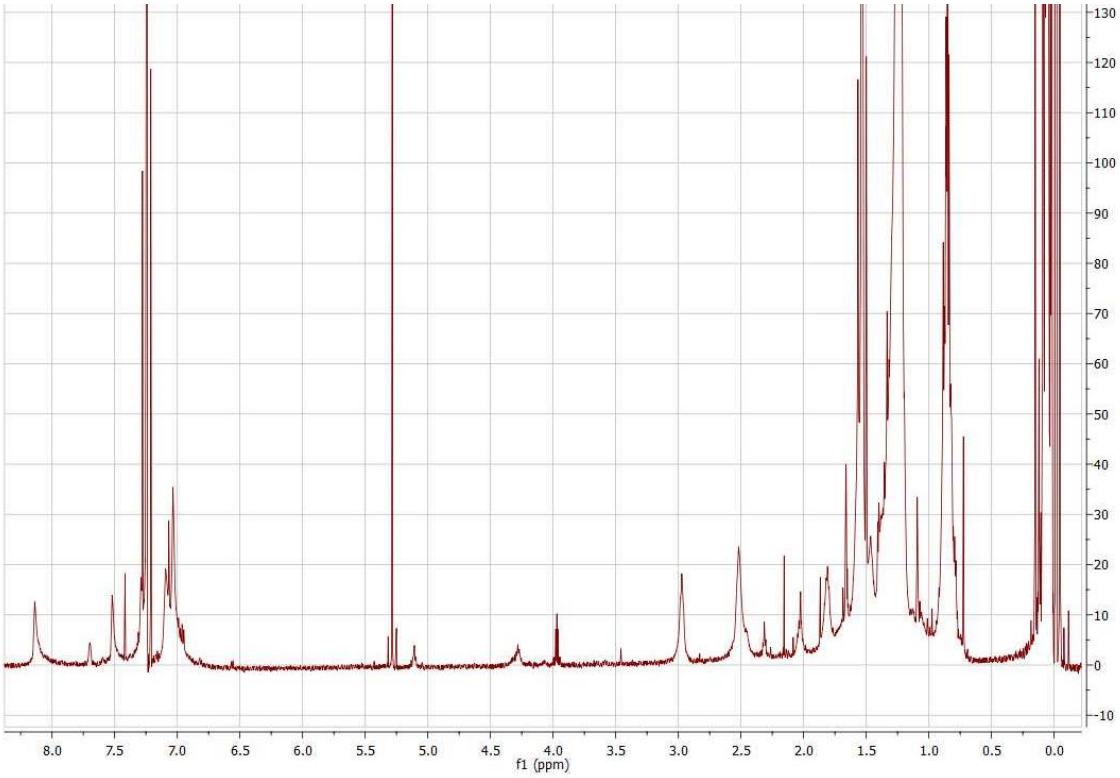

Figure 51. ^{1}H-NMR of BODIPY-qT*o*.

5.2.11 Polymer BODIPY-qTi

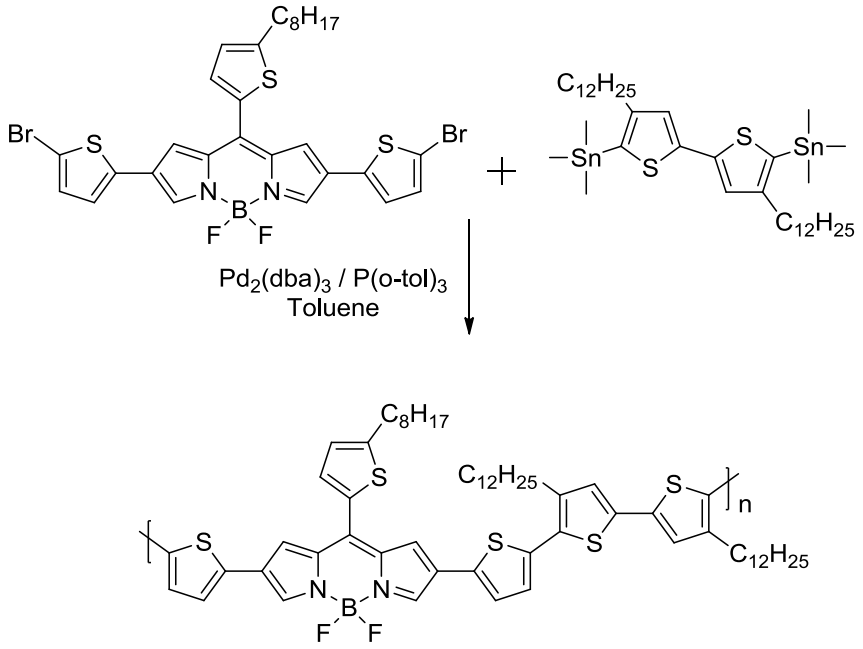

Procedure

A mixture of monomer 5 (110mg, 0,155 mmol), (4,4'-didodecyl-[2,2'-bithiophene]-5,5'-diyl)bis(trimethylstannane) (128 mg, 0,155mmol), $Pd_2(dba)_3$ (4,3 mg,0,0046 mol) , $P(o\text{-}tol)_3$ (2,8 mg, 0,0093 mmol) were added in dried flame two neck round bottom flask. Then dry toluene (12,4 mL) was added through a syringe and the reaction mixture started stirring and heating at 110° C for 48h.

Then 2-bromothiophene (0,15 ml, 1,55mmol) was added to the reaction and the reaction mixture was stirred for 4 h, then 2-tributylstannylthiophene (0,49 ml,1,55 mmol) was added . The day after the reaction was cooled down and the compound was precipitated in methanol.

Then the precipitate was filtered and purified with Soxhlet extraction using acetone, DCM and chloroform as solvents. The chloroform fraction was evaporated under reduced pressure and the polymer was precipitated in acetone, filtered and finally dried under high vacuum, providing a brownish solid (55 mg).

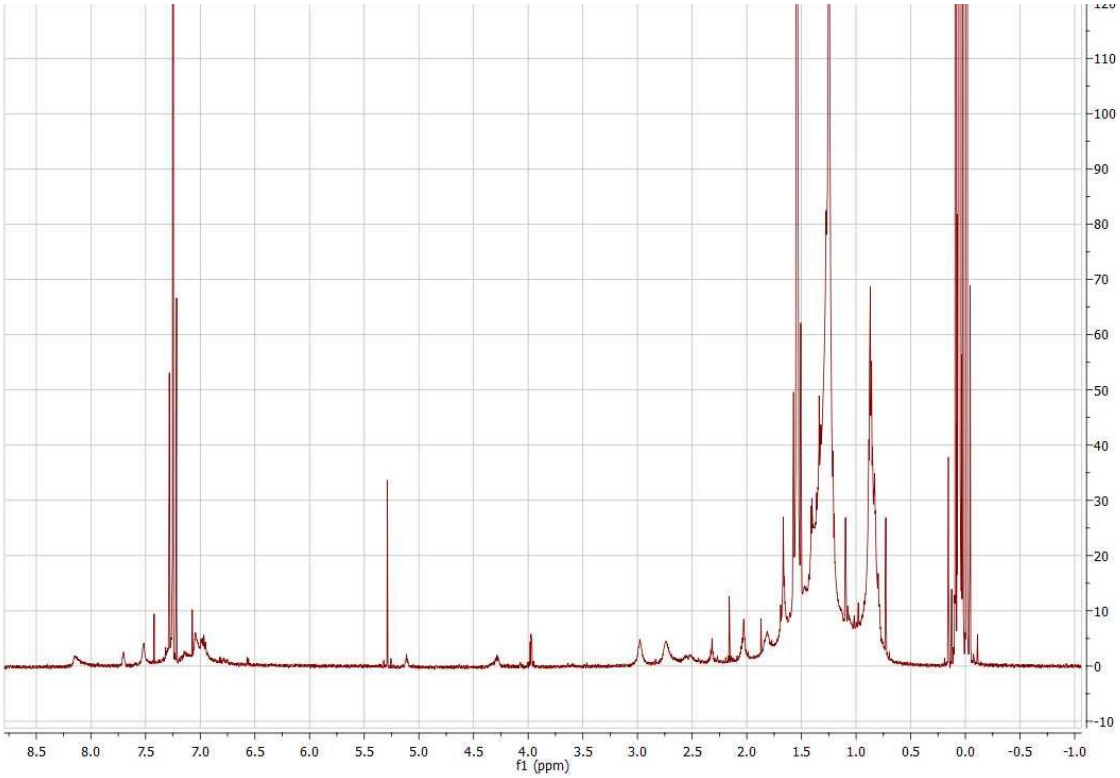

Figure 52. ^{1}H-NMR of BODIPY-qT*i*.

5.2.12 Polymer CB06

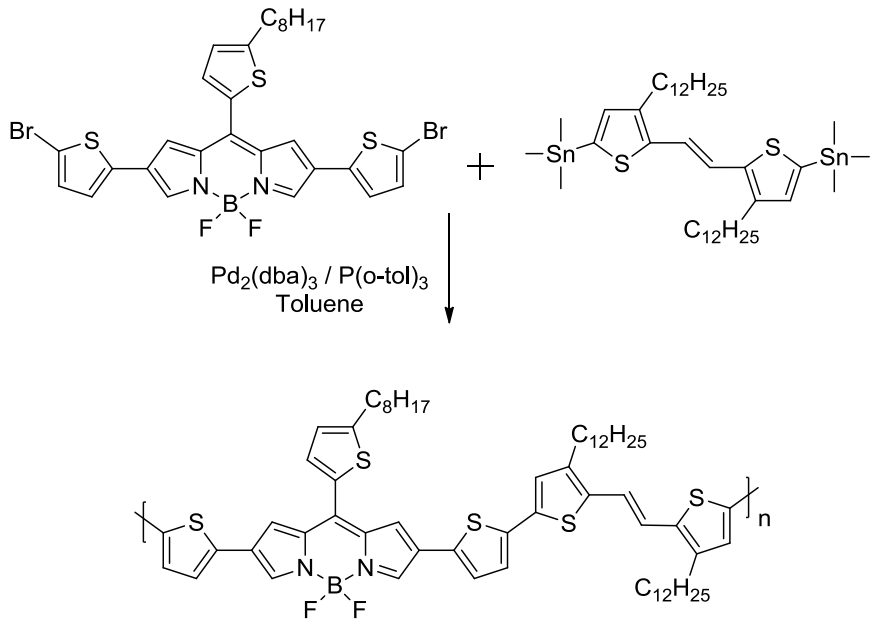

Procedure

A mixture of monomer 5 (110mg, 0,155 mmol), (E)-1,2-bis(3-dodecyl-5-(trimethylstannyl)thiophen-2-yl)ethene (132 mg, 0,155mmol), $Pd_2(dba)_3$ (4,3 mg,0,0046 mol), $P(o\text{-}tol)_3$ (2,8 mg, 0,0093 mmol) were added in a flame dried two neck round bottom flask. Then dry toluene (12,4 mL) was added through a syringe and the reaction mixture started stirring and heating at 110° C for 48h.

Then 2-bromothiophene (0,15 ml, 1,55mmol) was added to the reaction and was stirred for 4 h, then 2-tributylstannylthiophene (0,49 ml,1,55 mmol) was added . The day after the reaction was cooled down and the compound was precipitate in methanol The chloroform fraction was evaporated under reduced pressure and the polymer was precipitated in acetone, filtered and finally dried under high vacuum, providing greenish solid (53 mg).

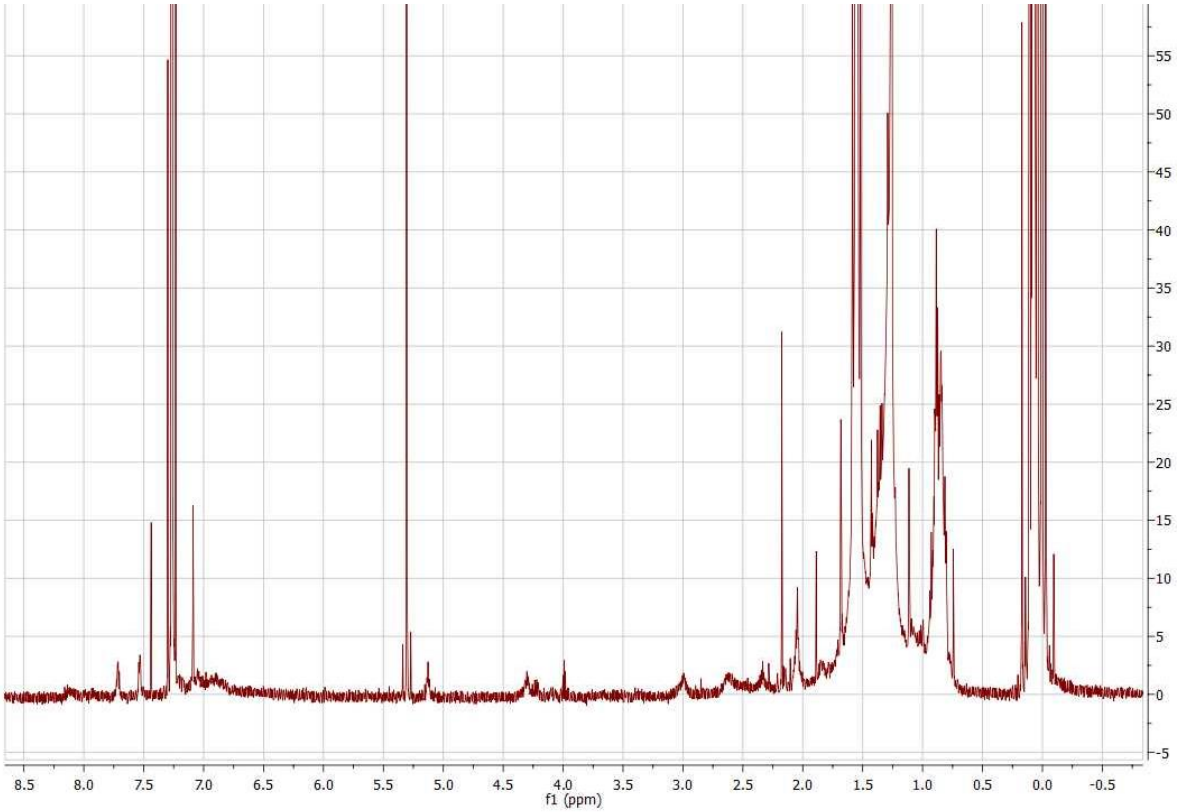

Figure 53. ^{1}H-NMR of CB06.

6.Bibliography

(1) Leclerc, M.; Morin, J.-F. *Synthetic Methods for Conjugated Polymer and Carbon Materials*; Wiley VCH, 2017.
(2) Schwartz, B. J. *Annu. Rev. Phys. Chem.* **2003**, *54*, 141–172.
(3) Asatkar, A. K.; Bedi, A.; Zade, S. S. *Isr. J. Chem.* **2014**, *54*, 467–495.
(4) Farchioni, R.; Grosso, G. *Organic Electronic Materials*; 2001.
(5) Wang, E.; Mammo, W.; Andersson, M. R. *Adv. Mater.* **2014**, *26*, 1801–1826.
(6) Fan, J.; Yuen, J. D.; Cui, W.; Seifter, J.; Mohebbi, A. R.; Wang, M.; Zhou, H.; Heeger, A.; Wudl, F. *Adv. Mater.* **2012**, *24*, 6164–6168.
(7) Facchetti, A. *Mater. Today* **2007**, *10*, 28–37.
(8) Kang, B.; Lee, W. H.; Cho, K. *ACS Appl. Mater. & Interfaces* **2013**, *5*, 2302–2315.
(9) Sirringhaus, H. *Adv. Mater.* **2014**, *26*, 1319–1335.
(10) Geffroy, B.; Roy, P. le; Prat, C. *Polym. Int.* **2006**, *55*, 572–582.
(11) Qu, B.; Chen, Z.; Xiao, L.; Luo, F.; Gong, Q. *Front. Optoelectron. China* **2009**, *2*, 92–102.
(12) Yook, K. S.; Lee, J. Y. *Adv. Mater.* **2014**, *26*, 4218–4233.
(13) Jou, J.-H.; Kumar, S.; Agrawal, A.; Li, T.-H.; Sahoo, S. *J. Mater. Chem. C* **2015**, *3*, 2974–3002.
(14) Yan, J.; Saunders, B. R. *RSC Adv.* **2014**, *4*, 43286–43314.
(15) Lu, L.; Zheng, T.; Wu, Q.; Schneider, A. M.; Zhao, D.; Yu, L. *Chem. Rev.* **2015**, *115*, 12666–12731.
(16) Li, G.; Zhu, R.; Yang, Y. *Nat. Photon-* **2012**, *6*, 153–161.
(17) Ma, C. *Mater. Technol. Appl.* **2016**, 201–250.
(18) Thompson, B. 25emC; Fréchet, J. 25emM \hspace0 25emJ. *Angew. Chem. Int. Ed.* **2008**, *47*, 58–77.
(19) Liu, Y.; Chen, C.-C.; Hong, Z.; Gao, J.; Yang, Y. (Michael); Zhou, H.; Dou, L.; Li, G.; Yang, Y. *Sci. Rep.* **2013**, *3*.
(20) Heeger, A. J. *Adv. Mater.* **2013**, *26*, 10–28.
(21) Feng, G.; Ding, D.; Liu, B. *Nanoscale* **2012**, *4*, 6150.
(22) Klingstedt, T.; Nilsson, K. P. R. *Biochim. et Biophys. Acta* **2011**, *1810*, 286–296.
(23) McGehee, M. D.; Heeger, A. J. *Adv. Mater.* **2000**, *12*, 1655–1668.
(24) Larson, N.; Ghandehari, H. *Chem. Mater.* **2012**, *24*, 840–853.
(25) Veggel, F. C. J. M. van. *Chem. Mater.* **2014**, *26*, 111–122.
(26) Ma, Q.; Su, X. *Anal.* **2010**, *135*, 1867.
(27) Gao, J.; Chen, X.; Cheng, Z. *Curr. Top. Med. Chem.* **2010**, *10*, 1147–1157.
(28) Runnerstrom, E. L.; Llordés, A.; Lounis, S. D.; Milliron, D. J. *Chem. Commun.* **2014**, *50*, 10555.
(29) Bricks, J. L.; Kachkovskii, A. D.; Slominskii, Y. L.; Gerasov, A. O.; Popov, S. V. *Dyes Pigment.* **2015**, *121*, 238–255.
(30) Seo, S.; Pascal, S.; Park, C.; Shin, K.; Yang, X.; Maury, O.; Sarwade, B. D.; Andraud, C.; Kim, E. *Chem. Sci.* **2014**, *5*, 1538.
(31) Samanta, A.; Vendrell, M.; Das, R.; Chang, Y.-T. *Chem. Commun.* **2010**, *46*, 7406.
(32) Tolmachev, A. I.; Slominskii, Y. L.; Ishchenko, A. A. *Near-Infrared Dyes High Technol. Appl.* **1998**, 385–415.
(33) Salvador, M. A.; Almeida, P.; Reis, L. V.; Santos, P. F. *Dyes Pigment.* **2009**, *82*,

118–123.
(34) Bello, K. A.; Griffiths, J. *J. Chem. Soc. Chem. Commun.* **1986**, 1639.
(35) Xu, A.-P.; Han, H.-H.; Lu, J.; Yang, P.-P.; Gao, Y.-J.; An, H.-W.; Zhanng, D.; Li, L.-Z.; Zhang, J.-P.; Wang, D.; Wang, L.; Wang, H. *Dyes Pigment.* **2016**, *125*, 392–398.
(36) Li, W.; Liu, Z.; Xu, X.; Cheng, Y.-B.; Zhao, Z.; He, H. *RSC Adv.* **2014**, *4*, 50897–50905.
(37) Li, D.-D.; Wang, J.-X.; Ma, Y.; Qian, H.-S.; Wang, D.; Wang, L.; Zhang, G.; Qiu, L.; Wang, Y.-C.; Yang, X.-Z. *ACS Appl. Mater. & Interfaces* **2016**, *8*, 19312–19320.
(38) Karton-Lifshin, N.; Albertazzi, L.; Bendikov, M.; Baran, P. S.; Shabat, D. *J. Am. Chem. Soc.* **2012**, *134*, 20412–20420.
(39) Qin, C.; Fu, Y.; Chui, C.-H.; Kan, C.-W.; Xie, Z.; Wang, L.; Wong, W.-Y. *Macromol. Rapid Commun.* **2011**, *32*, 1472–1477.
(40) *Near-Infrared Dyes for High Technology Applications*; Daehne, S.; Resch-Genger, U.; Wolfbeis, O. S., Eds.; Springer Nature, 1998.
(41) Fabian, J.; Nakazumi, H.; Matsuoka, M. *Chem. Rev.* **1992**, *92*, 1197–1226.
(42) Spikes, J. D. *Photochem. Photobiol.* **1986**, *43*, 691–699.
(43) Scharber, M. C.; Sariciftci, N. S. *Prog. Polym. Sci.* **2013**, *38*, 1929–1940.
(44) Heremans, P.; Cheyns, D.; Rand, B. P. *Accounts Chem. Res.* **2009**, *42*, 1740–1747.
(45) Ameri, T.; Forster, M.; Scherf, U.; Brabec, C. J. *Elem. Process. Org. Photovoltaics* **2016**, 311–326.
(46) Lu, L.; Xu, T.; Chen, W.; Landry, E. S.; Yu, L. *Nat. Photon-* **2014**, *8*, 716–722.
(47) Lim, B.; Bloking, J. T.; Ponec, A.; McGehee, M. D.; Sellinger, A. *ACS Appl. Mater. & Interfaces* **2014**, *6*, 6905–6913.
(48) Ameri, T.; Min, J.; Li, N.; Machui, F.; Baran, D.; Forster, M.; Schottler, K. J.; Dolfen, D.; Scherf, U.; Brabec, C. J. *Adv. Energy Mater.* **2012**, *2*, 1198–1202.
(49) Hertel, D.; Marechal, H.; Tefera, D. A.; Fan, W.; Hicks, R. *2009 IEEE Intell. Veh. Symp.* **2009**.
(50) Wang, R.; Zhang, F. *J. Mater. Chem. B* **2014**, *2*, 2422.
(51) Escobedo, J. O.; Rusin, O.; Lim, S.; Strongin, R. M. *Curr. Opin. Chem. Biol.* **2010**, *14*, 64–70.
(52) Xu, C.; Ye, J.; Marks, D. L.; Boppart, S. A. *Opt. Lett.* **2004**, *29*, 1647–1649.
(53) Roncali, J. *Chem. Rev.* **1997**, *97*, 173–206.
(54) Kiebooms, R.; Menon, R.; Lee, K. *Handb. Adv. Electron. Photon- Mater. Devices* **2001**, 1–102.
(55) Castiglioni, C.; Zerbi, G.; Gussoni, M. *Solid State Commun.* **1985**, *56*, 863–866.
(56) Brédas, J. L. *J. Chem. Phys.* **1985**, *82*, 3808–3811.
(57) Bredas, J. L. *Synth. Met.* **1987**, *17*, 115–121.
(58) Kobayashi, M.; Colaneri, N.; Boysel, M.; Wudl, F.; Heeger, A. J. *J. Chem. Phys.* **1985**, *82*, 5717–5723.
(59) Brédas, J. L.; Heeger, A. J.; Wudl, F. *J. Chem. Phys.* **1986**, *85*, 4673–4678.
(60) Hess, B. A.; Schaad, L. J.; Holyoke, C. W. *Tetrahedron* **1972**, *28*, 3657–3667.
(61) Hess, B. A.; Schaad, L. J. *J. Am. Chem. Soc.* **1973**, *95*, 3907–3912.
(62) Brédas, J. L.; Street, G. B.; Thémans, B.; André, J. M. *J. Chem. Phys.* **1985**, *83*, 1323–1329.
(63) Cui, C. X.; Kertesz, M. *Phys. Rev. B* **1989**, *40*, 9661–9670.
(64) Li, Y. *Accounts Chem. Res.* **2012**, *45*, 723–733.
(65) Ho, H. A.; Brisset, H.; Frère, P.; Roncali, J. *J. Chem. Soc., Chem. Commun.* **1995**, 2309–2310.
(66) Bredas, J. L.; Silbey, R.; Boudreaux, D. S.; Chance, R. R. *J. Am. Chem. Soc.* **1983**,

105, 6555–6559.
(67) Grimme, J.; Kreyenschmidt, M.; Uckert, F.; Müllen, K.; Scherf, U. *Adv. Mater.* **1995**, *7*, 292–295.
(68) Pschirer, N. G.; Kohl, C.; Nolde, F.; Qu, J.; Müllen, K. *Angew. Chem. Int. Ed.* **2006**, *45*, 1401–1404.
(69) Rissler, J. *Chem. Phys. Lett.* **2004**, *395*, 92–96.
(70) Filapek, M.; Matussek, M.; Szlapa, A.; Kula, S.; Paj\kak, M. *Electrochimica Acta* **2016**, *216*, 449–456.
(71) Griffith, O. L.; Jones, A. G.; Anthony, J. E.; Lichtenberger, D. L. *J. Phys. Chem. C* **2010**, *114*, 13838–13845.
(72) Spano, F. C.; Silva, C. *Annu. Rev. Phys. Chem.* **2014**, *65*, 477–500.
(73) Kularatne, R. S.; Magurudeniya, H. D.; Sista, P.; Biewer, M. C.; Stefan, M. C. *J. Polym. Sci. Part A: Polym. Chem.* **2012**, *51*, 743–768.
(74) Ajayaghosh, A. *Chem. Soc. Rev.* **2003**, *32*, 181–191.
(75) Tan, C.-J.; Yang, C.-S.; Sheng, Y.-C.; Amini, H. W.; Tsai, H.-H. G. *J. Phys. Chem. C* **2016**, *120*, 21272–21284.
(76) Wood, T. E.; Thompson, A. *Chem. Rev.* **2007**, *107*, 1831–1861.
(77) Treibs, A.; Kreuzer, F.-H. *Justus Liebigs Ann. Chem.* **1968**, *718*, 208–223.
(78) Loudet, A.; Burgess, K. *Chem. Rev.* **2007**, *107*, 4891–4932.
(79) Sathyamoorthi, G.; Boyer, J. H.; Allik, T. H.; Chandra, S. *Heteroat. Chem.* **1994**, *5*, 403–407.
(80) Pavlopoulos, T. G.; Shah, M.; Boyer, J. H. *Appl. Opt.* **1988**, *27*, 4998.
(81) Pavlopoulos, T. G.; Shah, M.; Boyer, J. H. *Opt. Commun.* **1989**, *70*, 425–427.
(82) Wang, D.; Miyamoto, R.; Shiraishi, Y.; Hirai, T. *Langmuir* **2009**, *25*, 13176–13182.
(83) Kennedy, D. P.; Kormos, C. M.; Burdette, S. C. *J. Am. Chem. Soc.* **2009**, *131*, 8578–8586.
(84) Rosenthal, J.; Lippard, S. J. *J. Am. Chem. Soc.* **2010**, *132*, 5536–5537.
(85) Lee, C. Y.; Hupp, J. T. *Langmuir* **2010**, *26*, 3760–3765.
(86) Godoy, J.; Vives, G.; Tour, J. M. *Org. Lett.* **2010**, *12*, 1464–1467.
(87) Nierth, A.; Kobitski, A. Y.; Nienhaus, G. U.; Jäschke, A. *J. Am. Chem. Soc.* **2010**, *132*, 2646–2654.
(88) uelos, J. B.; Arbeloa, F. L.; Arbeloa, T.; Salleres, S.; Amat-Guerri, F.; Liras, M.; Arbeloa, I. L. *J. Phys. Chem.* **2008**, *112*, 10816–10822.
(89) Yogo, T.; Urano, Y.; Ishitsuka, Y.; Maniwa, F.; Nagano, T. *J. Am. Chem. Soc.* **2005**, *127*, 12162–12163.
(90) Meng, G.; Velayudham, S.; Smith, A.; Luck, R.; Liu, H. *Macromolecules* **2009**, *42*, 1995–2001.
(91) Thivierge, C.; Bandichhor, R.; Burgess, K. *Org. Lett.* **2007**, *9*, 2135–2138.
(92) Lai, R. Y.; Bard, A. J. *J. Phys. Chem. B* **2003**, *107*, 5036–5042.
(93) Nepomnyashchii, A. B.; Cho, S.; Rossky, P. J.; Bard, A. J. *J. Am. Chem. Soc.* **2010**, *132*, 17550–17559.
(94) Forgie, J. C.; Skabara, P. J.; Stibor, I.; Vilela, F.; Vobecka, Z. *Chem. Mater.* **2009**, *21*, 1784–1786.
(95) Cortizo-Lacalle, D.; Howells, C. T.; Gambino, S.; Vilela, F.; Vobecka, Z.; Findlay, N. J.; Inigo, A. R.; Thomson, S. A. J.; Skabara, P. J.; Samuel, I. D. W. *J. Mater. Chem.* **2012**, *22*.
(96) Yilmaz, M. D.; Aytun, T.; Frasconi, M.; Stupp, S. I.; Stoddart, J. F. *Synth. Met.* **2014**, *197*, 52–57.
(97) Marzano, G.; Ciasca, C. V.; Babudri, F.; Bianchi, G.; Pellegrino, A.; Po, R.;

Farinola, G. M. *Eur. J. Org. Chem.* **2014**, *2014*, 6583–6614.
(98) Hayashi, Y.; Yamaguchi, S.; Cha, W. Y.; Kim, D.; Shinokubo, H. *Org. Lett.* **2011**, *13*, 2992–2995.
(99) Wang, L.; Wang, J.-W.; Cui, A.; Cai, X.-X.; Wan, Y.; Chen, Q.; He, M.-Y.; Zhang, W. *RSC Adv.* **2013**, *3*, 9219–9222.
(100) Kawashima, K.; Tamai, Y.; Ohkita, H.; Osaka, I.; Takimiya, K. *Nat. Commun.* **2015**, *6*.
(101) Usta, H.; Risko, C.; Wang, Z.; Huang, H.; Deliomeroglu, M. K.; Zhukhovitskiy, A.; Facchetti, A.; Marks, T. J. *J. Am. Chem. Soc.* **2009**, *131*, 5586–5608.
(102) Usta, H.; Facchetti, A.; Marks, T. J. *J. Am. Chem. Soc.* **2008**, *130*, 8580–8581.
(103) Jones, B. A.; Ahrens, M. J.; Yoon, M.-H.; Facchetti, A.; Marks, T. J.; Wasielewski, M. R. *Angew. Chem. Int. Ed.* **2004**, *43*, 6363–6366.
(104) Wang, Z.; Kim, C.; Facchetti, A.; Marks, T. J. *J. Am. Chem. Soc.* **2007**, *129*, 13362–13363.
(105) Schmidt, R.; Ling, M. \hspace0 167emM; Oh, J. \hspace0 167emH; Winkler, M.; Könemann, M.; Bao, Z.; Würthner, F. *Adv. Mater.* **2007**, *19*, 3692–3695.
(106) Chochos, C. L.; Singh, R.; Kim, M.; Gasparini, N.; Katsouras, A.; Kulshreshtha, C.; Gregoriou, V. G.; Keivanidis, P. E.; Ameri, T.; Brabec, C. J.; Cho, K.; Avgeropoulos, A. *Adv. Funct. Mater.* **2016**, *26*, 1840–1848.
(107) Zhan, X.; Facchetti, A.; Barlow, S.; Marks, T. J.; Ratner, M. A.; Wasielewski, M. R.; Marder, S. R. *Adv. Mater.* **2010**, *23*, 268–284.
(108) Mei, J.; Diao, Y.; Appleton, A. L.; Fang, L.; Bao, Z. *J. Am. Chem. Soc.* **2013**, *135*, 6724–6746.
(109) Nuzzo, D. D.; Wetzelaer, G.-J. A. H.; Bouwer, R. K. M.; Gevaerts, V. S.; Meskers, S. C. J.; Hummelen, J. C.; Blom, P. W. M.; Janssen, R. A. J. *Adv. Energy Mater.* **2012**, *3*, 85–94.
(110) Pivrikas, A.; Sariciftci, N. S.; Juška, G.; Österbacka, R. *Prog. Photovoltaics: Res. Appl.* **2007**, *15*, 677–696.
(111) Mozer, A. J.; Dennler, G.; Sariciftci, N. S.; Westerling, M.; Pivrikas, A.; Österbacka, R.; Juška, G. *Phys. Rev. B* **2005**, *72*.
(112) Chua, L.-L.; Zaumseil, J.; Chang, J.-F.; Ou, E. C.-W.; Ho, P. K.-H.; Sirringhaus, H.; Friend, R. H. *Nature* **2005**, *434*, 194–199.
(113) Anthopoulos, T. D.; Singh, B.; Marjanovic, N.; Sariciftci, N. S.; Ramil, A. M.; Sitter, H.; Cölle, M.; Leeuw, D. M. de. *Appl. Phys. Lett.* **2006**, *89*, 213504.
(114) Ball, J. M.; Bouwer, R. K. M.; Kooistra, F. B.; Frost, J. M.; Qi, Y.; Domingo, E. B.; Smith, J.; Leeuw, D. M. de; Hummelen, J. C.; Nelson, J.; Kahn, A.; Stingelin, N.; Bradley, D. D. C.; Anthopoulos, T. D. *J. Appl. Phys.* **2011**, *110*, 014506.
(115) Sekitani, T.; Someya, T. *Adv. Mater.* **2010**, *22*, 2228–2246.
(116) Ok, K.-H.; Kim, J.; Park, S.-R.; Kim, Y.; Lee, C.-J.; Hong, S.-J.; Kwak, M.-G.; Kim, N.; Han, C. J.; Kim, J.-W. *Sci. Reports* **2015**, *5*.
(117) Tan, Z.-K.; Moghaddam, R. S.; Lai, M. L.; Docampo, P.; Higler, R.; Deschler, F.; Price, M.; Sadhanala, A.; Pazos, L. M.; Credgington, D.; Hanusch, F.; Bein, T.; Snaith, H. J.; Friend, R. H. *Nat. Nanotechnol.* **2014**, *9*, 687–692.
(118) Duncan, T. V.; Susumu, K.; Sinks, L. E.; Therien, M. J. *J. Am. Chem. Soc.* **2006**, *128*, 9000–9001.
(119) Tzamalis, G.; Lemaur, V.; Karlsson, F.; Holtz, P. O.; Andersson, M.; Crispin, X.; Cornil, J.; Berggren, M. *Chem. Phys. Lett.* **2010**, *489*, 92–95.
(120) Hickey, S. G.; Gaponik, N.; Eychmüller, A. *Photon- Nanostructures - Fundam. Appl.* **2007**, *5*, 113–118.
(121) Ly, K. T.; Chen-Cheng, R.-W.; Lin, H.-W.; Shiau, Y.-J.; Liu, S.-H.; Chou, P.-T.;

Tsao, C.-S.; Huang, Y.-C.; Chi, Y. *Nat. Photon-* **2016**, *11*, 63–68.
(122) Slooff, L. H.; Polman, A.; Cacialli, F.; Friend, R. H.; Hebbink, G. A.; Veggel, F. C. J. M. van; Reinhoudt, D. N. *Appl. Phys. Lett.* **2001**, *78*, 2122–2124.
(123) Borek, C.; Hanson, K.; Djurovich, P. 25emI; Thompson, M. 25emE; Aznavour, K.; Bau, R.; Sun, Y.; Forrest, S. 25emR; Brooks, J.; Michalski, L.; Brown, J. *Angew. Chem.* **2007**, *119*, 1127–1130.
(124) Sommer, J. R.; Farley, R. T.; Graham, K. R.; Yang, Y.; Reynolds, J. R.; Xue, J.; Schanze, K. S. *ACS Appl. Mater. & Interfaces* **2009**, *1*, 274–278.
(125) Graham, K. R.; Yang, Y.; Sommer, J. R.; Shelton, A. H.; Schanze, K. S.; Xue, J.; Reynolds, J. R. *Chem. Mater.* **2011**, *23*, 5305–5312.
(126) Qian, G.; Wang, Z. Y. *Chem. - Asian J.* **2010**, *5*, 1006–1029.
(127) Ashraf, R. S.; Kronemeijer, A. J.; James, D. I.; Sirringhaus, H.; McCulloch, I. *Chem. Commun.* **2012**, *48*, 3939.
(128) Ashraf, R. S.; Meager, I.; Nikolka, M.; Kirkus, M.; Planells, M.; Schroeder, B. C.; Holliday, S.; Hurhangee, M.; Nielsen, C. B.; Sirringhaus, H.; McCulloch, I. *J. Am. Chem. Soc.* **2015**, *137*, 1314–1321.
(129) Yuen, J. D.; Kumar, R.; Zakhidov, D.; Seifter, J.; Lim, B.; Heeger, A. J.; Wudl, F. *Adv. Mater.* **2011**.
(130) Fei, Z.; Gao, X.; Smith, J.; Pattanasattayavong, P.; Domingo, E. B.; Stingelin, N.; Watkins, S. E.; Anthopoulos, T. D.; Kline, R. J.; Heeney, M. *Chem. Mater.* **2012**, *25*, 59–68.
(131) Tam, T. L. D.; Salim, T.; Li, H.; Zhou, F.; Mhaisalkar, S. G.; Su, H.; Lam, Y. M.; Grimsdale, A. C. *J. Mater. Chem.* **2012**, *22*, 18528.
(132) Dallos, T.; Beckmann, D.; Brunklaus, G.; Baumgarten, M. *J. Am. Chem. Soc.* **2011**, *133*, 13898–13901.
(133) Han, X.; Bai, Q.; Yao, L.; Liu, H.; Gao, Y.; Li, J.; Liu, L.; Liu, Y.; Li, X.; Lu, P.; Yang, B. *Adv. Funct. Mater.* **2015**, *25*, 7521–7529.
(134) Yao, L.; Zhang, S.; Wang, R.; Li, W.; Shen, F.; Yang, B.; Ma, Y. *Angew. Chem.* **2014**, *126*, 2151–2155.
(135) Nepomnyashchii, A. B.; Bröring, M.; Ahrens, J.; Bard, A. J. *J. Am. Chem. Soc.* **2011**, *133*, 8633–8645.
(136) Rihn, S.; Erdem, M.; Nicola, A. D.; Retailleau, P.; Ziessel, R. *Org. Lett.* **2011**, *13*, 1916–1919.
(137) Yang, Y.; Guo, Q.; Chen, H.; Zhou, Z.; Guo, Z.; Shen, Z. *Chem. Commun.* **2013**, *49*, 3940.
(138) Fabiano, S.; Usta, H.; Forchheimer, R.; Crispin, X.; Facchetti, A.; Berggren, M. *Adv. Mater.* **2014**, *26*, 7438–7443.
(139) Usta, H.; Newman, C.; Chen, Z.; Facchetti, A. *Adv. Mater.* **2012**, *24*, 3678–3684.
(140) Kim, Y.; Cho, H.-H.; Kim, T.; Liao, K.; Kim, B. J. *Polym. J.* **2016**, *48*, 517–524.
(141) Chen, Z.; Zheng, Y.; Yan, H.; Facchetti, A. *J. Am. Chem. Soc.* **2009**, *131*, 8–9.

The biography is not included in the online version for reasons of data protection

"

The biography is not included in the online version for reasons of data protection

The biography is not included in the online version for reasons of data protection

The biography is not included in the online version for reasons of data protection